INAUGURAL – DISSERTATION

submitted to the
Combined Faculty of Natural Sciences and Mathematics
of the Ruperto Carola University Heidelberg, Germany
for the degree of
Doctor of Natural Sciences

Put forward by
Fabian Josef Kratzer, M.Sc.
Born in: Mannheim, Germany
Oral examination: December 15th, 2021

On the Simultaneous Mapping of Sodium Relaxation Parameters using Magnetic Resonance Fingerprinting

Referees: Prof. Dr. Peter Bachert
Prof. Dr. Lothar R. Schad

On the Simultaneous Mapping of Sodium Relaxation Parameters using Magnetic Resonance Fingerprinting

In this thesis, the development of a framework for simultaneous sodium (^{23}Na) mapping of T_1, T_{2l}^*, T_{2s}^*, T_2^* and ΔB_0, based on magnetic resonance fingerprinting (MRF), is presented.

In initial experiments, the feasibility of ^{23}Na MRF was investigated using a 2D MRF sequence with variable-rate selective excitation pulses and density adapted readout gradients at a static magnetic field strength of 7 T. The proposed technique was validated in simulations and phantom experiments by comparison of the MRF results to reference measurements. An ensuing in vivo study of the human brain was performed with five healthy volunteers, yielding results in good agreement with the literature.

Subsequently, a 3D version of the pulse sequence was developed to increase the scan efficiency and an improved signal model for spin 3/2 nuclei, based on irreducible spherical tensor operators, was implemented. In an optimization step, a hybrid of single- and double-echo readouts and a flip angle pattern optimized with the Cramér Rao lower bound were implemented. Phantom experiments yielded a mean deviation of the quantified relaxation times of 1.0 % with respect to the references. A second in vivo study, conducted with the optimized 3D MRF framework, yielded good agreement to both the 2D MRF study and literature values. Mean values of $T_1 = (35.0 \pm 3.2)\,\mathrm{ms}$, $T_{2l}^* = (29.3 \pm 3.8)\,\mathrm{ms}$ and $T_{2s}^* = (5.5 \pm 1.3)\,\mathrm{ms}$ were found in brain tissue, whereas T_1 and T_2^* were $(61.9 \pm 2.8)\,\mathrm{ms}$ and $(46.3 \pm 4.5)\,\mathrm{ms}$ in cerebrospinal fluid. The culmination of all advancements proposed throughout this work enabled relaxometric sodium mapping of the human head within approximately $\frac{1}{2}\,\mathrm{h}$ with a nominal resolution of $(5\,\mathrm{mm})^3$.

The findings of this work suggest that ^{23}Na MRF is a promising candidate to push sodium relaxometric mapping towards clinically feasible measurement times.

Über die simultane Quantifizierung von Natriumrelaxationszeiten mit Hilfe von Magnetic Resonance Fingerprinting

In dieser Arbeit wird eine Technik zur simultanen Quantifizierung von T_1, T_{2l}^*, T_{2s}^* und T_2^* von Natrium (^{23}Na) sowie ΔB_0 vorgestellt, die auf Magnetic Resonance Fingerprinting (MRF) beruht.

In ersten Experimenten wurde die Anwendbarkeit von MRF auf die ^{23}Na-MRT mit Hilfe einer 2D-Pulssequenz untersucht, in welcher VERSE (variable-rate selective excitation) Anregungspulse und dichteangepasste Auslesegradienten bei einer statischen Magnetfeldstärke von 7 T genutzt werden. Die vorgestellte Technik wurde in Simulationen und Phantomexperimenten, in welchen die MRF-Ergebnisse mit Referenzmessungen verglichen wurden, validiert. In einer darauffolgenden in-vivo-Studie wurden die Relaxationszeiten im Kopf von fünf gesunden Probanden quantifiziert, wobei sich eine gute Übereinstimmung mit Literaturwerten ergab.

Anschließend wurde eine 3D-Version der Pulssequenz entwickelt, um die Messeffizienz zu erhöhen und ein verbessertes Signalmodel für Spin-3/2-Kerne implementiert, welches auf nichtreduzierbaren sphärischen Tensoroperatoren beruht. In der darauffolgenden Optimierung wurde die Sequenz durch einen Hybrid aus Einfach- und Doppelauslesen und eine Flipwinkel-Abfolge, welche mit dem Cramér Rao lower bound optimiert wurde, verbessert. Phantomexperimente zeigten eine mittlere Abweichung der Relaxationsparameter von 1,0 % zu den Referenzen. In einer zweiten in-vivo-Studie wurden die Relaxationszeiten im menschlichen Kopf mit der optimierten 3D-MRF-Sequenz bestimmt, wobei sich eine gute Übereinstimmung zu der 2D-Studie und den Literaturwerten ergab. In Hirngewebe wurden mittlere Werte von $T_1 = (35{,}0 \pm 3{,}2)\,\mathrm{ms}$, $T_{2l}^* = (29{,}3 \pm 3{,}8)\,\mathrm{ms}$ und $T_{2s}^* = (5{,}5 \pm 1{,}3)\,\mathrm{ms}$ quantifiziert, wohingegen ein T_1 von $(61{,}9 \pm 2{,}8)\,\mathrm{ms}$ und ein T_2^* von $(46{,}3 \pm 4{,}5)\,\mathrm{ms}$ in Liquor bestimmt wurden. Die Methoden dieser Arbeit ermöglichten die Quantifizierung der Relaxationszeiten im menschlichen Kopf bei einer nominellen Auflösung von $(5\,\mathrm{mm})^3$ innerhalb von etwa $\frac{1}{2}\,\mathrm{h}$.

Die Ergebnisse dieser Arbeit legen nahe, dass ^{23}Na-MRF einen vielversprechenden Kandidaten zur Relaxometriemessung von Natrium innerhalb klinischer Messzeiten darstellt.

Contents

1 Introduction

Medical imaging evolved to a key feature in medical diagnostics in the last decades, wherefore a variety of imaging modalities is used in clinical routine. Magnetic resonance imaging (MRI) is among the most prominent techniques since it provides excellent tissue contrast without the need of ionizing radiation. Application of different magnetic resonance (MR) sequences allows acquisition of a multitude of different information such as spatiotemporal morphology, quantification of flow and imaging of physiological processes, to name just a few.

In clinical routine, most MR sequences are qualitative in their nature, referring to the fact that a good tissue contrast is achieved but the individual pixel value depends on a variety of parameters, during data acquisition and reconstruction. This depicts only a minor drawback as highly trained physicians are used to perform diagnostics based on those images. However, quantitative measurements should allow automated diagnostics. Further, true quantitative imaging would eliminate inter-site variability and diagnostics could be based on a large database of normal and diseased tissue properties.

The vast majority of MRI sequences is based on acquiring the signal of ^{1}H nuclei, as they yield by far the highest signal in the human body. In theory, however, all other nuclei with non-vanishing spin can be used in MRI, which are commonly termed X-nuclei. Some of them, such as ^{23}Na, ^{31}P and ^{39}K, are involved in many cellular processes. Hence, a variety of applications for X-nuclei MRI has been investigated to provide insight into physiological processes. Sodium (^{23}Na) ions provide the second highest signal in the human body and constitute a key component in a number of physiological processes, such as the ^{23}Na-^{39}K-pump. Consequently, a multitude of pathologies, like neurodegenerative diseases and cancer, were investigated using ^{23}Na MRI. Many studies aimed for quantification of the tissue sodium concentration (TSC), which provides a volume-weighted combination of intra- and extracellular sodium concentrations [1]. Other studies applied relaxation weighted imaging [2, 3, 4, 5], where altered relaxation times were found in several diseases. Consequently, knowledge of ^{23}Na relaxation times might give additional diagnostic value, wherefore several studies aimed for quantification of them [6, 7, 8, 9]. However, sodium relaxometric mapping found limited application in clinical routine since it suffers from long measurement times, which are required due to the inherently low signal-to-noise ratio (SNR) of sodium imaging. To counteract these issues, the scans are often performed at ultra-high static magnetic fields ($B_0 \geq 7\,\mathrm{T}$) and sequences with low resolution and ultra-short echo times (UTEs) are exploited. Nevertheless, scan durations of approximately one hour for quantification of either the longitudinal or the transverse relaxation times have been reported [4, 8, 9]. This issue was tackled with techniques such as 3D-MERINA [7] and the variable flip angle method [6].

In ^{1}H imaging, magnetic resonance fingerprinting (MRF) evolved in recent years to one of the most promising techniques for rapid multi-parametric quantification, mainly the relaxation times [10]. Here, multiple tissue parameters are quantified simultaneously by transferring the encoding problem of conventional mapping techniques to a separation problem in MRF. This is achieved by driving the magnetization in a non-steady state condition, which is commonly achieved by continuous change of the sequence parameters, such as flip angles (FAs) and sequence timings. The exact signal evolution (fingerprint) then depends on the tissue parameters. Hence, a series of highly undersampled images is acquired to sample the evolution of the transient signal. The MR parameters in each voxel can then be recovered using a simulation based image reconstruction. Due to those properties, MRF was used to quantify a variety of tissue contrasts such as relaxometry [10], flow velocity [11], chemical exchange [12] and many more. A connection to X-nuclei imaging was established by Yu et al. [13], who presented simultaneous ^{1}H MRF and ^{23}Na imaging. In X-nuclei imaging, MRF was exploited for determination of the signal distribution of different ^{23}Na compartments [14] and for spectroscopic ^{31}P quantification of the creatine kinase reaction rate [15].

Therefore, the aim of this work was to develop an MRF framework for relaxometric ^{23}Na mapping, which is the first application of MRF in X-nuclei relaxometry, to the best of the authors knowledge.

Hence, a 2D ^{23}Na MRF sequence for simultaneous quantification of T_1, T_{2l}^*, T_{2s}^*, T_2^* and ΔB_0 was developed as a proof of concept. The corresponding signal simluation was based on a two-compartment Bloch model to enable biexponential transverse relaxation. Moreover, automatic differentiation between bi- and monoexponential transverse relaxation without the need for prior knowledge was enabled in the reconstruction. The proof of concept was shown by applying the 2D MRF sequence in phantom experiments and conducting a subsequent in vivo study, quantifying the relaxometric parameters in the heads of five healthy volunteers. After the feasibility of ^{23}Na MRF was shown, the sequence was implemented as a 3D version, which allows 3D measurement of head-sized objects in the same duration as required for acquisition of a single slice with the 2D sequence. Further, the 3D dictionary simulations were based on irreducible spherical tensor operators (ISTOs), which allow full description the spin dynamics of spin 3/2 particles. Finally, the 3D MRF sequence was refined by optimizing the FA pattern using

the Cramér Rao lower bound (CRLB) to improve T_1 encoding. Moreover, the readout efficiency was increased by implementing a hybrid of single- and double echo readouts. The encoding capabilities of both 3D sequences were compared in phantom experiments and the improved sequence version was used in subsequent in vivo experiments.

The final MRF framework allowed relaxometric mapping of the human head in approximately $\frac{1}{2}\,\mathrm{h}$ with a nominal resolution of $(5\,\mathrm{mm})^3$, pushing sodium relaxometric mapping towards clinically feasible scan durations.

2 Theory

In this section the basic concepts of MRI, MRF and the particularities of ^{23}Na MR are illustrated. A detailed description can be found in standard literature like [16, 17, 18], on which this section is based on.

2.1 Nuclear magnetic resonance

In this work, two different spin dynamic models are used, where one is based on Bloch equations, conventionally used for description of spin 1/2 nuclei. The other model is based on ISTOs, which allow full description of the spin dynamics of spin 3/2 nuclei. Consequently, both models are described in the following.

Every atom is composed of electrons and a nucleus, which itself consists out of protons and neutrons. These protons and neutrons, also called nucleons, inherently posses an intrinsic quantized angular momentum, called the nuclear spin. In cases where the spins of the nucleons do not cancel out, the nucleus has non-vanishing nuclear spin, which leads to the magnetic moment $\vec{\mu}$

$$\vec{\mu} = \gamma \vec{I}. \tag{2.1}$$

Here, γ corresponds to the nucleus-specific gyromagnetic ratio, which is $\gamma_{^1H} = 267.522 \cdot 10^6\,\mathrm{rad/s\,T}$ for hydrogen (^{1}H) and $\gamma_{^{23}Na} = 70.808 \cdot 10^6\,\mathrm{rad/s\,T}$ for sodium (^{23}Na).

In the quantum mechanical description the nuclear spin $\vec{I}$ fulfills the commutator relations

$$[I_l, I_m] = i\hbar\epsilon_{lmn} I_n \tag{2.2}$$

and

$$[\vec{I}, I_l] = 0. \tag{2.3}$$

Choosing the z-axis as quantization axis, the following eigenvalue equations are valid for the angular momentum state vector $|I, m\rangle$:

$$\vec{I}^2 |I, m\rangle = I(I+1)\hbar^2 |I, m\rangle \tag{2.4}$$

$$I_z |I, m\rangle = m\hbar |I, m\rangle. \tag{2.5}$$

Here, I corresponds to the spin quantum number and m to the magnetic spin quantum

number, for which $m \in \{-I, -I+1, ..., I\}$ is valid.
In free space, the energy level of the nucleus is independent of m and consequently $(2I+1)$-fold degenerated.
Application of an external magnetic field $\vec{B_0}$ lifts this degeneration due to interaction of the magnetic moment $\vec{\mu}$ with the field. Without loss of generality we assume that $\vec{B_0} = (0, 0, B_0)^T$ points in z-direction, which yields the Hamilton operator $\mathcal{H}$:

$$\mathcal{H} = \vec{\mu}\vec{B_0} = -\gamma B_0 I_z. \tag{2.6}$$

Equations 2.5 and 2.6, in conjunction with the time-independent Schrödinger equation, therefore lead to the allowed energies E_m

$$E_m = \langle m, I|\mathcal{H}|I, m\rangle = -\gamma\hbar m B_0. \tag{2.7}$$

The energy difference between two neighboring states is therefore given by

$$\Delta E = E_{m+1} - E_m = \hbar\omega_0, \tag{2.8}$$

where ω_0 corresponds to the Larmor frequency

$$\omega_0 = \gamma B_0. \tag{2.9}$$

Therefore, transitions between the states can be induced when a photon with this energy is absorbed or emitted. The energy splitting of ^{1}H and ^{23}Na systems in an external magnetic field are visualized in figure 1.

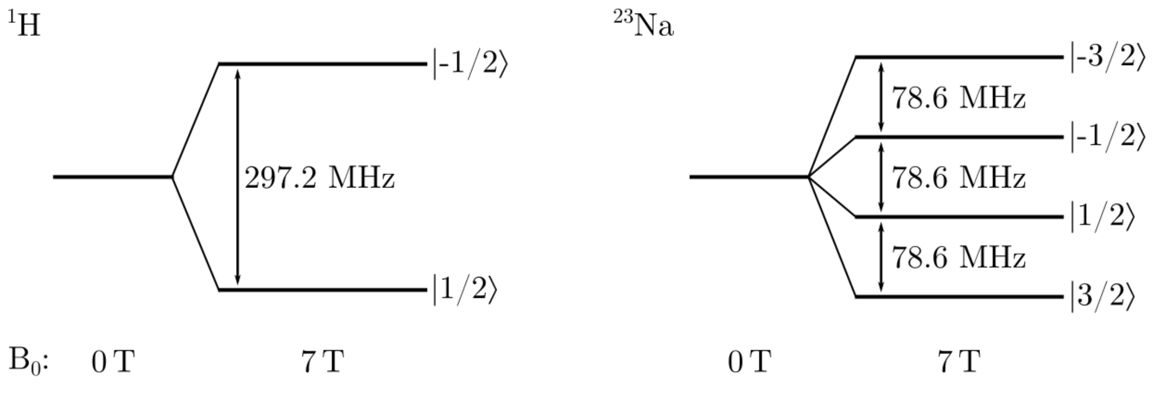

Figure 1: Zeeman splitting of hydrogen and sodium at 7 T.

The occupation numbers of the energy levels in thermal equilibrium follow a Fermi-Dirac statistic, since both ^{1}H and ^{23}Na ions are fermions. However, in the high temperature regime, which is well fulfilled in clinical NMR experiments, their occupation can be approximated by a Boltzmann distribution

$$p(E_m) = \frac{1}{Z} e^{-\frac{E_m}{k_B T}} \tag{2.10}$$

with the canonical partition function

$$Z = \sum_{m=-I}^{I} e^{-\frac{E_m}{k_B T}}. \tag{2.11}$$

Here, k_B corresponds to the Boltzmann constant and T is the temperature.
The detected NMR signal is given by the superposition of all magnetic moments in the sample, which motivates introducing the macroscopic magnetization $\vec{M}$. This allows a semi-classically description of the system since the quantum mechanical properties of the system vanish in the averaging, which is termed correspondence principle. The macroscopic magnetization $\vec{M}$ can be constructed by summation of the expectation values of the magnetic moments $\vec{\mu}$ per volume V:

$$\vec{M} = \frac{1}{V} \sum_i \langle \vec{\mu_i} \rangle = \frac{1}{V} \sum_i \gamma \langle \vec{I_i} \rangle \tag{2.12}$$

In thermal equilibrium the expectation values $\langle I_x \rangle$ and $\langle I_y \rangle$ vanish and only $\langle I_z \rangle$ comprises a finite value, where the first order Taylor series yields the macroscopic z-magnetization:

$$M_z = \frac{N}{V} \gamma \langle I_z \rangle = \frac{N}{V} \frac{\gamma^2 \hbar^2 I(I+1) B_0}{3 k_B T}. \tag{2.13}$$

In the following, the magnetization in thermal equilibrium will be termed $\vec{M}_0$.

2.2 Spin dynamics of spin 1/2 nuclei

The temporal evolution of the expectation value of the magnetic moment is given by the von-Neumann equation

$$\frac{\partial\langle\vec{\mu}\rangle}{\partial t} = \langle -\frac{i}{\hbar}\,[\vec{\mu}, \mathcal{H}]\rangle, \tag{2.14}$$

which transforms, using equations 2.2 and 2.6, to

$$\frac{\partial\langle\vec{\mu}\rangle}{\partial t} = \vec{\mu} \times \gamma\vec{B}. \tag{2.15}$$

This result translates to the macroscopic magnetization for a non-interaction magnetization vector as:

$$\frac{\partial\vec{M}}{\partial t} = \vec{M} \times \gamma\vec{B_0}. \tag{2.16}$$

Therefore, tipping $\vec{M}$ about a given FA with respect to the z-axis results in a precession motion around the z-axis with the Larmor frequency. This precession generates the measured NMR signal by inducing a voltage in the receive radiofrequency (RF) coils. Excitation is achieved by applying an RF excitation pulse that creates a magnetic field B_1, which is oriented perpendicular to the main magnetic field:

$$\vec{B_1} = B_1 \begin{pmatrix} \cos(\omega_{RF}t) \\ \sin(\omega_{RF}t) \\ 0 \end{pmatrix}. \tag{2.17}$$

In a coordinate system rotating with ω_0, marked in the following with the asterisk $*$, the equation of motion 2.16 in presence of an RF field transforms to

$$\begin{aligned} \left(\frac{\partial\vec{M}}{\partial t}\right)^* &= \vec{M} \times \begin{pmatrix} \omega_1 \\ 0 \\ \omega_0 - \omega_{RF} \end{pmatrix} \\ &= \gamma\vec{M} \times \vec{B_{eff}}, \end{aligned} \tag{2.18}$$

where $\omega_1 = \gamma B_1$. If the RF pulse is applied with the Larmor frequency ($\omega_{RF} = \omega_0$), the resonance condition is met and the z^*-entry vanishes and the FA after time t is then given by

$$\alpha(t) = \int_0^t \gamma B_1(t')dt'. \tag{2.19}$$

The magnetization in an excited system in free precession relaxes towards thermal equilibrium. The change in occupation numbers and therefore the longitudinal magnetization $M_\| = M_z$ is described by the time constant T_1, which is also referred to as the spin-lattice relaxation time. Here, energy is dissipated into molecular motion. Simultaneously a loss of phase coherence in the transverse magnetization $M_\perp = M_x + iM_y$ can be observed, described by the spin-spin relaxation time T_2.
Empirical observation of these processes resulted in formulation of the Bloch-equations

$$\begin{aligned}
\frac{\mathrm{d}M_x(t)}{\mathrm{d}t} &= \gamma\left(\vec{M}\times\vec{B}\right)_x - \frac{M_x(t)}{T_2} \\
\frac{\mathrm{d}M_y(t)}{\mathrm{d}t} &= \gamma\left(\vec{M}\times\vec{B}\right)_y - \frac{M_y(t)}{T_2} \\
\frac{\mathrm{d}M_z(t)}{\mathrm{d}t} &= \gamma\left(\vec{M}\times\vec{B}\right)_z - \frac{M_z(t)-M_0}{T_1}.
\end{aligned} \tag{2.20}$$

In the rotating frame, the solutions in absence of an RF field are given by

$$M_\perp(t) = M_\perp(0)e^{-\frac{t}{T_2}} \tag{2.21}$$

and

$$M_\|(t) = M_0 - \left(M_0 - M_\|(0)\right)e^{-\frac{t}{T_1}}. \tag{2.22}$$

For an inversion recovery (IR) experiment, where an 180° pulse is applied, equation 2.22 reduces to

$$M_\|(t) = M_0\left(1 - 2e^{-\frac{t}{T_1}}\right). \tag{2.23}$$

2.3 Spin dynamics of spin 3/2 nuclei

In this section, the spin dynamics of spin 3/2 particles are described, which constitute the basis for the quantitative signal simulations used in the 3D fingerprinting framework. For a more detailed description the reader is referred to [19, 20, 21], on which this section is based on.

2.3.1 Density matrix and ISTOs

A macroscopic description of the state of a spin 3/2 system can be described by the density matrix ρ, in which each entry ρ_{ij} corresponds to a transition from state i to state j:

$$\rho = \sum_{ij} \rho_{ij} |i\rangle\langle j| = \begin{pmatrix} \rho_{11} & \rho_{12} & \rho_{13} & \rho_{14} \\ \rho_{21} & \rho_{22} & \rho_{23} & \rho_{24} \\ \rho_{31} & \rho_{32} & \rho_{33} & \rho_{34} \\ \rho_{41} & \rho_{42} & \rho_{42} & \rho_{44} \end{pmatrix} \tag{2.24}$$

Here, $|i\rangle \in \{|1\rangle, |2\rangle, |3\rangle, |4\rangle\}$ represent the eigenstates of I_z, where the magnetic quantum numbers $m \in \{-\frac{3}{2}, -\frac{1}{2}, \frac{1}{2}, \frac{3}{2}\}$ are the corresponding eigenvalues. Transitions for which $|i - j| = 1$ and combinations of the latter correspond to single quantum coherences, whereas $|i - j| = 2$ and $|i - j| = 3$ are referred to as double and triple quantum coherences, respectively.

A convenient representation of the density matrix for systems with spin $\geq 3/2$ is achieved by the use of ISTOs, due to their rotational symmetry. For a spin 3/2 system, 16 operators T_{lm} with rank $l \in \{0, 1, 2, 3\}$ and order $m \in \{-l, -l+1, ..., l\}$ are required to describe the system.

They are summarized in table 1 and their matrix representation can be found in appendix 7.2.

The density matrix ρ can be expressed as a linear combination of ISTOs:

$$\rho = \sum_{lm} c_{lm} T_{lm}. \tag{2.25}$$

In the following, the symmetric and anti-symmetric tensor combinations

$$\begin{aligned} T_{lm}(s) &= \frac{1}{\sqrt{2}} \left(T_{l-m} + T_{lm} \right) \\ T_{lm}(a) &= \frac{1}{\sqrt{2}} \left(T_{l-m} - T_{lm} \right) \end{aligned} \tag{2.26}$$

Table 1: Overview on the ISTOs and their Cartesian representation. Here, $I_\pm = I_x \pm iI_y$ was used. Table adapted from [21].

Operator	Cartesian representation	Meaning
T_{00}	$\mathbb{1}$	Identity
T_{10}	I_z	Longitudinal magnetization
$T_{1\pm1}$	$\mp\frac{1}{\sqrt{2}}I_\pm$	Rank 1 single quantum coherence
T_{20}	$\frac{1}{\sqrt{6}}\left(3I_z^2 - I(I+1)\right)$	Quadrupolar order
$T_{2\pm1}$	$\mp\frac{1}{2}\left\{I_z, I_\pm\right\}$	Rank 2 single quantum coherence
$T_{2\pm2}$	$\frac{1}{2}I_\pm^2$	Rank 2 double quantum coherence
T_{30}	$\frac{1}{\sqrt{10}}\left(5I_z^3 - (3I(I+1)-1)I_z\right)$	Octopolar order
$T_{3\pm1}$	$\mp\frac{1}{4}\sqrt{\frac{3}{10}}\left\{5I_z^3 - I(I+1) - \frac{1}{2}, I_\pm\right\}$	Rank 3 single quantum coherence
$T_{3\pm2}$	$\frac{1}{2}\sqrt{\frac{3}{4}}\left\{I_z, I_\pm^2\right\}$	Rank 3 double quantum coherence
$T_{3\pm3}$	$\mp\frac{1}{2\sqrt{2}}I_\pm^3$	Rank 3 triple quantum coherence

and the normalizations

$$\begin{aligned}
\hat{T}_{00} &= \frac{1}{2}T_{00} \\
\hat{T}_{1m} &= \frac{1}{\sqrt{5}}T_{1m} \\
\hat{T}_{2m} &= \frac{1}{2\sqrt{2}}T_{2m} \\
\hat{T}_{3m} &= \frac{\sqrt{2}}{3}T_{3m}
\end{aligned} \tag{2.27}$$

are used.

2.3.2 Interaction of spin 3/2 systems

Assuming no fields except a static magnetic field B_0 in z-direction, the Zeeman Hamiltonian is given by

$$\mathcal{H}_0 = \gamma B_0 I_z = \omega_0 I_z = \omega_0 T_{10}. \tag{2.28}$$

The use of Boltzmann statistics in conjunction with the high temperature approximation yields the density matrix in thermal equilibrium:

$$\rho_0 = \frac{1}{Z}e^{\frac{\omega_0 T_{10}}{kT}} \approx \frac{1}{4}\mathbb{1} + \frac{\omega_0}{4kT}T_{10} \text{ with } Z = \mathrm{Tr}\left(e^{\frac{\omega_0 T_{10}}{kT}}\right). \tag{2.29}$$

Since the identity matrix $\mathbb{1}$ has no influence on temporal evolution and gives no signal contribution, the equilibrium magnetization is often referred to as

$$\rho_0 = \frac{\omega_0}{4kT} T_{10}. \tag{2.30}$$

The temporal evolution of the density matrix can be described in dependence of the Hamiltonian, which itself consists out of the individual Hamiltonians of static magnetic fields, RF pulses as well as static and fluctuating quadrupolar interactions. A basis transformation into a frame rotating with the Larmor frequency results in vanishing of the Zeeman-Hamiltonian $\mathcal{H}_0 = \omega_0 T_{10}$. Any arbitrary Hamiltonian transforms as

$$\mathcal{H}^* = e^{i\mathcal{H}_0 t} \mathcal{H} e^{-i\mathcal{H}_0 t} \tag{2.31}$$

and the density matrix is given by

$$\rho^* = e^{i\mathcal{H}_0 t} \rho e^{-i\mathcal{H}_0 t}, \tag{2.32}$$

where the asterisk $*$ marks the rotating frame.

Excitation of the system can be achieved by applying an RF field. An on-resonant RF field in x^*-direction with field strength B_1 yields

$$\mathcal{H}_1^* = \omega_1 I_x = \omega_1 T_{11}(a) = \sqrt{5}\omega_1 \hat{T}_{11}(a), \tag{2.33}$$

where the excitation frequency

$$\omega_1 = -\gamma B_1 \tag{2.34}$$

was used.

A non-zero pulse phase relative to the x^*-direction can be described by a change of basis prior and subsequent to the pulse:

$$\begin{aligned} T_{lm}(s) &= T_{lm}(s)\cos(m\phi) + iT_{lm}(a)\sin(m\phi) \\ T_{lm}(a) &= T_{lm}(a)\cos(m\phi) + iT_{lm}(s)\sin(m\phi) \end{aligned} \tag{2.35}$$

Due to their non-spherical charge distribution, spin 3/2 nuclei experience quadrupolar interactions with surrounding electrical field gradients (EFGs), which dominate their relaxation behaviour and can result in shifting of the energy levels and consequently splitting of the resonance lines. One can differentiate between fluctuating and static quadrupolar interactions. The former temporally average to zero and can for example be generated by the atomic charges on macromolecules, ions or contributions from the ion hydration shell [19]. The static quadrupolar coupling, on the other hand, is the part that persists after temporal averaging.

Assuming cylindrical static quadrupolar interactions, the Hamiltonian can be expressed as

$$\mathcal{H}^*_{QS} = \omega_Q \frac{3I_z^2 - I(I+1)}{6} = \omega_Q \hat{T}_{20}. \tag{2.36}$$

Here, ω_Q describes the residual quadrupolar coupling, which corresponds to the remaining part of quadrupolar interaction after temporal averaging. For each domain, that is the entirety of spins experiencing the same dynamic properties, the residual quadrupolar coupling can be expressed as

$$\omega_Q = \frac{\overline{\omega_Q}}{2}\left(3\cos^2(\theta) - 1\right). \tag{2.37}$$

Here, the angle θ describes the local director relative to the direction of the static magnetic field and $\overline{\omega_Q}$ the maximum splitting for $\theta = 0$.

The zero-average fluctuating quadrupolar interactions can be described by interactions of the nuclei with fluctuating EFGs of the environment, yielding the Hamiltonian

$$\mathcal{H}^*_{QF}(t) = C_Q \sum_{m=-2}^{2} (-1)^m T_{2m} e^{im\omega_0 t} \left(F_{2-m} - \langle F_{2-m}\rangle\right) \text{ with } C_Q = \frac{eQ}{\hbar\sqrt{6}}, \tag{2.38}$$

where Q corresponds to the quadrupolar moment of the nucleus. F_{2m} and $\langle F_{2m}\rangle$ describe the components of EFG tensor and their time-averaged means:

$$\begin{aligned} F_{20} &= \frac{1}{2}V_{zz} \\ F_{2\pm1} &= \frac{1}{\sqrt{6}}\left(V_{xz} \pm iV_{yz}\right) \\ F_{2\pm2} &= \frac{1}{2\sqrt{6}}\left(V_{xx} - V_{yy} \pm i2V_{xy}\right). \end{aligned} \tag{2.39}$$

2.3.3 Temporal evolution of the density matrix

The temporal evolution of the density matrix under a static Hamiltonian $\mathcal{H}^*_S$ results in the master equation

$$\frac{\mathrm{d}\rho^*}{\mathrm{d}t} = -i\left[\mathcal{H}^*_S, \rho^*\right], \tag{2.40}$$

where the Hamiltonian is given by

$$\mathcal{H}_S^* = \mathcal{H}_1^* + \mathcal{H}_{QS}^*. \tag{2.41}$$

Hence, expressing the master equation in terms of ISTOs yields

$$\frac{\mathrm{d}\rho^*}{\mathrm{d}t} = -i\left[\omega_Q\hat{T}_{20} + \sqrt{5}\omega_1\hat{T}_{11}(a), \rho^*\right]. \tag{2.42}$$

Equation 2.42 can be reduced to two sets of coupled differential equations

$$\begin{aligned}
\frac{\mathrm{d}}{\mathrm{d}t}\begin{pmatrix} \hat{T}_{10} \\ \hat{T}_{11}(s) \\ \hat{T}_{21}(a) \\ \hat{T}_{22}(a) \\ \hat{T}_{30} \\ \hat{T}_{31}(s) \\ \hat{T}_{32}(s) \\ \hat{T}_{33}(s) \end{pmatrix} = &\left(\begin{matrix} 0 & -i\omega_1 & 0 & 0 \\ -i\omega_1 & 0 & i\sqrt{\frac{3}{5}}\omega_Q & 0 \\ 0 & i\sqrt{\frac{3}{5}}\omega_Q & 0 & -i\omega_1 \\ 0 & 0 & -i\omega_1 & 0 \\ 0 & 0 & 0 & 0 \\ 0 & 0 & i\sqrt{\frac{2}{5}}\omega_Q & 0 \\ 0 & 0 & 0 & i\omega_Q \\ 0 & 0 & 0 & 0 \end{matrix}\right. \cdots \\
&\cdots \left.\begin{matrix} 0 & 0 & 0 & 0 \\ 0 & 0 & 0 & 0 \\ 0 & i\sqrt{\frac{2}{5}}\omega_Q & 0 & 0 \\ 0 & 0 & i\omega_Q & 0 \\ 0 & -i\sqrt{6}\omega_1 & 0 & 0 \\ -i\sqrt{6}\omega_1 & 0 & -i\sqrt{\frac{5}{2}}\omega_1 & 0 \\ 0 & -i\sqrt{\frac{5}{2}}\omega_1 & 0 & -i\sqrt{\frac{3}{2}}\omega_1 \\ 0 & 0 & -i\sqrt{\frac{3}{2}}\omega_1 & 0 \end{matrix}\right)\begin{pmatrix} \hat{T}_{10} \\ \hat{T}_{11}(s) \\ \hat{T}_{21}(a) \\ \hat{T}_{22}(a) \\ \hat{T}_{30} \\ \hat{T}_{31}(s) \\ \hat{T}_{32}(s) \\ \hat{T}_{33}(s) \end{pmatrix}
\end{aligned} \tag{2.43}$$

and

$$\frac{\mathrm{d}}{\mathrm{d}t}\begin{pmatrix}\hat{T}_{11}(a)\\ \hat{T}_{20}\\ \hat{T}_{21}(s)\\ \hat{T}_{22}(s)\\ \hat{T}_{31}(a)\\ \hat{T}_{32}(a)\\ \hat{T}_{33}(a)\end{pmatrix} = \left(\begin{matrix} 0 & 0 & i\sqrt{\frac{3}{5}}\omega_Q & 0 \\ 0 & 0 & -i\sqrt{3}\omega_1 & 0 \\ i\sqrt{\frac{3}{5}}\omega_Q & -i\sqrt{3}\omega_1 & 0 & -i\omega_1 \\ 0 & 0 & -i\omega_1 & 0 \\ 0 & 0 & i\sqrt{\frac{2}{5}}\omega_Q & 0 \\ 0 & 0 & 0 & i\omega_Q \\ 0 & 0 & 0 & 0 \end{matrix}\right. \cdots \tag{2.44}$$

$$\cdots \left.\begin{matrix} 0 & 0 & 0 \\ 0 & 0 & 0 \\ i\sqrt{\frac{2}{5}}\omega_Q & 0 & 0 \\ 0 & i\omega_Q & 0 \\ 0 & -i\sqrt{\frac{5}{2}}\omega_1 & 0 \\ -i\sqrt{\frac{5}{2}}\omega_1 & 0 & -i\sqrt{\frac{3}{2}}\omega_1 \\ 0 & -i\sqrt{\frac{3}{2}}\omega_1 & 0 \end{matrix}\right)\begin{pmatrix}\hat{T}_{11}(a)\\ \hat{T}_{20}\\ \hat{T}_{21}(s)\\ \hat{T}_{22}(s)\\ \hat{T}_{31}(a)\\ \hat{T}_{32}(a)\\ \hat{T}_{33}(a)\end{pmatrix}.$$

In the Redfield relaxation theory, which is based on perturbation theory, the fluctuating quadrupolar interactions yield the relaxation operator

$$f(\rho^*) = -\int_0^\infty \langle \left[\mathcal{H}^*_{QF}(t), \left[e^{-i\mathcal{H}^*_S\tau}\mathcal{H}^*_{QF}(t-\tau)e^{i\mathcal{H}^*_S\tau}, \rho^*(t)\right]\right]\rangle\, \mathrm{d}\tau, \tag{2.45}$$

resulting in the new master equation

$$\frac{\mathrm{d}\rho^*}{\mathrm{d}t} = -i\left[\mathcal{H}^*_S, \rho^*\right] + f(\rho^*). \tag{2.46}$$

Using equation 2.38 and neglecting terms oscillating with multiples of ω_0, equation 2.45 transforms to

$$\begin{aligned} f(\rho^*) = &- C_Q^2 \sum_{m=-2}^{2}\int_0^\infty \left[T_{2m}, \left[e^{-i\mathcal{H}^*_S\tau}T^\dagger_{2m}e^{i\mathcal{H}^*_S\tau}, \rho^*(t)\right]\right] \\ &\langle\left(F^*_{2m}(t) - \langle F^*_{2m}\rangle\right)\left(F_{2m}(t-\tau) - \langle F_{2m}\rangle\right)\rangle e^{im\omega_0\tau}\,\mathrm{d}\tau. \end{aligned} \tag{2.47}$$

The relaxation term reduces to complex spectral density functions at a number of frequencies. In the following, the imaginary part K_m of the spectral density functions will be ignored, as it results in only very small, second-order frequency shifts and in a weak coupling of the two sets of differential equations. The real part is given by

$$J_m(\omega) = \frac{6C_Q^2}{2} \int_{-\infty}^{\infty} \langle \left(F_{2m}^*(t) - \langle F_{2m}^* \rangle \right) \left(F_{2m}(t-\tau) - \langle F_{2m} \rangle \right) \rangle e^{i\omega\tau} \, \mathrm{d}\tau. \tag{2.48}$$

$f(\rho^*)$ includes terms proportional to $J_m(m\omega_0 \pm \lambda_i)$, where λ_i are the eigenvalues of equations 2.43 and 2.44. However, for the case $m \neq 0$ we will approximate $J_m(m\omega_0 \pm \lambda_i) \approx J_m(m\omega_0)$ in the following, since ω_0 is generally much larger than λ_i. Hence, $\mathcal{H}_S^*$ commutes with T_{2m} and vanishes in equation 2.47.

Consequently, the temporal evolution of the density matrix under relaxation can be described by

$$\frac{\mathrm{d}}{\mathrm{d}t} \begin{pmatrix} \hat{T}_{10} \\ \hat{T}_{11}(s) \\ \hat{T}_{21}(a) \\ \hat{T}_{22}(a) \\ \hat{T}_{30} \\ \hat{T}_{31}(s) \\ \hat{T}_{32}(s) \\ \hat{T}_{33}(s) \end{pmatrix} = - \left(\begin{matrix} \frac{2}{5}J_1 + \frac{8}{5}J_2 & 0 & 0 & 0 \\ 0 & J_1 + \frac{2}{5}J_2 & 0 & 0 \\ 0 & 0 & J_1 + 2J_2 & 0 \\ 0 & 0 & 0 & 2J_1 + J_2 \\ \frac{4}{5}J_1 - \frac{4}{5}J_2 & 0 & 0 & 0 \\ 0 & -\frac{\sqrt{6}}{5}J_2 & 0 & 0 \\ 0 & 0 & 0 & 0 \\ 0 & 0 & 0 & 0 \end{matrix} \right. \cdots$$

$$\cdots \left. \begin{matrix} \frac{4}{5}J_1 - \frac{4}{5}J_2 & 0 & 0 & 0 \\ 0 & -\frac{\sqrt{6}}{5}J_2 & 0 & 0 \\ 0 & 0 & 0 & 0 \\ 0 & 0 & 0 & 0 \\ \frac{8}{5}J_1 + \frac{2}{5}J_2 & 0 & 0 & 0 \\ 0 & J_1 + \frac{3}{5}J_2 & 0 & 0 \\ 0 & 0 & J_2 & 0 \\ 0 & 0 & 0 & J_1 + J_2 \end{matrix} \right) \begin{pmatrix} \hat{T}_{10} \\ \hat{T}_{11}(s) \\ \hat{T}_{21}(a) \\ \hat{T}_{22}(a) \\ \hat{T}_{30} \\ \hat{T}_{31}(s) \\ \hat{T}_{32}(s) \\ \hat{T}_{33}(s) \end{pmatrix} \tag{2.49}$$

and

$$\frac{\mathrm{d}}{\mathrm{d}t}\begin{pmatrix}\hat{T}_{11}(a)\\ \hat{T}_{20}\\ \hat{T}_{21}(s)\\ \hat{T}_{22}(s)\\ \hat{T}_{31}(a)\\ \hat{T}_{32}(a)\\ \hat{T}_{33}(a)\end{pmatrix} = -\left(\begin{matrix} J_1+\frac{2}{5}J_2 & 0 & 0 & 0\\ 0 & 2J_1+2J_2 & 0 & 0\\ 0 & 0 & J_1+2J_2 & 0\\ 0 & 0 & 0 & 2J_1+J_2 \cdots\\ -\frac{\sqrt{6}}{5}J_2 & 0 & 0 & 0\\ 0 & 0 & 0 & 0\\ 0 & 0 & 0 & 0\end{matrix}\right. \tag{2.50}$$

$$\left.\begin{matrix} & -\frac{\sqrt{6}}{5}J_2 & 0 & 0\\ & 0 & 0 & 0\\ & 0 & 0 & 0\\ \cdots & 0 & 0 & 0\\ & J_1+\frac{3}{5}J_2 & 0 & 0\\ & 0 & J_2 & 0\\ & 0 & 0 & J_1+J_2\end{matrix}\right)\begin{pmatrix}\hat{T}_{11}(a)\\ \hat{T}_{20}\\ \hat{T}_{21}(s)\\ \hat{T}_{22}(s)\\ \hat{T}_{31}(a)\\ \hat{T}_{32}(a)\\ \hat{T}_{33}(a)\end{pmatrix},$$

where $J_1 = J_1(\omega_0)$ and $J_2 = J_2(2\omega_0)$ were used.

For the case $m = 0$ these assumptions do not hold true and a full evaluation of $f(\rho^*)$ is necessary. The relaxation rates are then dependent on the spectral density at the frequencies 0, λ_1 and λ_2, which themselves are given by:

$$\begin{aligned}\lambda_1 &= \sqrt{\omega_Q^2 + 2\omega_Q\omega_1 + 4\omega_1^2}\\ \lambda_2 &= \sqrt{\omega_Q^2 - 2\omega_Q\omega_1 + 4\omega_1^2}.\end{aligned} \tag{2.51}$$

Neglecting low-frequency dispersion in the order of $\lambda_{1,2}$ yields $J_0(0) \approx J_0(\lambda_1) \approx J_0(\lambda_2)$, resulting in the differential equations for $m = 0$ to be

$$\frac{\mathrm{d}}{\mathrm{d}t}\begin{pmatrix}\hat{T}_{10}\\ \hat{T}_{11}(s)\\ \hat{T}_{21}(a)\\ \hat{T}_{22}(a)\\ \hat{T}_{30}\\ \hat{T}_{31}(s)\\ \hat{T}_{32}(s)\\ \hat{T}_{33}(s)\end{pmatrix} = -\begin{pmatrix}0 & 0 & 0 & 0 & 0 & 0 & 0 & 0\\ 0 & \frac{3}{5}J_0 & 0 & 0 & 0 & \frac{\sqrt{6}}{5}J_0 & 0 & 0\\ 0 & 0 & J_0 & 0 & 0 & 0 & 0 & 0\\ 0 & 0 & 0 & J_0 & 0 & 0 & 0 & 0\\ 0 & 0 & 0 & 0 & 0 & 0 & 0 & 0\\ 0 & \frac{\sqrt{6}}{5}J_0 & 0 & 0 & 0 & \frac{2}{5}J_0 & 0 & 0\\ 0 & 0 & 0 & 0 & 0 & 0 & J_0 & 0\\ 0 & 0 & 0 & 0 & 0 & 0 & 0 & 0\end{pmatrix}\begin{pmatrix}\hat{T}_{10}\\ \hat{T}_{11}(s)\\ \hat{T}_{21}(a)\\ \hat{T}_{22}(a)\\ \hat{T}_{30}\\ \hat{T}_{31}(s)\\ \hat{T}_{32}(s)\\ \hat{T}_{33}(s)\end{pmatrix} \tag{2.52}$$

and

$$\frac{\mathrm{d}}{\mathrm{d}t}\begin{pmatrix}\hat{T}_{11}(a)\\ \hat{T}_{20}\\ \hat{T}_{21}(s)\\ \hat{T}_{22}(s)\\ \hat{T}_{31}(a)\\ \hat{T}_{32}(a)\\ \hat{T}_{33}(a)\end{pmatrix} = -\begin{pmatrix}\frac{3}{5}J_0 & 0 & 0 & 0 & \frac{\sqrt{6}}{5}J_0 & 0 & 0\\ 0 & 0 & 0 & 0 & 0 & 0 & 0\\ 0 & 0 & J_0 & 0 & 0 & 0 & 0\\ 0 & 0 & 0 & J_0 & 0 & 0 & 0\\ \frac{\sqrt{6}}{5}J_0 & 0 & 0 & 0 & \frac{2}{5}J_0 & 0 & 0\\ 0 & 0 & 0 & 0 & 0 & J_0 & 0\\ 0 & 0 & 0 & 0 & 0 & 0 & 0\end{pmatrix}\begin{pmatrix}\hat{T}_{11}(a)\\ \hat{T}_{20}\\ \hat{T}_{21}(s)\\ \hat{T}_{22}(s)\\ \hat{T}_{31}(a)\\ \hat{T}_{32}(a)\\ \hat{T}_{33}(a)\end{pmatrix}. \tag{2.53}$$

Hence, the temporal evolution of the basis operators under the static Hamiltonian including relaxation effects is given by two equations: the sum of equations 2.43, 2.49 2.52 and the sum of equations 2.44, 2.50 and 2.53. Both these equations can be expressed as

$$\frac{\mathrm{d}T}{\mathrm{d}t} = MT, \tag{2.54}$$

where T is given by $\left(\hat{T}_{10}, \hat{T}_{11}(s), \hat{T}_{21}(a), \hat{T}_{22}(a), \hat{T}_{30}, \hat{T}_{31}(s), \hat{T}_{32}(s), \hat{T}_{33}(s)\right)^T$ for the first equation and $\left(\hat{T}_{11}(a), \hat{T}_{20}, \hat{T}_{21}(s), \hat{T}_{22}(s), \hat{T}_{31}(a), \hat{T}_{32}(a), \hat{T}_{33}(a)\right)^T$ for the second equation. The solution of equation 2.54 is given by

$$T(t) = Se^{M_d t}S^{-1}T(0). \tag{2.55}$$

Here, $T(0)$ is the initial condition, M_d is the diagonal form of M and S the corresponding similarity transform:

$$M_d = S^{-1}MS. \tag{2.56}$$

Relaxation towards thermal equilibrium can be implemented by adding terms proportional to the identity T_{00} to equation 2.54 [3].

The effects of off-resonances can be implemented by addition of

$$\frac{\mathrm{d}}{\mathrm{d}t}\begin{pmatrix}\hat{T}_{lm}(s)\\ \hat{T}_{lm}(a)\end{pmatrix} = \begin{pmatrix}0 & im\omega_{off}\\ im\omega_{off} & 0\end{pmatrix}\begin{pmatrix}\hat{T}_{lm}(s)\\ \hat{T}_{lm}(a)\end{pmatrix}. \tag{2.57}$$

The full resulting equation of motion, used for numeric solving of the temporal density matrix evolution in this work, can be found in the appendix in equations 7.1 and 7.2.

2.3.4 Relaxation

Equation 2.54 contains the full information on the temporal evolution of the spin operators. However, there are analytical solutions for thermal relaxation in absence of an RF pulse, which are discussed in the following.
Exploiting equations 2.36, 2.38 and 2.45 yields the temporal evolution of the density matrix:

$$\frac{\mathrm{d}\rho^*}{\mathrm{d}t} = -i\frac{\omega_Q}{\sqrt{6}}\left[T_{20},\rho^*\right] - \sum_{m=-2}^{2}\left[T_{2m},\left[T_{2m},\rho^*\right]\right]\left(J_m(m\omega_0) + iK_m(m\omega_0)\right). \tag{2.58}$$

The temporal evolution of the polarization tensors $\hat{T}_{10}$, $\hat{T}_{20}$ and $\hat{T}_{30}$ can be expressed as

$$\frac{\mathrm{d}}{\mathrm{d}t}\begin{pmatrix}\hat{T}_{10}\\ \hat{T}_{30}\end{pmatrix} = -\begin{pmatrix}\frac{2}{5}J_1 + \frac{8}{5}J_2 & \frac{4}{5}J_1 - \frac{4}{5}J_2\\ \frac{4}{5}J_1 - \frac{4}{5}J_2 & \frac{8}{5}J_1 + \frac{2}{5}J_2\end{pmatrix}\begin{pmatrix}\hat{T}_{10}\\ \hat{T}_{30}\end{pmatrix} \tag{2.59}$$

and

$$\frac{\mathrm{d}}{\mathrm{d}t}\hat{T}_{20} = -\left(2J_1 + 2J_2\right)\hat{T}_{20}. \tag{2.60}$$

The solution of equation 2.59 in arrow notation is given by

$$\begin{aligned}\hat{T}_{10} &\xrightarrow{R^{(0)}} \hat{T}_{10}f_{11}^{(0)}(t) + \hat{T}_{30}f_{31}^{(0)}(t)\\ \hat{T}_{30} &\xrightarrow{R^{(0)}} \hat{T}_{30}f_{33}^{(0)}(t) + \hat{T}_{10}f_{13}^{(0)}(t),\end{aligned} \tag{2.61}$$

where the index (0) labels quantum coherences of order zero and $f(t)$ is the biexponential relaxation function:

$$\begin{aligned} f_{11}^{(0)}(t) &= \frac{1}{5}\left(e^{-R_1^{(0)}t} + 4e^{-R_2^{(0)}t}\right) \\ f_{13}^{(0)}(t) = f_{31}^{(0)}(t) &= \frac{2}{5}\left(e^{-R_1^{(0)}t} - e^{-R_2^{(0)}t}\right) \\ f_{33}^{(0)}(t) &= \frac{1}{5}\left(4e^{-R_1^{(0)}t} + e^{-R_2^{(0)}t}\right). \end{aligned} \tag{2.62}$$

Here, the relaxation rates $R_1^{(0)}$ and $R_2^{(0)}$ correspond to

$$\begin{aligned} R_1^{(0)} &= \frac{1}{T_{1s}} = 2J_1 \\ R_2^{(0)} &= \frac{1}{T_{1l}} = 2J_2, \end{aligned} \tag{2.63}$$

where T_{1s} and T_{1l} are the short and long longitudinal relaxation times.
Equation 2.60 can be solved by

$$\hat{T}_{20} \xrightarrow{R^{(0)}} \hat{T}_{20} f_{22}^{(0)}(t), \tag{2.64}$$

where the relaxation function and the corresponding relaxation rate are given by

$$f_{11}^{(0)}(t) = e^{-R_3^{(0)}t} \tag{2.65}$$

and

$$R_3^{(0)} = 2J_1 + 2J_2. \tag{2.66}$$

For the consideration of single and multi-quantum coherences, contributions of the imaginary part K_m of the spectral density function are neglected since they are very small. Single quantum coherences, which are equivalent to the transverse relaxation of the measured NMR signal, can be described by

$$\frac{\mathrm{d}}{\mathrm{d}t}\begin{pmatrix}\hat{T}_{11}(a,s)\\ \hat{T}_{21}(s,a)\\ \hat{T}_{31}(a,s)\end{pmatrix} = -\left(\begin{matrix}\frac{3}{5}J_0+J_1+\frac{2}{5}J_2 & -i\sqrt{\frac{3}{5}}\omega_Q\\ -i\sqrt{\frac{3}{5}}\omega_Q & J_0+J_1+2J_2\\ \frac{\sqrt{6}}{5}\left(J_0-J_2\right) & -i\sqrt{\frac{2}{5}}\omega_Q\end{matrix}\right. \cdots \tag{2.67}$$

$$\cdots \left.\begin{matrix}\frac{\sqrt{6}}{5}\left(J_0-J_2\right)\\ -i\sqrt{\frac{2}{5}}\omega_Q\\ \frac{2}{5}J_0+J_1+\frac{3}{5}J_2\end{matrix}\right)\begin{pmatrix}\hat{T}_{11}(a,s)\\ \hat{T}_{21}(s,a)\\ \hat{T}_{31}(a,s)\end{pmatrix}.$$

The solution of the latter is

$$\begin{aligned}\hat{T}_{11}(a,s) &\xrightarrow{R^{(1)}} \hat{T}_{11}(a,s)f_{11}^{(1)}(t)+\hat{T}_{21}(s,a)f_{21}^{(1)}+\hat{T}_{31}(a,s)f_{31}^{(1)}(t)\\ \hat{T}_{21}(s,a) &\xrightarrow{R^{(1)}} \hat{T}_{11}(a,s)f_{12}^{(1)}(t)+\hat{T}_{21}(s,a)f_{22}^{(1)}+\hat{T}_{31}(a,s)f_{32}^{(1)}(t)\\ \hat{T}_{31}(a,s) &\xrightarrow{R^{(1)}} \hat{T}_{11}(a,s)f_{13}^{(1)}(t)+\hat{T}_{21}(s,a)f_{23}^{(1)}+\hat{T}_{31}(a,s)f_{33}^{(1)}(t),\end{aligned} \tag{2.68}$$

where the relaxation functions are

$$\begin{aligned}
f_{11}^{(1)}(t) &= \frac{1}{5}\left(\frac{3}{2}(1+\kappa^{(1)})e^{-R_1^{(1)}t}+2e^{-R_2^{(1)}t}+\frac{3}{2}(1-\kappa^{(1)})e^{-R_3^{(1)}t}\right)\\
f_{12}^{(1)}(t) = f_{21}^{(1)}(t) &= \frac{i}{2}\sqrt{\frac{3}{5}}\frac{\omega_Q}{\sqrt{J_2^2-\omega_Q^2}}\left(e^{-R_1^{(1)}t}-e^{-R_3^{(1)}t}\right)\\
f_{13}^{(1)}(t) = f_{31}^{(1)}(t) &= \frac{\sqrt{6}}{5}\left(\frac{1}{2}(1+\kappa^{(1)})e^{-R_1^{(1)}t}-e^{-R_2^{(1)}t}+\frac{1}{2}(1-\kappa^{(1)})e^{-R_3^{(1)}t}\right)\\
f_{22}^{(1)}(t) &= \frac{1}{2}\left((1-\kappa^{(1)})e^{-R_1^{(1)}t}+(1+\kappa^{(1)})e^{-R_3^{(1)}t}\right)\\
f_{23}^{(1)}(t) = f_{32}^{(1)}(t) &= \frac{i}{\sqrt{10}}\frac{\omega_Q}{\sqrt{J_2^2-\omega_Q^2}}\left(e^{-R_1^{(1)}t}-e^{-R_3^{(1)}t}\right)\\
f_{33}^{(1)}(t) &= \frac{1}{5}\left((1+\kappa^{(1)})e^{-R_1^{(1)}t}+3e^{-R_2^{(1)}t}+(1-\kappa^{(1)})e^{-R_3^{(1)}t}\right)
\end{aligned} \tag{2.69}$$

with

$$\begin{aligned}
\kappa^{(1)} &= \frac{J_2}{\sqrt{J_2^2 - \omega_Q^2}} \\
R_1^{(1)} &= \frac{1}{T_{2s}} = J_0 + J_1 + J_2 - \sqrt{J_2^2 - \omega_Q^2} \\
R_2^{(1)} &= \frac{1}{T_{2l}} = J_1 + J_2 \\
R_3^{(1)} &= J_0 + J_1 + J_2 + \sqrt{J_2^2 - \omega_Q^2}.
\end{aligned} \tag{2.70}$$

The short and long transverse relaxation times T_{2s} and T_{2l} define the biexponential free induction decay (FID) of a spin 3/2 system after excitation.

The temporal evolution of multi-quantum coherences ($m > 1$) are given by

$$\frac{\mathrm{d}}{\mathrm{d}t}\begin{pmatrix} \hat{T}_{22}(s,a) \\ \hat{T}_{32}(a,s) \\ \hat{T}_{33}(a,s) \end{pmatrix} = -\begin{pmatrix} J_0 + 2J_1 + J_2 & -i\omega_Q & 0 \\ -i\omega_Q & J_0 + J_2 & 0 \\ 0 & 0 & J_1 + J_2 \end{pmatrix}\begin{pmatrix} \hat{T}_{22}(s,a) \\ \hat{T}_{32}(a,s) \\ \hat{T}_{33}(a,s) \end{pmatrix}. \tag{2.71}$$

The solution is

$$\begin{aligned}
\hat{T}_{22}(s,a) &\xrightarrow{R^{(2)}} \hat{T}_{22}(s,a) f_{22}^{(2)}(t) + \hat{T}_{32}(a,s) f_{32}^{(2)}(t) \\
\hat{T}_{32}(a,s) &\xrightarrow{R^{(2)}} \hat{T}_{22}(s,a) f_{23}^{(2)}(t) + \hat{T}_{32}(a,s) f_{33}^{(2)}(t) \\
\hat{T}_{33}(a,s) &\xrightarrow{R^{(3)}} \hat{T}_{33}(a,s) f_{33}^{(3)}(t),
\end{aligned} \tag{2.72}$$

with the relaxation functions

$$\begin{aligned}
f_{22}^{(2)}(t) &= \frac{1}{2}\left((1+\kappa^{(2)})e^{-R_1^{(2)}t} + (1-\kappa^{(2)})e^{-R_2^{(2)}t}\right) \\
f_{23}^{(2)}(t) &= f_{32}^{(2)}(t) = -\frac{i}{2}\frac{\omega_Q}{\sqrt{J_1^2 - \omega_Q^2}}\left(e^{-R_1^{(2)}t} - e^{-R_2^{(2)}t}\right) \\
f_{33}^{(2)}(t) &= \frac{1}{2}\left((1-\kappa^{(2)})e^{-R_1^{(2)}t} + (1+\kappa^{(2)})e^{-R_2^{(2)}t}\right) \\
f_{33}^{(3)}(t) &= e^{-R_1^{(3)}t}
\end{aligned} \tag{2.73}$$

and the relaxation rates

$$\begin{aligned}
\kappa^{(2)} &= \frac{J_1}{\sqrt{J_1^2 - \omega_Q^2}} \\
R_1^{(2)} &= J_0 + J_1 + J_2 + \sqrt{J_1^2 - \omega_Q^2} \\
R_2^{(1)} &= J_0 + J_1 + J_2 - \sqrt{J_1^2 - \omega_Q^2} \\
R_1^{(3)} &= J_1 + J_2.
\end{aligned} \tag{2.74}$$

The considerations in this work are focused on isotropic environments, in which $\omega_Q = 0$. Consequently, equation 2.70 transforms to

$$\begin{aligned}
T_{2s} &= \frac{1}{J_0 + J_1} \\
T_{2l} &= \frac{1}{J_1 + J_2},
\end{aligned} \tag{2.75}$$

wherefore an FID decays with

$$S(t) = S_0 \left(0.6 e^{-\frac{t}{T_{2s}}} + 0.4 e^{-\frac{t}{T_{2l}}} \right). \tag{2.76}$$

An IR experiment can be described by:

$$S(t) = S_0 \left(1 - 2 \left(0.8 e^{-\frac{t}{T_{1l}}} + 0.2 e^{-\frac{t}{T_{1s}}} \right) \right). \tag{2.77}$$

2.4 Specific absorption rate

Excitation of the magnetization is achieved using RF pulses (see section 2.5) and results in a precession movement which generates the NMR signal. To ensure patient safety, the specific absorption rate (SAR), which describes the amount of power absorbed in the tissue, is strictly limited by the IEC-guidelines [22].
The SAR is limited for a mass of 10 g and both a 10 s and a 6 min window and is given by:

$$SAR = \frac{1}{2V} \int_t \int_V \frac{\sigma(\vec{r})}{\rho(\vec{r})} |\vec{E}(\vec{r})|^2, \tag{2.78}$$

where σ corresponds to the electrical conductivity and ρ is the density of the tissue.
If either the 10 s or the 6 min limit is reached, the measurement is aborted. Therefore, the excitation field B_1 is limited by the SAR constraints, since

$$|\vec{E}(\vec{r})|^2 \propto |\vec{B}_1(\vec{r})|^2 \propto \alpha^2, \tag{2.79}$$

where α is the FA. Hence, doubling the FA for a given pulse shape results in fourfold the SAR. This is a limiting factor in ultra-high field MRI, wherefore strategies such as variable-rate selective excitation (VERSE), as illustrated in section 2.5.1.3, are applied.

2.5 Magnetic resonance imaging

In magnetic resonance imaging, the magnetization is spatially encoded after magnetization preparation. The easiest example of an MRI sequence is given by an excitation pulse and subsequent spatial encoding, which will be discussed in the following. However, more complicated sequences of RF and gradient fields can be used to achieve a multitude of image contrasts [23], but their description lies beyond the scope of this work.

2.5.1 Selective and non-selective excitation

At the beginning of the pulse sequence, the magnetization is excited with an RF pulse, which results in precession of the magnetization and therefore the NMR signal is induced in the receive coils. A typical excitation pulse is composed of a pulse envelope modulated with the Larmor frequency, which is true for all RF pulses discussed in the following.

2.5.1.1 Non-selective excitation

The simplest excitation pulse is a rectangular (rect) pulse without presence of any gradient fields. Due to their absence, the magnetic field distribution is spatially independent and therefore all spins experience the same Larmor frequency. Consequently, the pulse non-selectively excites all spins similarly and a constant FA is achieved, when a homogenous B_1 distribution is assumed. A major advantage of this pulse type is its SAR-efficiency due to the constant amplitude. Further, the absence of gradient fields allows spatial encoding directly after the RF pulse since no gradient rewinders have to be used, as required for selective excitation. On the downside, however, spatial encoding of the entire magnetization in the coil is required to reconstruct artifact free images, as discussed in section 2.5.2. This can be time consuming and is therefore especially time-inefficient if only a small area is of interest.

2.5.1.2 Selective excitation

Selective excitation pulses only excite a certain area in the coil, leading to reduced time required for spatial encoding. The most common selective excitation pulse is a filtered sinc pulse, which is applied in conjunction with a slice selection gradient.

The bandwidth (BW) of the pulse determines the frequency band that is excited. Application of a gradient field in z-direction yields a z-dependent Larmor frequency, wherefore the BW of the pulse is imprinted on this direction, allowing excitation of an arbitrary slice thickness by changing the BW or the gradient amplitude. The sharpness of the slice is determined by the bandwidth-time-product (BWT), which corresponds to the total number of zero crossings of the RF pulse. However, with increasing BWT also the peak amplitude of the pulse increases, resulting in a higher SAR demand and consequently a compromise between SAR and slice sharpness has to be made. The use of a sinc pulse comes at the expense of prolonged echo times (TEs) compared to rect pulses, since a rewinder gradient has to be applied after the slice selection gradient. The 0^{th} gradient moment (i.e. the integral) of the rewinder is commonly equal to half the moment of the slice selection gradient to allow refocusing of the magnetization after excitation. While this poses no problem in conventional ^{1}H imaging, the short relaxation times of ^{23}Na can result in significant signal decay during the rewinding. Moreover, the SAR of a sinc pulse is high compared to the SAR of a rect pulse with similar FA and pulse duration, since $SAR \propto |B_1|$. Further, the SAR increases with the BWT, which becomes apparent when considering the maximal pulse amplitudes in figure 2. To tackle this issue, techniques such as a VERSE routine are applied, as illustrated in the following.

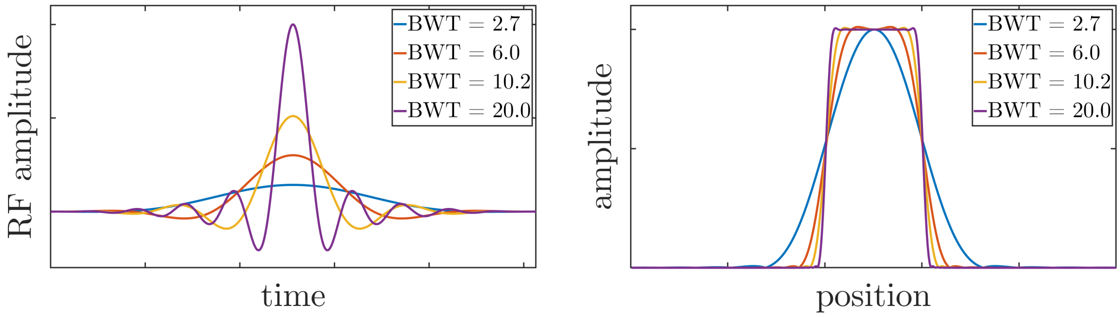

Figure 2: Three sinc pulses (left) with $BWT = [2.7, 6.0, 10.2, 20.0]$ and the corresponding slice profiles (right) in the small tip angle approximation are shown. Mind that the maximal pulse amplitude increases with the BWT and consequently a sharper slice profile results in a higher SAR demand.

2.5.1.3 Variable-Rate Selective Excitation

Variable-rate selective excitation (VERSE) is a technique to reduce the SAR of RF pulses [24], where both an existing RF pulse and the corresponding slice selection gradient are modified to yield an unchanged excitation profile. Neglecting relaxation effects, the FA for a constant excitation pulse with duration Δt is given by

$$\alpha = \gamma B_1 \Delta t. \tag{2.80}$$

It is therefore obvious that an increase of Δt can compensate any decrease of the excitation field B_1. In the following we consider an RF pulse $B_1(n) = B_{1r}(n) + iB_{1i}(n)$ with N discrete samples of duration Δt and the slice direction gradient G is chosen in z-direction. Applying the pulse on the magnetization can therefore be expressed as the matrix product

$$\vec{M}(z, N\Delta t) = \Pi_{n=N}^{1} exp \left(\begin{pmatrix} 0 & Gz & -B_{1i}(n) \\ -Gz & 0 & B_{1r}(n) \\ B_{1i}(n) & -B_{1r}(n) & 0 \end{pmatrix} \gamma \Delta t \right) \vec{M}(z, 0). \tag{2.81}$$

Multiplication of $1 = \frac{\beta}{\beta}$ changes the n^{th} rotation matrix to

$$\exp \left(\begin{pmatrix} 0 & \beta(n)Gz & -\beta(n)B_{1r}(n) \\ -\beta(n)Gz & 0 & \beta(n)B_{1i}(n) \\ \beta(n)B_{1r}(n) & -\beta(n)B_{1i}(n) & 0 \end{pmatrix} \frac{\gamma \Delta t}{\beta(n)} \right). \tag{2.82}$$

Therefore, the n^{th} RF entry can be modified when the corresponding gradient entry is modified as well. This yields the VERSE-conditions

$$\begin{pmatrix} B_{1r}(n) \\ B_{1i}(n) \\ G \end{pmatrix} \Delta t = \begin{pmatrix} \beta(n)B_{1r}(n) \\ \beta(n)B_{1i}(n) \\ \beta(n)G \end{pmatrix} \frac{\Delta t}{\beta(n)} = \begin{pmatrix} b_{1r}(n) \\ b_{1i}(n) \\ g(n) \end{pmatrix} t(n) \tag{2.83}$$

and the FA is unchanged if the temporal integral of the RF pulse and the gradient are constant.

Since the SAR is described by

$$SAR \propto \sum_{n=1}^{N} |B_1(n)|^2 \Delta t, \tag{2.84}$$

reducing pulse areas with high amplitude while increasing the parts with low amplitude can yield a new RF pulse with reduced SAR without changing neither the duration nor the excitation profile. An exemplary VERSE pulse and its initial sinc pulse ($BWT = 10.2$) are shown in figure 3. The SAR of the VERSE pulse is reduced by 36 % compared to the initial pulse, without alteration of the slice profile.

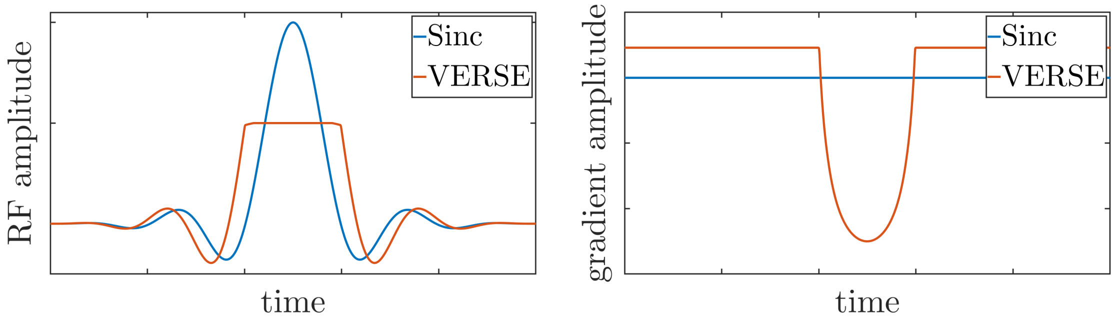

Figure 3: An examplary VERSE pulse is shown, created by constraining the amplitude to be below half the maximal amplitude of the initial sinc pulse ($BWT = 10.2$). This results in a SAR reduction of 36 %, without alteration of the excitation profile.

2.5.2 Spatial encoding

After excitation, the spatial information has to be encoded, which is based on linear gradient fields $\vec{G}(t)$, whose application results in a spatially dependent Larmor frequency:

$$\omega_0(\vec{r}, t) = \gamma \left(B_0 + \vec{r}\vec{G}(t) \right) . \tag{2.85}$$

An object with non-interacting transverse magnetization is assumed in the following in the rotating frame. Application of a temporally constant gradient field for the time t results in a position-dependent Larmor frequency as described in equation 2.85. After the gradient is switched off, all spins experience the same precession frequency again but the accumulated position-dependent phase ϕ remains:

$$\phi(\vec{r}, t) = -\gamma \int_0^t \vec{r}\vec{G}(t')\, \mathrm{d}t'. \tag{2.86}$$

The signal of the imaged object, described by the spatial magnetization distribution $M_\perp(\vec{r})$, is given by the spatial integral

$$s(t) = \int M_\perp(\vec{r}) e^{-i\phi(\vec{r},t)}\, \mathrm{d}\vec{r}, \tag{2.87}$$

which can be expressed as

$$s(\vec{k}) = \int M_{\perp}(\vec{r}) e^{-i2\pi\vec{k}\vec{r}} \, \mathrm{d}\vec{r}, \tag{2.88}$$

when the spatial frequency $\vec{k}$ is introduced.

$$\vec{k} = \frac{\gamma}{2\pi} \int_0^t \vec{G}(t') \, \mathrm{d}t', \tag{2.89}$$

which spans the k-space.
Applying the inverse Fourier transform onto equation 2.88 yields the spatial magnetization distribution

$$M_{\perp}(\vec{r}) = \int s(\vec{k}) e^{i2\pi\vec{k}\vec{r}} \, \mathrm{d}\vec{k}, \tag{2.90}$$

if $s(\vec{k})$ is known.
In practice, only discrete values of $\vec{k}$ will be known and the Fourier transform is replaced by a discrete FT (DFT), commonly implemented as a fast FT (FFT). The conditions on the k-space sampling for artifact-free image reconstruction are discussed in the following section.
Note that $\vec{k}$ can be changed by varying either t or $\vec{G}$. Changing t while applying a gradient is performed during data acquisition and is termed frequency encoding. Changing $\vec{G}$, on the other hand, is called phase encoding and requires N measurement repetitions to sample N data points to allow a constant t.

2.5.3 Discrete k-space sampling

In theory, the gradients allow free movement through k-space and therefore any arbitrary sampling scheme can be used as long as the k-space is filled sufficiently. However, the maximal amplitudes and maximal slewrates of the gradient system limit the choice of the readout trajectory. Due to its efficiency, most MRI sequences apply a Cartesian readout. In 2D Cartesian sampling, one frequency encoding and one phase encoding direction are commonly used. In 3D MRI, the third direction is sampled with an additional phase encoding. The Nyquist-Shannon theorem implies the maximal required k-value as well as the minimal distance between sampling points in k-space for a given resolution $(\Delta x, \Delta y, \Delta z)$ and field of view (FOV):

$$\Delta\vec{k} = \left(\frac{1}{FOV_x}, \frac{1}{FOV_y}, \frac{1}{FOV_z} \right)^T, \tag{2.91}$$

$$\vec{k}_{max} = \frac{1}{2}\left(\frac{1}{\Delta x}, \frac{1}{\Delta y}, \frac{1}{\Delta z}\right)^T. \tag{2.92}$$

Equation 2.91 directly implies that a larger FOV, which corresponds to the excited area, results in the need of a higher sampling density in k-space and therefore prolonged scan times. Consequently, MRI scans are commonly performed such that only the areas of interest are excited, often via slice selection, to reduce the measurement duration. The effect of different $\vec{k}_{max}$ on the reconstructed image is visualized in figure 4, where different areas of k-space were cropped. It becomes apparent that the k-space center represents the contrast and low resolution image features, whereas the k-space periphery represents the fine image structures.

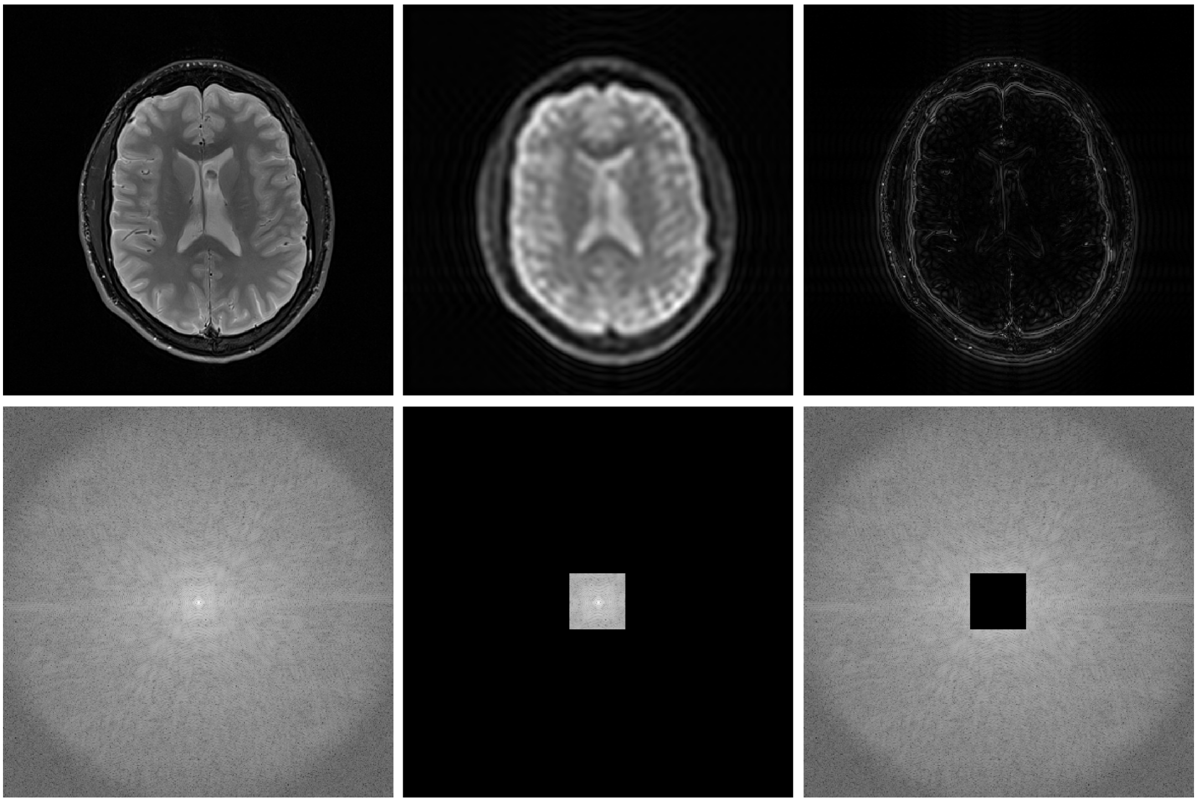

Figure 4: Different k-space coverage (shown on a logarithmic scale) and the corresponding reconstructed images are shown. Cropping of the peripheral k-space areas results in loss of fine image structures, whereas cropping of the k-space center removes the contrast and low resolution structures.

2.5.4 Radial sampling

The previously described Cartesian sampling is the most common k-space trajectory due to a variety of reasons, such as efficiency and robustness against system imperfections. However, other sampling strategies such as radial or spiral readouts are used as well. In this work, center-out radial trajectories are used for 2D as well as 3D imaging as illustrated in figure 5.

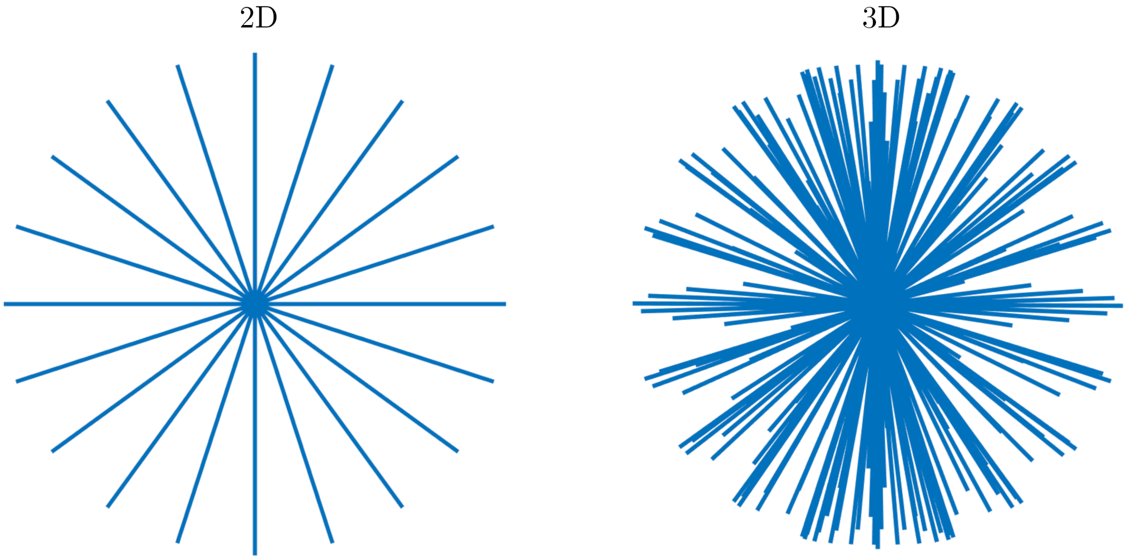

Figure 5: Schematic drawings of a 2D and a 3D radial readout trajectory are shown, where the readout direction is determined by the applied gradient.

The use of radial sequences allows short TEs since no phase encoding gradient has to be applied prior to the data acquisition. For selective sequences, such as a 2D radial sequence, therefore the rewinder gradient determines the minimal delay between excitation and readout. The 3D radial sequence conventionally exploits a non-selective excitation pulse and consequently the readout can be performed directly after the excitation pulse. This is especially useful for ^{23}Na imaging, where short relaxation times yield a rapid signal decay.

Other advantages of radial imaging are the motion-robustness and the possibility to undersample the k-space while preserving most of the image quality. Here, undersampling refers to acquisition of less spokes than required to fulfill the Nyquist criterion. For a

2D readout, the Nyquist criterion yields the minimal number of projections

$$N_{Pmin} = \pi \frac{FOV}{\Delta x}, \tag{2.93}$$

where Δx corresponds to the in-plane resolution.
In the 3D case, the Nyquist creterion is given by

$$N_{Pmin} = \pi \left(\frac{FOV}{\Delta x} \right)^2 . \tag{2.94}$$

The undersampling factor (USF) is defined by

$$USF = \frac{N_{Pmin}}{N_P}, \tag{2.95}$$

where N_P is the number of projections acquired in a measurement.
Figure 6 shows examples of different undersampling factors for both a 2D and a 3D radial sequence.

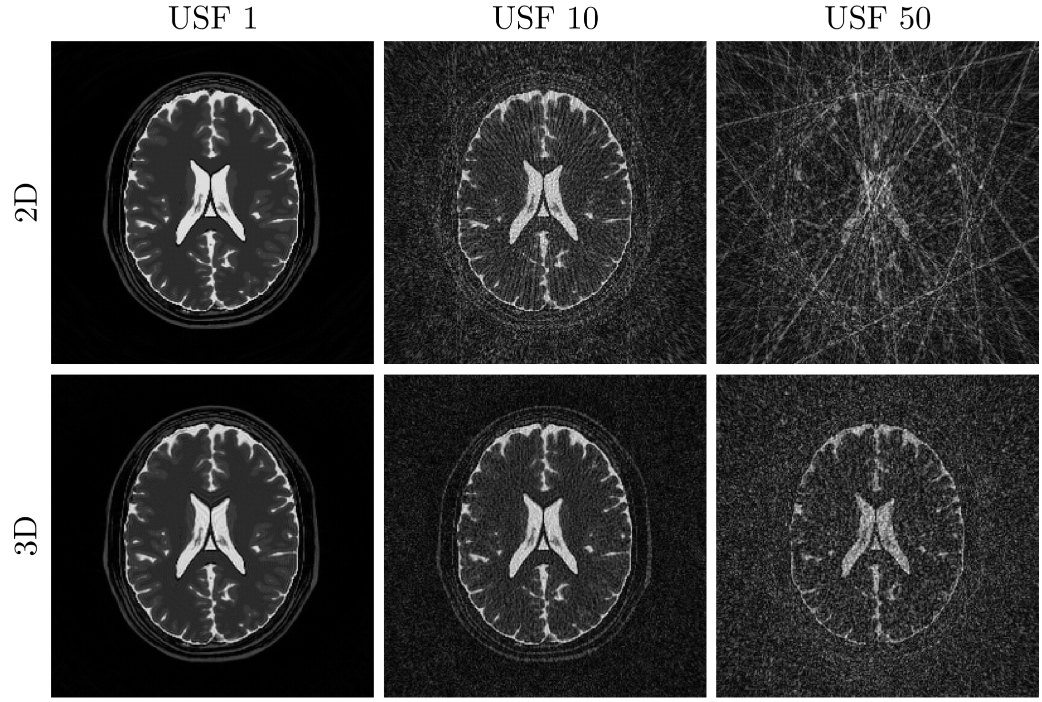

Figure 6: Image reconstructions of a numerical head model with different undersampling factors ($USF = [1,\ 10,\ 50]$) are shown for both 2D and 3D radial imaging as illustrated in figure 5. Streaking artifacts are visible in the undersampled 2D acquisitions, whereas the artifacts in the 3D images appear noise-like.

2.5.4.1 Density adapted radial sampling

Conventional radial sampling is achieved with a constant readout gradient, wherefore the distance Δk between samples on each spoke is constant along the readout direction. Due to the radial geometry, however, the distance between spokes increases with the distance to the k-space center, resulting in a decreasing k-space sampling density as illustrated in figure 7. Since a more homogeneous k-space sampling increases the SNR, density adapted (DA) readout gradients were introduced for both 2D and 3D radial trajectories [25, 26]. They are designed to counteract the increasing distance between spokes by reducing Δk along the readout via variation of the gradient amplitude, as illustrated in figure 7. The DA readout gradients consist of a ramp regiment, a trapezoidal part, a density adapted part and a ramp down regiment. The maximal gradient amplitude is described by G_0 and t_0 corresponds to the combined duration of the ramp and the trapezoidal part. The readout duration T_{RO} is defined as the gradient duration without the ramp down area. The construction of the density adapted parts is illustrated in the following.

In the 2D case, the sampling density distribution in k-space in radial direction is given by

$$D_{2D}(k) \propto \frac{1}{2\pi k G(k)}. \tag{2.96}$$

In practice, both the gradient amplitude and gradient slewrate are restricted due to hardware and safety concerns. Consequently, the gradient starts with a linear ramp and a flat top part with amplitude G_0, resulting in the k-value after the time t_0:

$$k_0 = k(t_0) = \frac{\gamma}{2\pi} \int_0^{t_0} G(t)\,\mathrm{d}t. \tag{2.97}$$

Hence, equation 2.96 and k_0 yield the density adapted gradient for $t > t_0$:

$$\begin{aligned} G_{2D,DA}(t) &= \frac{\mathrm{d}}{\mathrm{d}t} \frac{2\pi k(t)}{\gamma} \\ &= \frac{\mathrm{d}}{\mathrm{d}t} \frac{2\pi \left(\sqrt{k_0^2 + \frac{\gamma}{2\pi} 2 k_0 G_0 (t - t_0)} \right)}{\gamma} \\ &= \frac{k_0 G_0}{\sqrt{k_0^2 + \frac{\gamma}{2\pi} 2 k_0 G_0 (t - t_0)}}. \end{aligned} \tag{2.98}$$

For the 3D case

$$D_{3D}(k) \propto \frac{1}{4\pi k^2 G(k)} \tag{2.99}$$

is valid, resulting in

$$G_{3D,DA}(t) = \frac{k_0^2 G_0}{\left(\gamma k_0^2 G_0 (t - t_0) + k_0^3\right)^{\frac{2}{3}}}. \tag{2.100}$$

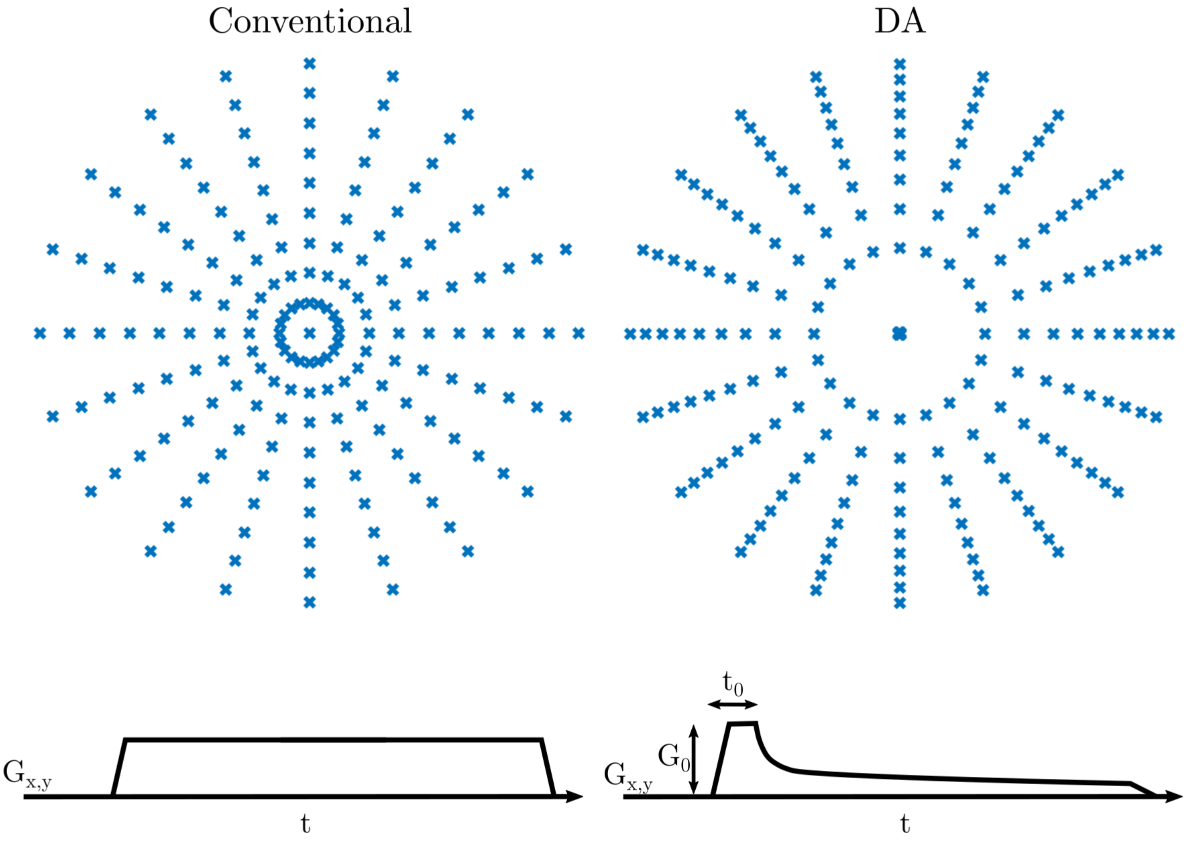

Figure 7: On the left hand side, a conventional radial sampling scheme and the corresponding trapezoidal readout gradient are shown, illustrating the decreasing sampling density in k-space. To counteract this effect, density adapted readout gradients, illustrated on the right hand side, can be used. Here the gradient amplitude is reduced during the readout and therefore the speed through k-space is changed, resulting in decreasing distance between samples along the readout if a fixed dwelltime is assumed. Note that the same principle can be expanded to 3D imaging.

2.6 Magnetic resonance fingerprinting

Magnetic resonance fingerprinting [10] is a technique for rapid and simultaneous quantification of various parameters. This is achieved by acquisition of a spatially highly undersampled time series of a sequence-driven transient state signal. The most common aim is to simultaneously quantify both longitudinal and transverse relaxation times. However, other parameters such as diffusion [27], velocity [11] and chemical exchange [12] were quantified using MRF as well. A combination of ^{1}H MRF and ^{23}Na TSC imaging was proposed by Yu et al. [13]. In X-nuclei MR, to the best of the authors knowledge, MRF was only exploited in ^{31}P magnetic resonance spectroscopy (MRS) for quantification of the creatine kinase reaction rate [15] and in determination of the ^{23}Na signal contribution of different compartments [14]. In this work the potential of MRF to quantify ^{23}Na relaxation times is investigated.

In the following a brief overview on the basics of MRF is given. A more detailed description can be found in [28, 29, 30].

2.6.1 Transient signal evolution

Most MRI sequences use a steady state signal for imaging. The exact steady state in these sequences is given by a multitude of parameters such as FA, TE, TR and the off-resonance. Consequently, changing these parameters leads to a change of the state and therefore variation of the signal. Hence, a transient signal can be constructed by constantly changing the imaging parameters. The exact evolution of this transient state signal depends on the tissue parameters, which is exploited in MRF to characterize them. The most significant impact on the signal state for relaxometric quantification is generated by the FA, TE and repetition time (TR).

To give a comprehensive example, the simulated signal evolution of brain tissue (BT; $T_1 = 40\,\text{ms}$, $T_{2l} = 35\,\text{ms}$, $T_{2s} = 4.9\,\text{ms}$, $T_{2l}^{*} = 30\,\text{ms}$, $T_{2s}^{*} = 4.8\,\text{ms}$) and cerebrospinal fluid (CSF; $T_1 = T_2 = 60\,\text{ms}$, $T_2^{*} = 50\,\text{ms}$) for a FISP sequence ($\text{TE} = 0.55\,\text{ms}$, $\text{TR} = 10\,\text{ms}$) with variable FA is shown in figure 8. These signal evolutions are well distinguishable due to the different relaxation times of the given tissues. In the following, we assume imaging a subject that solely consists of the two compartments BT and CSF. Consequently, when an image is acquired for each signal state, the signal evolution in each voxel can be determined and therefore each voxel can be assigned to one of the tissue types.

This approach can be expanded to a large number of parameter combinations, allowing reconstruction of the parameters in each voxel. Relaxometric mapping with MRF is

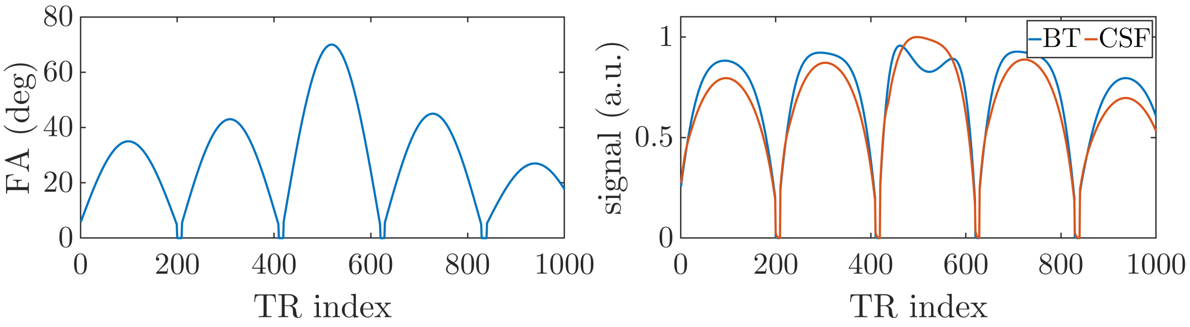

Figure 8: The FA pattern proposed by Jiang et al. [31] without prior inversion pulse (left) was implemented in an ISTO simulation (see section 3.4.2) of FISP sequence (TE = 0.55 ms, TR = 10 ms). The resulting signal evolutions for brain tissue (BT, $T_1 = 40\,\text{ms}$, $T_{2l} = 35\,\text{ms}$, $T_{2s} = 4.9\,\text{ms}$, $T_{2l}^* = 30\,\text{ms}$, $T_{2s}^* = 4.8\,\text{ms}$) and cerebrospinal fluid (CSF, $T_1 = T_2 = 60\,\text{ms}$, $T_2^* = 50\,\text{ms}$) show good distinguishability, which yields the basis for MRF.

based on the signal dynamics and is independent of the signal amplitude, assuming sufficient SNR. Hence, inhomogeneous density distributions and receive sensitivities do not alter the relaxometric mapping.

2.6.2 Undersampled image acquisition

As mentioned before, the signal evolution in each voxel can be used for reconstruction of the parameter maps, when an image is acquired for each signal state. However, this would lead to long acquisition times. Therefore, a key feature of MRF is the high spatial undersampling of each time frame to reduce scan times. When different k-space trajectories are sampled in each time frame, the overall measurement still contains the full spatial information required to reconstruct an artifact free image, as illustrated in section 3.5, figure 21. In practice, most MRF sequences exploit a radial or spiral readout since their streak-like or noise-like undersampling artifacts can be well suppressed.

2.6.3 Simulation based reconstruction

A disadvantage of the transient state is that there is generally no analytic solution describing the signal evolution. This issue, however, can be tackled by conducting simulations with a suitable signal model. Commonly, a discrete range is set for each parameter that is to be quantified and all parameter combinations are stored in a lookup table (LUT). Subsequently, the theoretical signal evolution is computed for all entries in the

LUT and stored in a dictionary $\delta \in \mathbb{C}^{M \times T}$, where T is the number of signal observations and M the number of unique parameter combinations. The following description is based on work by Assländer et al. [32].

Mathematically, the measurement process with an arbitrary k-space trajectory can be described by

$$S = GFx, \tag{2.101}$$

where $x \in \mathbb{C}^{NT}$ corresponds to the image time series with N voxels and T time frames. The measured signal is denoted by $S \in \mathbb{C}^{KT}$, where K is the trajectory length in each time frame in k-space. $F \in \mathbb{C}^{NT \times NT}$ corresponds to be a block-diagonal matrix which represents the Fourier transformation along all spatial dimensions for each time frame T. The gridding operator $G \in \mathbb{C}^{KT \times NT}$ grids the Cartesian k-space onto the arbitrary k-space trajectory.

Reconstruction of the parameters in each voxel can be achieved by finding the best matching dictionary entry (atom) to the signal evolution in the voxel and extracting its parameters. The dictionary entry matrix $D \in \mathbb{C}^{NT \times N}$ can be constructed by combining the best fitting atoms of all voxels

$$D = \begin{pmatrix} d_{1,1} & \cdots & 0 \\ \vdots & \ddots & \vdots \\ 0 & \cdots & d_{N,1} \\ \vdots & \vdots & \vdots \\ d_{1,T} & \cdots & 0 \\ \vdots & \ddots & \vdots \\ 0 & \cdots & d_{N,T} \end{pmatrix}. \tag{2.102}$$

Therefore, $DD^{\dagger}x$ is the time series of images, composed of dictionary atoms to match x. Consequently, the forward model described by the dictionary is given by

$$S = GFDD^{\dagger}x \tag{2.103}$$

and the general MRF reconstruction problem can be expressed by

$$\min_{D,x} = \| GFDD^{\dagger}x - S \|_2^2, \tag{2.104}$$

where the reconstructed images x and the best fitting dictionary entries D are unknown.

To decrease memory consumption and to denoise the reconstructed images [33, 32], the dictionary can be compressed. A common compression approach is to calculate a singular value decomposition (SVD) which yields a new basis, sorted by the energy of the individual basis functions.
The dictionary $\delta \in \mathbb{C}^{M\times T}$ can be expressed using the SVD [32, 33]:

$$\delta = u\Sigma v^{\dagger}, \tag{2.105}$$

where $v \in \mathbb{C}^{T\times T}$ and $u \in \mathbb{C}^{M\times M}$ are unitary matrices. The diagonal matrix $\Sigma \in \mathbb{R}^{M\times T}$ contains decreasing singular values in decreasing order. A rank-k approximation of the dictionary in the new space is given by

$$\tilde{\delta} = u_k^{\dagger}\delta, \tag{2.106}$$

where u_k corresponds to the first k columns of the unitary matrix.
Defining

$$U_k = \begin{pmatrix} u_{1,1}\mathbb{1} & \cdots & u_{1,k}\mathbb{1} \\ \vdots & \ddots & \vdots \\ u_{T,1}\mathbb{1} & \cdots & u_{T,k}\mathbb{1} \end{pmatrix}, \tag{2.107}$$

with $u_{t,k} \in \mathbb{C}$ being the entries of the first k columns of u and $\mathbb{1}$ the identity matrix of rank N, allows a low rank approximation of x:

$$\tilde{x} = U_k^{\dagger}x. \tag{2.108}$$

Consequently, the compressed image series $\tilde{x} \in \mathbb{C}^{Nk}$ and the compressed dictionary matrix $\tilde{D} = (U_k^{\dagger}D)$ change equation 2.104 to

$$\min_{\tilde{D},\tilde{x}} = \| GFU_k\tilde{D}\tilde{D}^{\dagger}\tilde{x} - S \|_2^2 . \tag{2.109}$$

Hence, minimization of equation 2.109 yields the optimized time series $\tilde{x}$ and the best fitting dictionary entries with respect to the $\mathcal{L}_2$-norm, allowing the extraction of the parameter combination in each voxel.

2.7 Particularities of ^{23}Na MRI

In the following, practical considerations on sodium imaging are described. A more detailed description can be found in [34]. The main challenge in ^{23}Na MRI is the low SNR compared to ^{1}H. The amplitude of the NMR signal is given by

$$S \propto c\gamma^3 I(I+1), \tag{2.110}$$

which means that

$$S(^{23}\mathrm{Na}) = 0.093 S(^{1}\mathrm{H}) \tag{2.111}$$

for a similar concentration c. Considering the approximately 1000-fold lower ^{23}Na concentration with respect to ^{1}H, yields the signal ratio

$$\frac{S(^{23}\mathrm{Na})}{S(^{1}\mathrm{H})} \approx 10^{-4}. \tag{2.112}$$

Moreover, the gyromagnetic ratio $\gamma_{^{23}\mathrm{Na}}$ is about 3.8 times smaller than $\gamma_{^{1}\mathrm{H}}$, which leads to the 3.8-fold reduced Larmor frequency. Hence, assuming the thermal noise to be linearly dependent on the frequency [26], leads to

$$\frac{SNR(^{23}Na)}{SNR(^{1}H)} \approx 2.5 \cdot 10^{-3}. \tag{2.113}$$

Consequently, ^{23}Na imaging suffers from long scan durations and reduced resolution to achieve the required SNR. Further, the ^{23}Na relaxation times are short and typically in the order of $T_1 = 12\,\mathrm{ms}$–$65\,\mathrm{ms}$, $T_{2l}^{*} = 10\,\mathrm{ms}$–$65\,\mathrm{ms}$ and $T_{2s}^{*} = 0.5\,\mathrm{ms}$–$6.5\,\mathrm{ms}$ [4, 8, 34]. This motivates the use of UTE sequences for sodium imaging to minimize the signal decay between excitation and data acquisition. Therefore, often sequences with non-selective excitation and center-out readout techniques such as radial trajectories or twisted projection imaging (TPI) are used. The exhaustive use of non-selective excitation is a major difference to ^{1}H MRI, where commonly selective excitation pulses are used since here the time for acquisition of the entire k-space is often larger than the time required to collect sufficient SNR. In ^{23}Na MRI however, the bottleneck is the SNR and acquisition of a larger k-space is therefore rarely of concern. The reduced gyromagnetic ratio of ^{23}Na with respect to ^{1}H allows construction of coils, producing a more homogeneous excitation field, which is a big issue in ^{1}H MRI at 7 T. Further, the reduced gyromagnetic ratio makes ^{23}Na MRI less sensitive to off-resonances with respect to ^{1}H since $\omega_{off} = \gamma \Delta B_0$, which simultaneously comes at the expense of an increased gradient amplitude to reach a certain k-value in k-space. However, in practice this is rarely of concern as the maximal k-values are commonly smaller in ^{23}Na imaging due to the increased voxel size, as explained in section 2.5.

2.8 Sodium ions in the human body

Sodium ions play an important role in many physiological processes in the human body. The basics of the ^{23}Na-^{39}K-pump and the distribution of sodium in the human head are discussed briefly in the following. A more detailed description of ^{23}Na physiology can be found in standard literature [34, 35].

In a healthy cell, the ^{23}Na concentration is in the order of $\left[Na^{+}\right]_{i} = 5\,\text{mmol/L–}15\,\text{mmol/L}$, whereas a concentration of $\left[Na^{+}\right]_{e} = 140\,\text{mmol/L–}150\,\text{mmol/L}$ is found in the extracellular space [35]. The ^{39}K gradient is orientated in the opposite direction, where concentrations of $\left[K^{+}\right]_{i} = 120\,\text{mmol/L–}150\,\text{mmol/L}$ and $\left[Na^{+}\right]_{e} = 4\,\text{mmol/L–}5\,\text{mmol/L}$ are present. Those gradients are predominantly maintained by an enzyme in the cell membrane, called the ^{23}Na-^{39}K-pump (^{23}Na^{+}-^{39}K^{+}-ATPase), illustrated in figure 9. The latter extrudes three sodium ions and imports two potassium ions into the cell using the energy obtained by transformation of adenosine triphosphate (ATP) to adenosine diphosphate (ADP).

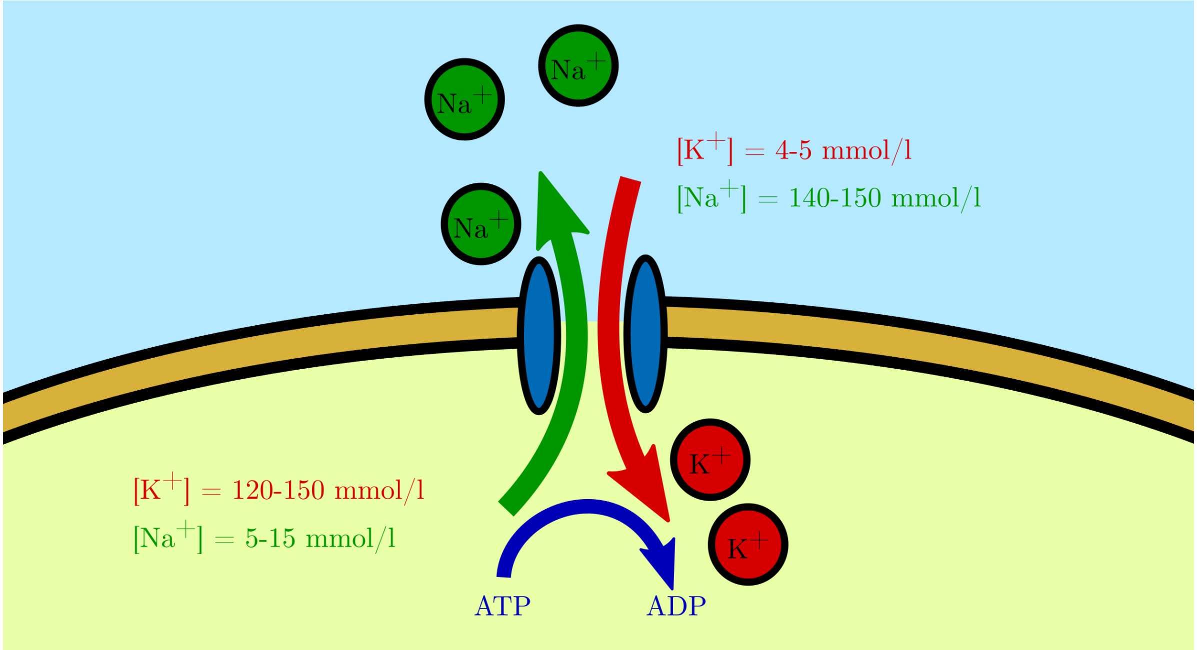

Figure 9: Illustration of the ^{23}Na^{+}-^{39}K^{+}-ATPase. Here, three ^{23}Na ions are extruded from the cell, while two ^{39}K ions are imported under transformation of ATP to ADP.

This, in conjunction with other ion channels in the cell membrane, leads to an approximate cell potential of $-70\,\text{mV}$. The latter plays an important role in both the central

nervous system and muscular system. An incoming stimulus, which corresponds to a voltage, depolarizes the cell by opening sodium channels and therefore allowing inflow of ^{23}Na ions into the cell. The subsequent repolarization is achieved by closing the ^{23}Na channels and opening other ion channels (K^+, Cl^-, Ca^{2+}). This is driven forward along the nerve fiber and therefore transmits the stimulus, where the dead time of the cell leads to propagation of the stimulus in only one fiber direction.
A potential application of ^{23}Na MRI is investigation of the sodium concentration in the muscle, which can be changed due to malfunction of the $^{39}K^+$-ATPase [5].
In the human head, ^{23}Na concentrations of 20 mmol/L–60 mmol/L in white matter (WM), 30 mmol/L–70 mmol/L in gray matter (GM) and 140 mmol/L–150 mmol/L in CSF were measured [34]. In malignant brain tumors, on the other hand, an increased cell division rate was found, preceded by a depolarization of the cell, resulting in an increased ^{23}Na concentration in the cell. This, in conjunction with a changed ratio of intra- and extracellular volume, results in a higher sodium concentration in most brain tumors compared to healthy tissue, enabling examination of brain cancer and monitoring the course of therapy with ^{23}Na MRI. Moreover, other applications of ^{23}Na MRI in the human head are the investigation of strokes, multiple sclerosis, Alzheimer's disease and Huntington's disease [34].

3 Methods

3.1 Hardware

All measurements were conducted on a whole body research system (Siemens Healthcare, Erlangen, Germany) with a static field strength of 6.98 T, located at the German Cancer Research Center (DKFZ) in Heidelberg, Germany. The scanner is equipped with an AS095DS gradient coil, producing a maximal magnetic gradient of 38 mT/m and achieves a maximal slewrate of 200 mT/m ms.

Figure 10: Photograph of the 7T whole body MR system, located at the German Cancer Research Center (DKFZ) in Heidelberg, Germany.

3.1.1 RF coils

Two RF coils were used in this work, illustrated in figure 11. The first coil is a ^{23}Na birdcage RF coil (Rapid Biomed GmbH, Rimpar, Germany), equipped with an additional ^{1}H channel. This coil was the workhorse of this project, as it provides sufficient homogeneity but has only one receive channel, which decreases the computational burden in the image reconstruction and consequently increases reconstruction speed, which was especially beneficial in the development process. The second RF coil used is a double-resonant ^{1}H/^{23}Na head coil with 30 sodium receive channels (Rapid Biomed GmbH, Rimpar, Germany), which was used in the 2D in vivo experiments.

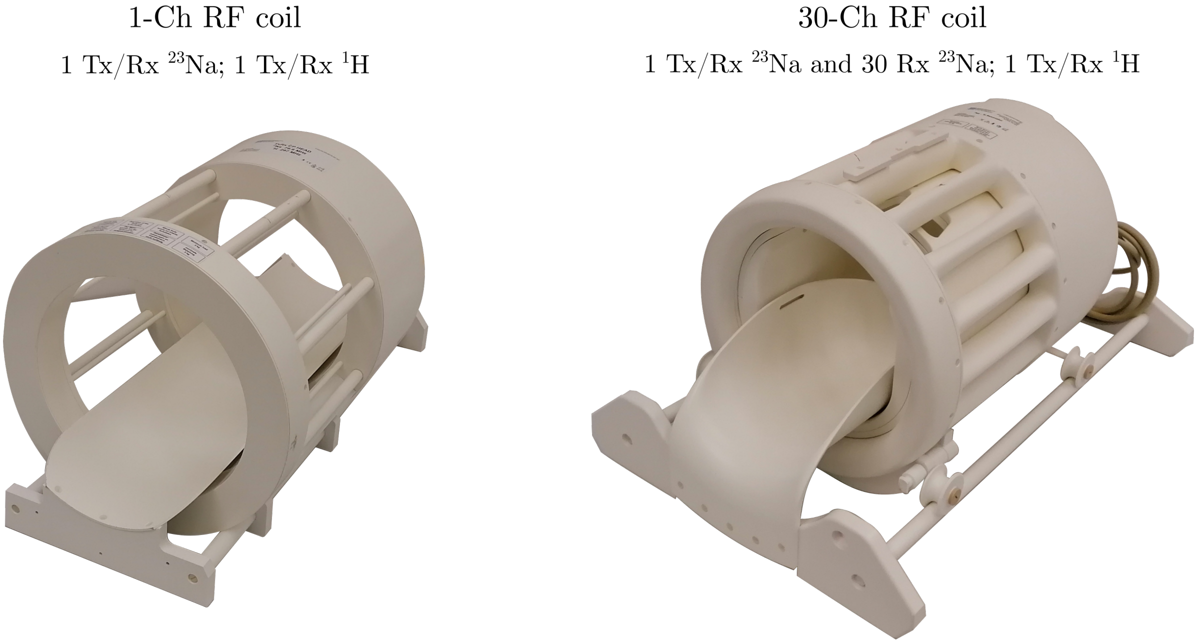
1-Ch RF coil

1 Tx/Rx ^{23}Na; 1 Tx/Rx ^{1}H

30-Ch RF coil

1 Tx/Rx ^{23}Na and 30 Rx ^{23}Na; 1 Tx/Rx ^{1}H

Figure 11: Photograph of the RF coils used in this work. Left, the ^{23}Na birdcage coil, equipped with an additional ^{1}H channel, is shown. On the right, the ^{23}Na RF coil with 30 receive channels and additional ^{1}H module is displayed.

3.1.2 Phantoms

Two similar phantoms were used in this work, which are shown in figure 12. The first phantom is cylindrically shaped with a diameter of 190 mm and a length of 160 mm. It is filled with aqueous 0.9 % NaCl solution (compartment 0) and seven smaller vials (compartments 1-7) with a diameter of 43 mm are inserted, which contain aqueous 0.9 % NaCl solution and additional Agar concentrations ranging from 1 % to 7 % to cover a range of relaxation times. This phantom was used for the 2D experiments. However, the latter is approximately 2 mm to wide to fit into the 30-Ch coil. A second phantom version was designed and manufactured at the house-internal workshop for the 3D experiments. Here, the outer diameter was reduced to 180 mm to fit the 30-ch coil. The length is 155 mm and the vials have an outer diameter of 50 mm. Further, compartment 1 was removed, as the 2D experiments showed that 1 % Agar yields relaxation times which are not expected in vivo.

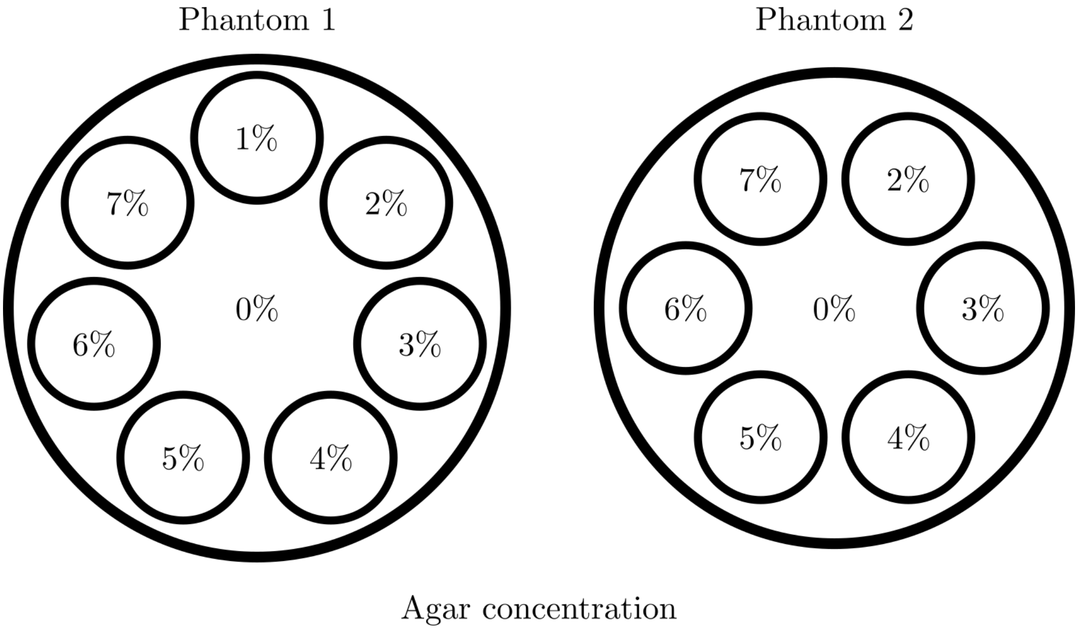

Figure 12: The phantoms used in this work are displayed. On the left, phantom 1 is shown, which is filled with a sodium concentration of 0.9 %. The vials contain an additional Agar concentration of [1, 2, 3, 4, 5, 6, 7] %. Phantom 2, illustrated on the right, contains similar ^{23}Na and Agar concentrations, but the vial with additional 1 % Agar was abandoned. The line widths are adjusted to represent the thickness of the acrylic glass. Image adapted from [36].

3.2 Reference pulse sequences and image reconstruction

In this work, well established ^{23}Na MR sequences were used to acquire relaxometric reference maps as well as the ΔB_0 and B_1 distributions. The sequence principles, the corresponding image reconstructions and the model fitting are discussed in the following. Note that the MRF sequences, developed in this work, are explained in section 3.3.
Since the reference sequences for 2D and 3D experiments are similar, they will be illustrated jointly. Note that in the following excitation pulses are only characterized by their nominal FA. If not stated differently, slice-selective sinc pulses are applied in 2D imaging, whereas non-selective rect pulses are used for 3D measurements. Further, the term DA gradients refers to either the 2D or the 3D implementation, depending on the sequence type. All ^{23}Na sequences, except for the transmitter voltage adjustment, use center-out DA readout gradients.

3.2.1 ^{23}Na image reconstruction

All following ^{23}Na measurements were reconstructed using an offline pipeline in MATLAB (The MathWorks, Natick, MA, USA), which recovers all sequence parameters from the measurement header and uses NUFFT operators for reconstruction [37]. A density compensation was performed on the data to counteract non-homogeneous sampling density. Furthermore, the framework allows application of filters to increase the SNR and reduce Gibbs ringing artifacts at the expense of a broadened point spread function (PSF). The three most common filters are the Hamming, the Hanning and the Gaussian filter, which are given by:

- Hamming:
$$w(k) = \frac{25}{46} + (1 - \frac{25}{46}) \cos\left(\frac{\pi k}{k_{max}}\right) \tag{3.1}$$
- Hanning:
$$w(k) = \frac{1}{2}\left(1 - \cos\left(\frac{\pi k}{k_{max}}\right)\right) \tag{3.2}$$
- Gaussian:
$$w(k) = e^{-2(\pi k \sigma)^2} \tag{3.3}$$

Here, σ can be varied to adjust the amount of filtering.

3.2.2 Determination of the ^{23}Na reference voltage

At the beginning of each measurement session, the ^{23}Na reference voltage was determined by fitting a sine function to the data of 32 non-selective excitation pulses with increasing pulse voltage. To allow full recovery towards thermal equilibrium a repetition time of 550 ms was used.

3.2.3 Relaxometric mapping

To characterize the abilities of the MRF sequences developed in this work, the resulting MRF parameter maps were compared to those obtained with gold standard techniques, which are explained in the following. Note that this section explains the basics of the techniques used, whereas the sequence parameters used in the measurements are summarized in section 3.7.

3.2.3.1 Mapping of longitudinal relaxation times

Mapping of the longitudinal relaxation times was performed using an inversion recovery sequence. It begins with a non-selective excitation pulse in both the 2D and the 3D sequence version. Next, a variable inversion time (TI) is inserted, allowing longitudinal relaxation towards thermal equilibrium. Subsequently, an excitation pulse is applied to convert longitudinal into measurable transverse magnetization. Finally, spatial encoding is performed using a DA readout gradient, followed by a long pause (approximately $5T_1 \approx 300\,\text{ms}$ for ^{23}Na solution) to allow full magnetization recovery towards thermal equilibrium before the next excitation. In the measurements, variation of TI permitted sampling of the relaxation curve and a monoexponential relaxation model was fitted pixelwise to the data after image reconstruction using a least squares fitting routine in MATLAB:

$$S(TI) = \left| S_0 \left(1 - 2e^{-\frac{TI}{T_1}}\right) + N \right| . \tag{3.4}$$

Here, S_0 denotes the amplitude at $TI = 0\,\text{ms}$ and N the noise floor.
A schematic sequence diagram for the 3D version is shown in figure 13.

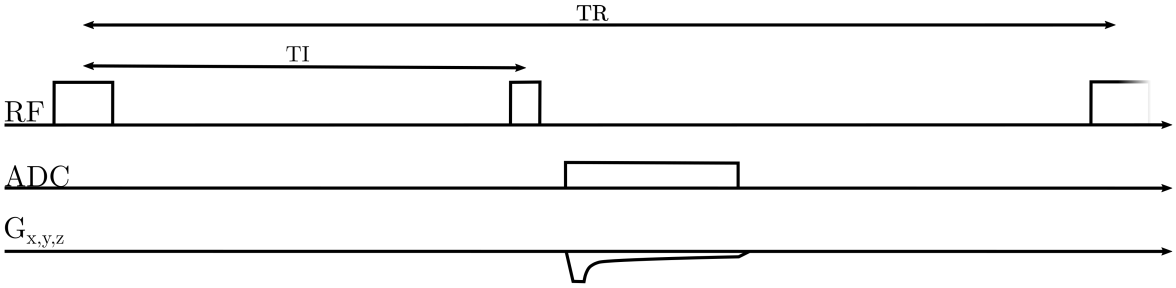

Figure 13: T_1 mapping was performed by fitting a monoexponential relaxation model to the data of an inversion recovery sequence. Sequence timings are not to scale.

3.2.3.2 Mapping of apparent transverse relaxation times

The transverse relaxation times were mapped with two different sequences but similar data post processing was performed. For the 2D measurements, a gradient echo (GRE) sequence was applied, where a single echo is acquired after excitation and echo time TE. A long TR, in the order of 200 ms, allows recovery to thermal equilibrium before the next excitation. The relaxation curve was sampled by variation of TE and a biexponential relaxation model was fitted pixelwise to the time series in image space:

$$S(TE) = \left| S_0 \left(0.6 e^{-\frac{TE}{T_{2s}^*}} + 0.4 e^{-\frac{TE}{T_{2l}^*}} \right) + N \right| . \tag{3.5}$$

Here, a fixed ratio of 0.6/0.4 for the short/long relaxation contribution was assumed, based on the theoretical relaxation theory for a single tissue compartment. This allowed comparison with the MRF sequences, where the same ratio was implied in the dictionary simulations. The short relaxation time T_{2s}^* was restricted to a range between 1 ms and 20 ms, whereas T_{2l}^* was constrained to 10 ms–70 ms. Moreover, a monoexponential signal model was fitted to the data, where $T_2^* = T_{2s}^* = T_{2l}^*$ was used in equation 3.5. Each voxel was assigned to either bi- or monoexponential relaxation, based on the coefficient of determination (R^2) of the fits. In phantom measurements, the mean and standard deviation (SD) of the relaxation times in each compartment were calculated for comparison with the MRF results. Biexponential voxels were neglected from the analysis in predominantly monoexponential areas and vice versa.

The 3D reference measurements for determination of the transverse relaxation times were conducted with a multi-echo GRE. Here, a rewinder gradient is used to null the 0th moment of the readout gradient, followed by a second readout. This procedure is repeated seven times such that eight readouts are performed, resulting in eight samples along the TE direction per TR. A spoiler gradient is used to dephase remaining transverse magnetization and a long TR allows relaxation towards thermal equilibrium. Since the echo spacing between the readouts within each TR is constant, changing the first TE results in a shift of all eight echo times. This allows dense sampling of the relaxation curve by varying the TEs. Similar to the single-echo GRE measurements, both a bi- and a monoexponential model were fitted to the reconstructed data and the relaxation type was assigned to each pixel, based on R^2. A schematic sequence diagram of the 3D multi-echo GRE is shown in figure 14.

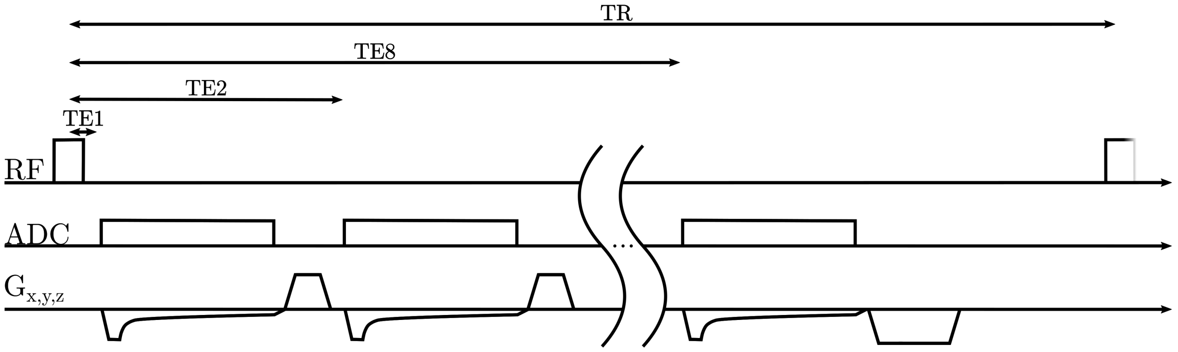

Figure 14: The multi-echo GRE sequence, used for 3D mapping of the transverse relaxation times, is shown. In the 2D experiments, a single-echo sequence with a similar sequence schematic, but acquiring only one readout per TR, was used. Sequence timings are not to scale.

3.2.4 B_0 mapping

Inhomogenieties in the static magnetic field result in position dependent off-resonances, which were mapped using the phase difference between two fast low-angle shot (FLASH) sequences with different TEs. Here, dephasing of the magnetization at the end of each TR is achieved by a spoiler gradient in readout direction and RF spoiling is used. The off-resonance distribution can then be calculated as

$$\Delta B_0 = \frac{\phi_2(\vec{r}) - \phi_1(\vec{r})}{TE_2 - TE_1} = \frac{\angle \left(\frac{im_2(\vec{r})}{im_1(\vec{r})} \right)}{2\pi \left(TE_2 - TE_1 \right)}, \tag{3.6}$$

where ϕ_1 and ϕ_2 are the position dependent phases and im_2 and im_1 correspond to the complex valued reconstructed images.

Mind that only off-resonances in the interval $(-\frac{1}{2(TE_2-TE_1)}, \frac{1}{2(TE_2-TE_1)})$ can be quantified due to the 2π periodicity of the signal phase.

3.2.5 B_1 mapping

Mapping of the excitation field was performed using the phase sensitive method [38, 39]. Here, an excitation pulse with $FA = 2\alpha$ is applied, immediately followed by an α-pulse with relative phase of 90° and subsequent readout. A second measurement is conducted, where the pulse phase of the first pulse is incremented by 180°. The phase difference between both acquisitions is free of phase offsets from eddy currents and other sources and the resulting phase is a monotonic function of the actual FA, which allows mapping of the excitation field [38].

3.2.6 ^{1}H imaging

Two ^{1}H sequences were used in this work. A localizer sequence, based on a FLASH sequence, was used to image the phantoms and for initial B_0 shimming.

In the 2D in vivo study, a turbo spin echo (TSE) image of each head was acquired for co-registration with the ^{23}Na images and subsequent defining of regions of interest (ROIs) in BT and CSF. A detailed description of ^{1}H sequences can be found in [17, 23].

3.3 MRF sequences

In this work three MRF sequences were developed, which are illustrated in the following. The first one is a 2D MRF sequence, developed to investigate the feasibility of MRF for ^{23}Na relaxometry [40].

When this was successful, a 3D version of the sequence was implemented to increase the covered volume per measurement time and the SNR efficiency. Furthermore, a simulation based on ISTOs was implemented to describe the full dynamics of spin 3/2 nuclei, as described in section 2.3. Finally, an optimized 3D MRF sequence, termed MRF II, was developed. Here, the readout efficiency was increased by implementing a hybrid of single- and a double-echo readouts. Moreover, the FA pattern was optimized using the CRLB [41, 42] to improve the T_1 encoding.

In all MRF sequences in this work, the transient signal is generated by varying FAs, TEs and TRs and their commonalities are illustrated in the following. The specifics of each sequence will be discussed below.

Each MRF measurement of this work can be divided into N_{PT} pulse trains (PTs), in which the same FA, TE and TR patterns are used to drive the magnetization in the same transient state conditions. To ensure that the magnetization is in thermal equilibrium at the beginning of each PT, consecutive PTs are separated by a pause of 1 s, allowing full relaxation of the magnetization between them.

Each PT consists of a succession of N_c cycles (equivalent to TR intervals), where each cycle uses a unique combination of FA, TE and TR. In this work, $N_c = 1000$ was chosen for all experiments. Since all acquisitions within one PT are acquired in different transient states, each readout is measured in a different time frame in k-space. Hence, for a single-echo sequence the number of time frames N_f is equal to the number of cycles N_c, whereas a double-echo sequence would yield $N_f = 2N_c$.

Since one pulse train results in acquisition of one spoke in N_f time frames in k-space, measurement of N_{PT} pulse trains results in $N_{PT} \times N_f$ k-spaces. However, the k-spaces of all PTs can be cyclewise combined because they are sampled in the same N_f transient states, resulting in N_f k-spaces containing N_{PT} spokes each. Hence, each time frame can be sampled homogeneously by incrementing the radial readout direction of each PT by $\frac{2\pi}{N_{PT}}$ for a 2D sequence and a similar approach for the 3D case, respectively. Furthermore, the spatial encoding is enabled by rotating the readout direction within each pulse train successively by the golden angle. This finally results in N_f rotated, homogeneously sampled time frames in k-space, as illustrated for the 3D case in section 3.3.2, figure 18.

Therefore, the entire MRF data set contains the full spatial information required for reconstruction of the images even if the individual time frames are highly undersampled. The varying FAs mainly enable encoding of the longitudinal relaxation, whereas the apparent transverse relaxation is predominantly determined by the varying TEs.

3.3.1 2D ^{23}Na MRF

The 2D ^{23}Na MRF sequence is based on a radial spoiled-steady-state free precession (SSFP/FISP) sequence [31] and a sequence diagram is shown in figure 16.
The FA and TE pattern, used in each PT, are illustrated in figure 15.

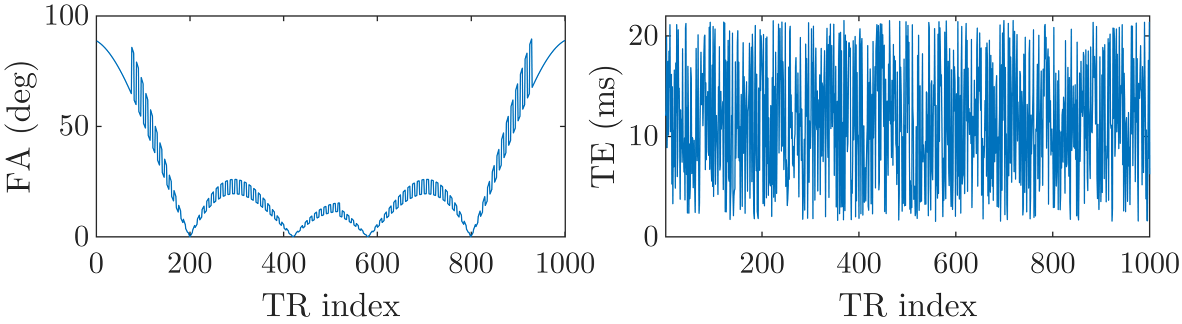

Figure 15: The FA pattern used in 2D MRF is shown on the left, whose heuristic construction is described in section 4.2.1.1. A pseudo-randomly chosen TE pattern was used, ranging from 1.55 ms to 21.55 ms and illustrated on the right. Image adapted from [40].

The FA pattern was constructed heuristically (see section 4.2.1.1) and consists of two half sinc functions, starting and ending with the maximal FA of 90°. Furthermore, step-like modulations toggle the pattern between the original value and the value scaled by 4/3 every five cycles. Entries that would exceed 90° were not scaled. The TE pattern was chosen pseudo-randomly, ranging from the minimal echo time $TE_{min} = 1.55\,\text{ms}$ to 21.55 ms, constituting a trade-off between sensitivity towards T_{2s}^* and T_{2l}^* as well as the scan efficiency. The short TE values are necessary to sample the short transverse relaxation time T_{2s}^*, whereas the long TE-delays mainly encode T_{2l}^* and T_2^*. Even longer TEs could further improve encoding of T_{2l}^* and T_2^* but would also linearly prolong the scan duration. As described above, consecutive time frames in k-space are successively rotated by the golden angle (111.2°) to enable spatial encoding.
Each cycle starts with a VERSE sinc pulse with a duration of 1024 µs, a BWT of 2.7 and a variable FA according to the FA pattern. Subsequent to the excitation pulse, a

rewinder gradient is inserted, whose length, in conjunction with half the pulse duration, determines the minimal echo time TE_{min}. Next, a variable TE-delay is applied and a DA readout gradient is used for data acquisition, followed by a rewinder gradient. Last, a spoiler gradient in slice direction is used to dephase the spins by 4π over the slice at the center of the next excitation pulse. Since the next cycle starts directly after the spoiler gradient, the varying TE results in the same variation in TR: $TR(i) = TR_0 + TE(i)$.

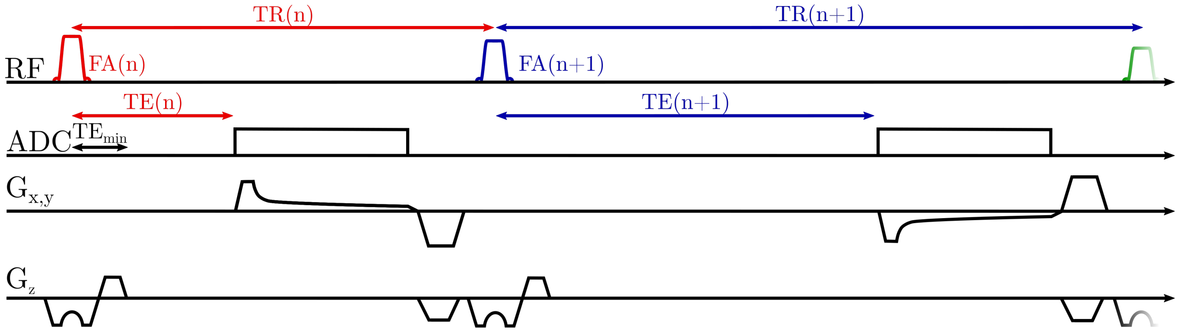

Figure 16: A schematic of the 2D MRF sequence is illustrated, timings are not for scale. A slice selective VERSE pulse is used for excitation, followed by a rewinder gradient and variable TE. Spatial encoding is conducted using density adapted readout gradients and a subsequent spoiler gradient is used to dephase the spins 4π in slice direction. Image adapted from [40].

The dictionary simulation for the 2D MRF sequence was based on adapted Bloch equations, as described in section 3.4.1.

3.3.2 3D ^{23}Na MRF I

The MRF I sequence is an extension from 2D ^{23}Na MRF to a 3D version, based on a 3D center-out radial sequence with DA readout gradients [26]. A schematic of the sequence is displayed in figure 17.

The MRF I sequence uses the same FA pattern as the 2D sequence and the TE pattern only differs by a constant offset of $-1.0\,\text{ms}$: $TE_{3D}(i) = TE_{2D}(i) - 1\,\text{ms}$. This TE reduction is possible because no slice selection rewinder gradients are needed due to the use of non-selective excitation pulses.

Similar to the 2D MRF sequence, the readout direction of each PT was changed to homogeneously cover a sphere in k-space. Furthermore, within each PT all readout directions are successively rotated by the 13th tiny golden angle [43] to allow full k-space coverage over the time dimension, as illustrated in figure 18. The tiny golden angles lead

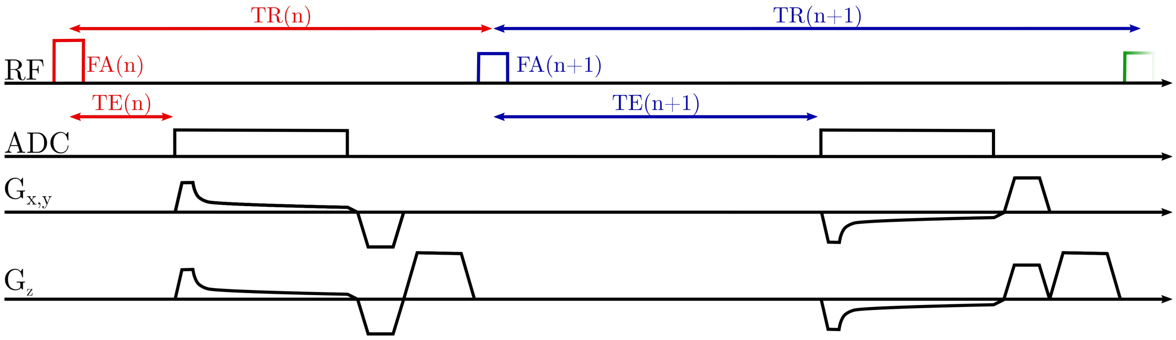

Figure 17: A schematic of the 3D MRF I sequence is shown, which starts with a non-selective excitation pulse with variable amplitude. Both FA and TE pattern were adopted from the 2D MRF sequence (figure 15). However, the TE pattern was globally reduced by 1 ms, which was enabled by the absence of a rewinder gradient after slice selection. A density adapted readout gradient was used for spatial encoding, followed by a rewinder and a spoiler gradient. Sequence timings are not to scale. Image adapted from [36].

to a similar k-space coverage as the conventional golden angles but with decreased eddy currents, due to the smaller angle increment.

In each cycle the VERSE pulses are replaced by rect pulses with a duration of 1 ms. Similar to the 2D sequence, the excitation is followed by a variable TE, a readout and a rewinder gradient, which nulls the 0^{th} gradient moment. Finally, a spoiler gradient is applied in z-direction to dephase the magnetization in each voxel by 2π before the next excitation pulse.

Since the required duration of both the rewinder and the spoiler gradient are resolution-dependent, the time after the readout is unique to the nominal image resolution of the measurement. The common image resolutions of $(3\,\text{mm})^3$ and $(5\,\text{mm})^3$ were used in this work. The delays between readout and next excitation pulse for the latter were 3.79 ms and 2.58 ms for the gradient system used in this work.

To accurately reconstruct the relaxation parameters, the different delays were taken into account in the dictionary simulations, which were based on ISTOs, as described in section 3.4.2.

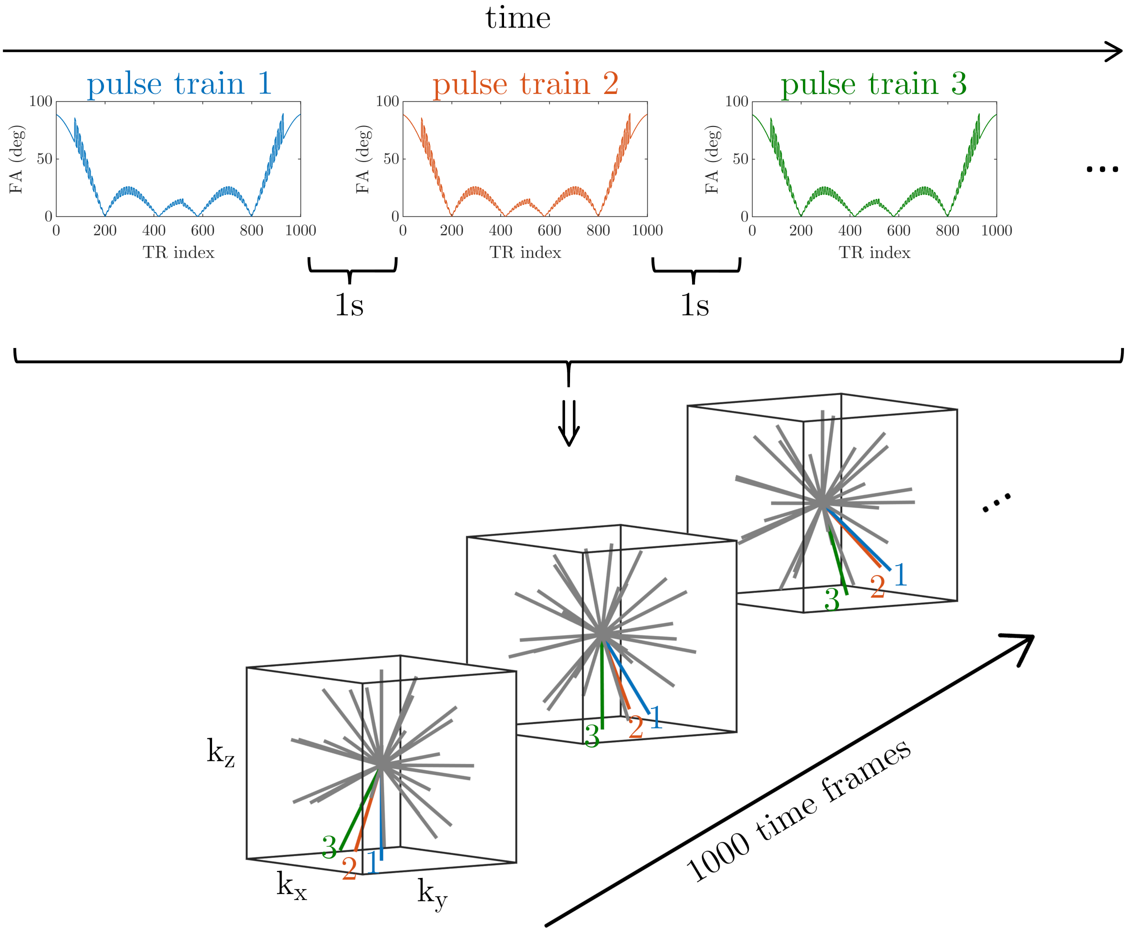

Figure 18: The spatial encoding of 3D MRF is illustrated. The first pulse train (blue) results in acquisition of 1000 successively rotated time frames in k-space, containing one spoke each. Relaxation of the magnetization towards thermal equilibrium is allowed by inserting a pause of 1 ms. Consequently, the second pulse train (red) results in acquisition of a second spoke in the same time frames. Hence, acquisition of N_{PT} results in 1000 rotated time frames, each containing N_{PT} spokes. Image adapted from [36].

3.3.3 3D ^{23}Na MRF II

The 3D MRF II sequence is based on MRF I with two major improvements.

Looking at the sequence diagram of the MRF I sequence (figure 17), it becomes apparent that the measurement time is not used efficiently since long TEs result in long waiting periods without data sampling. This becomes even more evident when comparing the total duration of a PT ($\sim 25\,\mathrm{s}$) with the sum of all echo times (10.53 s) within one PT.

Thus, approximately 42 % of the PT duration are waiting periods and therefore unused time. Since the TE pattern is a random distribution, a certain percentage will have a TE-delay longer than the time required for an additional readout.
Hence, the readout efficiency was increased by inserting an extra readout between the pulse and the original readout in those cases. This allows 425 extra readouts per pulse train, resulting in acquisition of 1425 time frames per PT without changing the duration of the latter. The echo times of these extra readouts $\mathrm{TE}_{\mathrm{add}}$ are also varied, ranging from 0.55 ms to 5.05 ms to improve encoding of the short transverse relaxation time. Here, the 425 echo times, suitable for acquisition of an additional echo, are binned into 10 subsets. The echo times (0.55, 1.05, …, 5.05) ms were assigned to the bins, ensuring a homogeneous $\mathrm{TE}_{\mathrm{add}}$ distribution in the specified range. A schematic sequence diagram for MRF II is shown in figure 19.

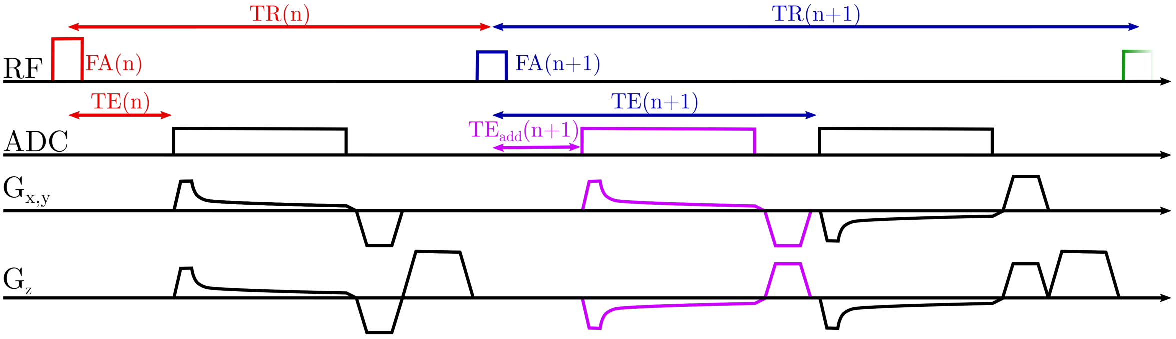

Figure 19: The 3D MRF II sequence differs from the MRF I sequence in two ways. First, an optimized FA pattern was used, shown in figure 20. Second, an additional spoke, illustrated in purple, was acquired when the current TE was longer than the time required for data acquisition and rewinding of the 0^{th} gradient moment. The echo time $\mathrm{TE}_{\mathrm{add}}$ of the additional readout was varied between 0.55 ms and 20.55 ms. Image adapted from [36].

Second, an improved FA pattern was implemented, illustrated in figure 20. It was numerically optimized using the CRLB, as described in section 4.2.1.1.
For this sequence four dictionaries were calculated. First, dictionaries based on ISTOs for the isotropic resolutions of $(3\,\mathrm{mm})^3$ and $(5\,\mathrm{mm})^3$ were constructed. Second, two additional dictionaries were calculated based on Bloch equations to investigate the impact of the signal model on the quantified parameters.

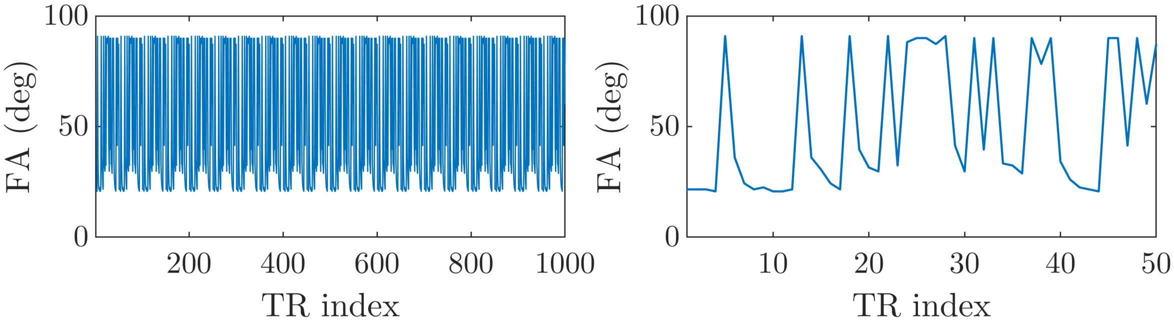

Figure 20: The 3D FA pattern was numerically optimized using the CRLB, as discussed in section 4.2.1.1. Due to the computational burden, only 50 consecutive FAs were optimized and concatenated 20 times to yield 1000 pattern entries. The full pattern is shown on the left, whereas the right subfigure illustrates the 50 entries after optimization. Image adapted from [36].

3.4 Dictionary simulations

In the following, the dictionary simulation process is described. The 2D sequence was used as a proof of concept, wherefore a simplified model based on Bloch equations was used for the dictionary simulation for a start. This comes with the advantage of reduced computational burden and well-evaluated pre-excisting simulation code.

When the feasibility of 2D MRF was shown, two 3D MRF sequences were developed and a sophisticated ISTO simulation was implemented to cover the full spin dynamics of spin 3/2 nuclei. For the MRF II sequence, an additional Bloch dictionary was calculated to investigate the differences in the results for the two signal models.

All dictionaries were compressed using an SVD, as described in section 3.4.3.

3.4.1 2D MRF dictionary simulation

The dictionary for the 2D MRF sequence was simulated using a Bloch model, implemented in MATLAB and accelerated by the use of GPUs. Here the effect of RF pulses, divided into n time steps, can be simulated using a rotation matrix R around the effective field $\vec{B}_{eff}$. The magnetization $\vec{M}_{i+1}$ is then a function of the previous state:

$$\vec{M}_{i+1} = R\vec{M}_i. \tag{3.7}$$

In the absence of an RF pulse, the system can be described by

$$\vec{M}_{i+1} = A\vec{M}_i + B, \tag{3.8}$$

with

$$A = \begin{pmatrix} e^{-\frac{\Delta t}{T_2}} & 0 & 0 \\ 0 & e^{-\frac{\Delta t}{T_2}} & 0 \\ 0 & 0 & e^{-\frac{\Delta t}{T_1}} \end{pmatrix} \tag{3.9}$$

and

$$B = \begin{pmatrix} 0 \\ 0 \\ 1 - e^{-\frac{\Delta t}{T_1}} \end{pmatrix}. \tag{3.10}$$

Consequently, the state after the RF pulse can be expressed as

$$\vec{M}_n = A_n \left(R_n \left(\ldots \left(A_2 \left(R_2 \left(A_1 \left(R_1 \vec{M}_0 \right) + B_1 \right) \right) + B_2 \right) \ldots \right) \right) + B_n, \tag{3.11}$$

which allows description of the state of the magnetization at any given point.
This approach was used to simulate a dictionary for the 2D MRF sequence. Here, $T_2^* = T_2$ was assumed to reduce the computational burden and because the relaxation times are in the order of TR. The Bloch model was adapted to yield biexponential transverse relaxation behavior by simulating two pools with similar parameters except for T_2^*, where one pool was characterized by $T_2^* = T_{2l}^*$ and the other pool by $T_2^* = T_{2s}^*$. This allowed construction of a biexponential transverse relaxation by summation of the signals of both pools at the end of the simulation, weighted with a ratio of 0.6/0.4.
The simulation was initialized with the relaxation times and all sequence relevant parameters. Spatial variations of the excitation slice profile were considered by simulating 401 independent isochromats distributed equidistantly along the slice direction covering 3.4 times the slice thickness. A 20 µs temporal grid was used to simulate the VERSE pulse and the corresponding VERSE slice selection gradient. Summation of the complex transverse magnetization along the slice direction at the end of the simulation resulted in a complex signal evolution for each parameter set.
In this work, the biexponential parameter space was: $T_1 = [20, 21, \ldots, 70]$ ms, $T_{2l}^* = [15, 16, \ldots, 60]$ ms, $T_{2l}^* = [1.0, 1.3, \ldots, 14.8]$ ms and $\Delta B_0 = [-60, -58, \ldots .60]$ Hz. Tissues experiencing a monoexponential relaxation, such as CSF, were considered in: $T_1 = [30, 31, \ldots, 90]$ ms, $T_2^* = [5, 6, \ldots, 80]$ ms and $\Delta B_0 = [-60, -58, \ldots, 60]$ Hz.
The biexponential and the monoexponential signals were concatenated to yield a single dictionary, which was compressed as described in section 3.4.3.

3.4.2 3D MRF dictionary simulation

To enable simulation of the full spin dynamics of sodium, an ISTO simulation was implemented for the 3D MRF sequences.

3.4.2.1 ISTO simulations

An ISTO simulation was implemented as described in section 2.3, which is based on the model by Hancu et al. [20]. However, two additional steps regarding the relaxation

times, were considered in this work as described in the following.
The ISTO model inherently yields a biexponential relaxation for both the transverse and the longitudinal magnetization. However, fitting of a biexponential inversion recovery curve to determine the longitudinal relaxation components is challenging, wherefore in literature the longitudinal relaxation is commonly described with a single monoexponential relaxation constant T_1.
Hence, in this work a monoexponential T_1-estimate was constructed, as illustrated in the following. Considering a biexponential function $ae^{a't} + be^{b't}$ with $a + b = 1$, a first order Taylor expansion yields

$$\begin{aligned} ae^{a't} + be^{b't} &= a\sum_{n=0}^{\infty}\frac{(a't)^n}{n!} + b\sum_{n=0}^{\infty}\frac{(b't)^n}{n!} \approx (a+b) + aa't + bb't \\ &= 1 + (aa' + bb')t \approx \sum_{n=0}^{\infty}\frac{\big((aa' + bb'+)t\big)^n}{n!} = e^{(aa'+bb')t}. \end{aligned} \tag{3.12}$$

Comparison with equations 2.77 yields $a = 0.8$, $a' = \frac{-1}{T_{1l}}$, $b = 0.2$ and $b' = \frac{-1}{T_{1s}}$, which results in the monoexponential estimate

$$T_1 \approx \frac{1}{\frac{0.8}{T_{1l}} + \frac{0.2}{T_{1s}}}. \tag{3.13}$$

Equation 3.13 in conjunction with equations 2.75 and 2.63 leads to a bijective transformation

$$\begin{aligned} T_1 &= \frac{1}{1.6J_2 + 0.4J_1} \\ T_{2l} &= \frac{1}{J_1 + J_2} \\ T_{2s} &= \frac{1}{J_0 + J_1} \end{aligned} \tag{3.14}$$

and

$$\begin{aligned} J_0 &= \frac{5}{6T_1} - \frac{4}{3T_{2l}} + \frac{1}{T_{2s}} \\ J_1 &= \frac{4}{3T_{2l}} - \frac{5}{6T_1} \\ J_2 &= \frac{5}{6T_1} - \frac{1}{3T_{2l}}. \end{aligned} \tag{3.15}$$

In aqueous sodium solution, the inverse of the Larmor frequency is long compared to the correlation time ($\omega_0 \tau_c \ll 1$) and a monoexponential transverse relaxation is expected, wherefore $J_0 = J_1 = J_2$ has to be valid. This however results in $T_1 = T_2$, which is not found, when comparing the results of FID and IR experiments. This can be explained by intravoxel dephasing due to field inhomogenieties in the static field, resulting in the apparent transverse relaxation time T_2^* (T_{2s}^* and T_{2l}^* respectively). Assuming a Lorentzian off-resonance distribution p_L with a half width at half maximum (HWHM) χ_L yields:

$$T_x^* = \frac{1}{2\pi\chi_L + \frac{1}{T_x}}, \tag{3.16}$$

where $x \in \{2, 2s, 2l\}$.

These considerations were used in the dictionary simulation process as explained in the following.

Three versions of the quantitative signal simulation were implemented, which are equivalent and only differ in their computational performance for different sizes of parameter sets as explained below. The simulations are initialized with the sequence (FA pattern, timings, spoiling) and sample parameters $(T_1, T_{2l}, T_{2s}, \Delta B_0)$. In a first step, the relaxation times are converted into spectral density parameters using equation 3.15. Each parameter combination is represented by 100 isochromats to allow dephasing and potential formation of spin echoes and stimulated echoes. The interaction matrices M (see appendix, equations 7.1 and 7.2) are constructed for each parameter combination for both cases with and without presence of an RF pulse. Subsequent application of a numerical eigenvalue decomposition on M allows solving of equation 2.55 for each sequence event, which enables simulation of the spin dynamics for each time step. Phase spoiling was implemented by applying a phase of 2π over the sample using equation 2.35. The signal for the fingerprint is extracted using $s(t) = T_{11}(a)(t) - T_{11}(s)(t)$, summed over all isochromats. Consequently, the simulation is independent of the spatial encoding in the MRF sequence.

In this work, the parameter space for the 3D dictionaries was $T_1 = [20,\ 21,\ \ldots,\ 70]\,\text{ms}$, $T_{2l} = [15,\ 16,\ \ldots,\ 50]\,\text{ms}$, $T_{2s} = [1.0,\ 1.3,\ \ldots,\ 14.8]\,\text{ms}$, $\omega_Q = 0$ and $\Delta B_0 = [-50,\ -48,\ \ldots,\ 50]\,\text{Hz}$ for the biexponential dictionary part. Monoexponential tissues, such as CSF, were taken into account in the monoexponential part: $T_1 = T_2 = T_{2l} = T_{2s} = [20,\ 21,\ \ldots,\ 90]\,\text{ms}$, $\omega_Q = 0$ and $\Delta B_0 = [-50,\ -48,\ \ldots,\ 50]\,\text{Hz}$. Parameter sets that violate $0 < J_2 < J_1 < J_0$ were neglected, for example $(T_1, T_{2l}, T_{2s}) = (20,\ 50,\ 5)\,\text{ms}$ $\hat{=} (J_2, J_1, J_0) = (35,\ -15,\ 215)\,\text{Hz}$.

To introduce T_2^*, an off-resonance range of ± 100 Hz was simulated around each central off-resonance $\Delta B_0 \in [-50,\ -48,\ \ldots,\ 50]$ Hz, yielding $\overline{\Delta B_0} = [\Delta B_0 - 100, \Delta B_0 - 99, , ..., \Delta B_0 + 100]$ Hz. Subsequently, the signals were interpolated along the $\overline{\Delta B_0}$-axis to yield a step size of 0.5 Hz. Different T_2^* decays were constructed by summation of the signals along the $\overline{\Delta B_0}$-axis with varying χ_L, such that $T_2 > T_2^* > 0.4T_2$ in 1 ms steps. For the biexponential case $T_{2l} > T_{2l}^* > 0.6T_{2l}$ was chosen. Since T_{2s}^* changes less then T_{2l}^* (compare equation 3.16), here a step size below 1 ms is automatically achieved.

The biexponential and the monoexponential signal sets were concatenated to construct a single dictionary, which was subsequently compressed as explained in paragraph 3.4.3.

Three equivalent versions of the simulation were implemented, optimized for different scenarios: The first version was implemented in MATLAB and runs on the CPU. This version is the fastest if the signal evolution of only a small number of parameter combinations is of interest (e.g. the FA optimization, see section 4.2.1.1). Secondly, a GPU-accelerated version was implemented, allowing fast calculation of medium-sized parameter sets. In spirit of reproducible research, both of the latter implementations are published [36] and can be found online under `https://github.com/7TGroupDKFZ/ISTO_MRF`.

The last simulation version was tailored to calculate large data sets, such as complete dictionaries, using the computational infrastructure at the German Cancer Reserach Center (DKFZ) at the time of this thesis. Here, the simulation starts with the pre-computing of the spectral density parameters and the parallelized eigenvalue decomposition required for solving equation 2.55, which is performed on two OpenStack clusters (28 logical processors: Intel Broadwell family 6 model 61, 240GB RAM). The pre-computed objects are subsequently sent to the GPU-cluster (10x(Nvida V100)). Here, the signal evolution is computed for each set of inputs, implemented in PYTHON 3.7. Last, the resulting signal evolutions and the corresponding LUTs are send to a MATLAB worker (32 logical processors Intel Xeon E5-2650 v2, 512GB RAM), where the Lorentz-combination and the SVD are performed (see subsection 3.4.3). In this setup, a total duration of 2-3 days, depending on the exact sequence and parameter space, was required to simulate a dictionary.

3.4.2.2 Bloch simulations

For the MRF II sequence an additional Bloch dictionary was calculated to evaluate the benefit of ISTO simulations over the simplified Bloch model.

Here, the Bloch simulation used for 2D dictionary calculation was applied. However, to allow a fair comparison between the ISTO and the Bloch model, the exact same dictionary entries were considered for the Bloch and the ISTO simulation. Further, T_2^*-effects were taken into account using the same approach through the Lorentz-distribution as in the ISTO simulations.

3.4.3 Dictionary compression

All entries in each dictionary were normalized, such that the $\mathcal{L}_2$-norm of each signal evolution is equal to 1. Next, the dictionaries were compressed in MATLAB using an SVD up to rank 12, which improves data handling and highly reduces the computational burden in the reconstruction. Furthermore, the low rank compression is useful for denoising of the data in the reconstruction.

3.5 MRF reconstruction

The reconstruction of the MRF data is explained in the following, which is valid for both 2D MRF and 3D MRF. The different readout trajectories are taken into account in the NUFFT operators.

An offline reconstruction pipeline was developed, which retrieves all imaging parameters required for reconstruction, such as number of spokes and k-space sampling trajectories from the measurement data header.

As described in section 3.1.1, a single channel birdcage RF coil and an RF coil with 30 receive channels were used in this work. To reconstruct data acquired with the latter, sensitivity maps are required, whose construction is explained below the MRF reconstruction section.

3.5.1 LR ADMM reconstruction

Quantitative parameter maps were reconstructed using a low rank alternating direction method of multipliers (LR ADMM) approach, proposed by Asslaender at al. [32] as explained in theory section 2.6.3. Here, a conjugate gradient (CG) algorithm based on NUFFT operators is used to iteratively reconstruct the measured data in the compressed image space, sorted by their weights. For the 3D data, the LR ADMM approach was reduced to its CG part in order to increase the reconstruction speed. In case of multi-channel data, sensitivity maps, whose construction is described below, were intrinsically used in the NUFFT operators. An $\mathcal{L}_2$-norm in the wavelet domain was applied as spatial regularization (2D: $\lambda_{phantom} = 1 \times 10^{-2}$ and $\lambda_{invivo} = 5 \times 10^{-2}$; 3D: $\lambda = 0$) and the spatial information is recovered in the compression process, as illustrated in figure 21.

The quantitative parameter maps were extracted for each pixel by finding the highest scalar product between the pixel coefficients in the compressed basis and all dictionary entries. This approach intrinsically determined if the given pixel decayed with bi- or monoexponential relaxation without prior knowledge.

In the following, monoexponential pixels are masked in all T_{2l}^* and T_{2s}^* maps in pink and biexponential pixels are masked in the T_2^* maps, respectively. Moreover, when mean and SD were calculated, monoexponential pixels were excluded from analysis in mainly biexponential areas and vice versa.

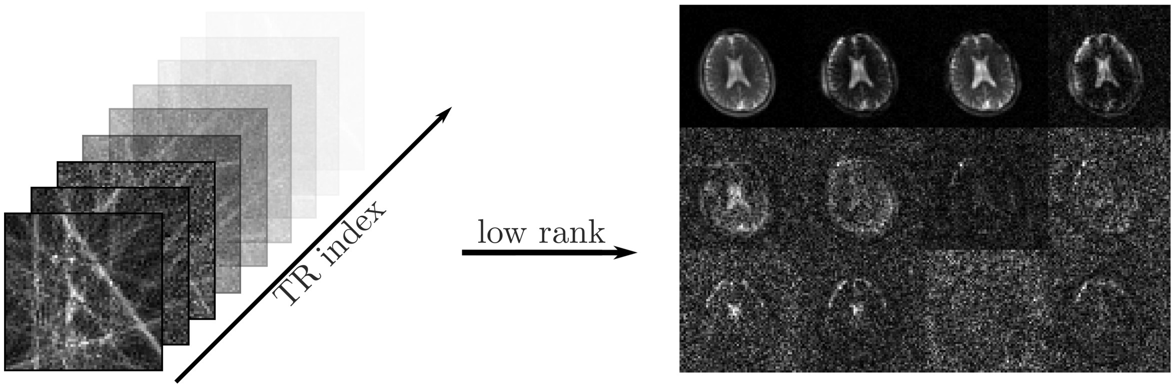

Figure 21: Applying the SVD compression onto the MRF data in image space yields the approximated data in the compressed basis and the spatial information is recovered. Voxelwise comparison of the signal evolution with the simulated dictionary allows retrieving of the relaxometric parameters. Image adapted from [40].

3.5.2 Reconstruction of sensitivity maps

Sensitvity maps are required to accurately reconstruct the phase information in the image domain in multi-channel MRI. To determine the sensitivity maps, each time frame of the measured data was reconstructed with a NUFFT operator for each receive coil individually. Next, complex summation of all time frames yielded a single image for each receive coil. These images were converted into Cartesian k-spaces, which were then used to construct the sensitivity map of each coil using an ESPIRiT approach [44].

3.6 Simulation experiments

In this work numerical simulations were used to investigate a variety of applications, such as the construction of suitable FA patterns, the minimal number of spokes, PV effects and parameter bias due to B_1 inhomogeneities.

This section is supposed to shortly give a general idea on the basic concepts of those simulations. The specifics of each simulation are described in the corresponding result sections. All simulations were implemented in MATLAB if not stated otherwise and can be divided into two groups: the signal simulations and the spatial simulations, as discussed in the following.

3.6.1 Signal simulation experiments

Signal simulations were used for investigations which needed no spatial information. These were the determination of the distinguishability of different signal evolutions, parameter bias due to PV effects, impact of B_1 deviations and comparison between the ISTO and the Bloch model.

The signal simulations were all based on either the ISTO or the Bloch simulation framework, described in section 3.4.

3.6.2 Spatial simulation experiments

Spatially resolved simulations were performed to investigate the feasibility of ^{23}Na MRF, to determine the minimal number of spokes for the 2D sequence and for investigation of the achievable image resolution with 3D MRF. These simulations all aimed to construct a numerical k-space, which was subsequently fed into the same reconstruction pipeline as used for the measured data.

The 2D simulations were performed by applying NUFFT operators [37] on different compartments of a numerical head model [45], yielding a separate k-space for each compartment and time frame. Due to k-space linearity, this allowed summation of the time frames, weighted by complex scaling factors to describe both the ^{23}Na concentration and the current transient state.

The achievable image resolution for the 3D MRF framework was investigated by analytically calculating the k-space of each compartment with the Fourier Domain method proposed by Koay et al. [46]. Again, the k-spaces were weighted with the simulated signal evolutions and then summed up.

3.7 Measurements and data analysis

In the following section the measurements conducted in this work are summarized. The ^{23}Na transmitter voltage was adjusted at the beginning of each measurement session, as described in section 3.2.2.

3.7.1 2D measurements

The 2D MRF sequence was used to show the feasibility of ^{23}Na relaxometric mapping using MRF. The measurements conducted are illustrated in the following.

3.7.1.1 Phantom measurements

The 2D MRF sequence was validated in phantom 1 with the birdcage coil by comparing relaxometric maps acquired with MRF with results obtained with reference methods. The following measurements were all acquired in the same 2D slice with a nominal resolution of $2 \times 2 \times 12\,\mathrm{mm}^3$ using density adapted readout gradients (512 samples, $G_0 = 20\,\mathrm{mT/m}$, $t_0 = 120\,\mu\mathrm{s}$). Further, all sequences applied a sinc pulse ($\tau = 1.024\,\mathrm{ms}$, BWT = 2.7), except for the MRF sequence, where the latter was modified using a VERSE routine [47].

The 2D MRF sequence was acquired with 14 spokes per time frame, based on the simulation results (see section 4.1.1). This, in conjunction with the use of 11 averages, yielded a measurement time of 1:00h. The VERSE pulses were constructed such that the maximal RF amplitude of the VERSE pulse was half the maximal amplitude of the initial sinc pulse.

The reference maps of the transverse relaxation times were determined by acquiring an image stack with varying TE using a single-echo GRE sequence. Both a bi- and a monoexponential relaxation model were fitted pixelwise to the data, as discussed in section 3.2.3.2. The imaging parameters are summarized in table 2. The FA was limited to 60° due to SAR and pulse-voltage constraints. Acquisition of 18 echoes resulted in a total measurement duration of 3:12h.

The longitudinal relaxation times were mapped using an inversion recovery sequence. As illustrated in section 3.2.3.1, here a non-selective inversion pulse, a sinc pulse and DA readout gradients were used. Again, the sinc pulse was similar to the pulse in the MRF sequence but without the use of a VERSE routine. The total duration for acquisition of an image stack with 10 inversion times (see table 2) was 1:40h.

Table 2: Overview of the sequence parameters used in 2D phantom measurements. All sequences used DA readout gradients (512 samples, $G_0 = 20\,\mathrm{mT/m}$, $t_0 = 120\,\mathrm{\mu s}$) and were acquired with a nominal resolution of $2 \times 2{\times}12\,\mathrm{mm}^3$.

	FA(deg)	TE and TI (ms)	TR (ms)	spokes	averages	TA (h)
2D ^{23}Na MRF	0 to 90	TE = 1.55 to 21.55	13.34 to 33.34	14 × 1000	11	1:00
GRE ($T^*_{2l}, T^*_{2s}, T^*_2$)	60	TE = [1.24, 1.35, 2.0, 2.5, 3.0, 4.0, 5.0, 6.0, 7.0, 9.0, 13, 17, 23, 27, 35, 40, 50, 60]	200	320	10	3:12
GRE (ΔB_0)	45	TE = [1.55,6.55]	25	320	20	0:05
IR-GRE (T_1)	180, 63	TE = 1.34; TI = [3.2, 10, 20, 40, 70, 100, 130, 160, 200, 250]	300	200	10	1:40

To compare the results of the MRF and the reference measurements, mean and SD of all relaxation times were quantified in each phantom compartment. In this process, each compartment was assigned to either bi- or monoexponential transverse relaxation, based on the ratio $\frac{N_{bi}}{N_{bi}+N_{mono}}$ and mismatched voxels were excluded from numerical analysis. The ΔB_0 maps were compared visually and by calculating the mean absolute difference between the ΔB_0 maps $\frac{\sum^N |\Delta B_{0,MRF}-\Delta B_{0,reference}|}{N}$.

3.7.1.2 In vivo measurements

The 2D MRF sequence was used to perform an in vivo study in five healthy volunteers ([22, 23, 24, 24, 25] years, 3 female and 2 male) with approval from the local ethics committee and according to the institutional guidelines. Here, the 30-Ch head coil was used to increase the SNR. A nominal resolution of $4 \times 4{\times}12\,\mathrm{mm}^3$ (512 samples, $G_0 = 9\,\mathrm{mT/m}$, $t_0 = 100\,\mu\mathrm{s}$) was used and 7 spokes were acquired per time frame, based on the simulation results (see section 4.1.1). To increase the SNR, 21-fold averaging was performed, resulting in a scan duration of 1:00h. Subsequently, a TSE sequence (TE = 72 ms, TR = 3000 ms, $(0.7\,\mathrm{mm}–0.8\,\mathrm{mm})^2$ in-plane resolution) with the same slice thickness as the ^{23}Na MRF measurement was applied to acquire ^{1}H images. The latter were co-registered onto a sodium image, constructed by summation of all MRF time frames in the image domain. Mean and SD of the ^{23}Na relaxation times were then quantified in BT and CSF ROIs, which were manually drawn in the TSE images. Again, biexponential voxels in predominantly monoexponential areas were neglected in the numerical analysis and vice versa.
The influence of undersampling on the quantified parameters was investigated by measuring volunteer 1 for a second time with the same protocol but using 147 instead of 7 spokes per time frame and a single average instead of 21. This resulted in the same measurement duration and fulfilled the Nyquist criterion of approximately 140 spokes.

3.7.2 3D measurements

When the feasibility of ^{23}Na MRF was shown using the 2D sequence, two 3D MRF sequences were developed for more time-efficient relaxometric mapping. The measurements conducted are illustrated in the following.

3.7.2.1 Phantom measurements

The 3D MRF sequences were benchmarked using the phantom 2 (figure 11) and the birdcage coil. The following phantom measurements were all acquired in the same measurement session to guarantee a similar position in the scanner, spatial alignment between the measurements and a similar B_0 shim. Further, a nominal resolution of $(3\,\mathrm{mm})^3$ and a readout duration of 10 ms with 384 samples per spoke were used. The sequence parameters are summarized in table 3. After B_0 shimming and determination of the ^{23}Na reference voltage, a measurement with the MRF II sequence was performed. Here, 150 pulse trains were acquired, resulting in a scan duration of 1:04h. Next, the off-resonance distribution was acquired with a phase difference measurement, followed by an MRF I measurement. Subsequently, the B_0 shimming was repeated to eliminate potential phase drifts; however, none were observed. To allow mapping of the reference transverse relaxation times, four GRE measurements with eight echoes each were acquired, which resulted in a total scan duration of 0:56h. Subsequently, T_1 maps were acquired by measuring a set of IR scans, which required 5:48h.

The impact of virtually reduced measurement time on the parameters was investigated by retrospective undersampling of the MRF II data. Here, only every [2nd, 3rd, 4th, 6th, 9th, 25th] spoke of each time frame was reconstructed to yield reduced virtual measurement times of [32, 21, 16, 11, 7.3, 2.6] min.

Table 3: Overview of the sequence parameters used in 3D phantom measurements. All sequences were acquired with a nominal resolution of $(3\,\mathrm{mm})^3$ and density adapted readout gradients (384 samples, $G_0 = 7.55\,\mathrm{mT/m}$, $t_0 = 150\,\mathrm{\mu s}$).

	FA(deg)	TE and TI (ms)	TR (ms)	spokes	averages	TA (h)
3D MRF II	20 to 91	TE = 0.55 to 20.55	14.8 to 24.8	150 × 1425	1	1 : 04
GRE (ΔB_0)	45	TE = [0.55,5.55]	25	8000	1	0 : 07
3D MRF I	0 to 90	TE = 0.55 to 20.55	14.8 to 24.8	150 × 1000	1	1 : 04
multi-echo GRE ($T_{2l}^*, T_{2s}^*, T_2^*$)	60	TE = [0.35, 2.1, 3.85, 5.6, 12.4, 14.1, 15.9, 17.6, 24.4, 26.1, 27.9, 29.6, 36.4, 38.1, 39.9, 41.6, 48.4, 50.1, 51.9, 53.6, 60.4, 62.1, 63.9, 65.6, 72.4, 74.1, 75.9, 77.6, 84.4, 86.1, 87.9, 89.6]	120	7050	1	0 : 56
IR-GRE (T_1)	180, 90	TE = 0.55; TI = [4, 20, 40, 70, 100, 130, 170, 200, 250]	290	8000	1	5 : 48
Phase sensitive (B_1)	90	TE = 0.55	190	3800	1	0 : 24

3.7.2.2 In vivo measurements

The relaxation times in the human head were determined in an in vivo study, conducted in four healthy volunteers ([25, 24, 26, 27] years, 1 female and 3 male) with the MRF II sequence. Here, a nominal resolution of $(5\,\mathrm{mm})^3$ was used and 150 pulse trains were acquired ($\mathrm{TRO} = 10\,\mathrm{ms}$, $N_{samples/projection} = 384$), resulting in a measurement duration of 1:04h.

Mean and SD of the relaxation times were determined in BT and CSF. The ROIs were drawn in seven central slices of the first coefficient image in the compressed basis. To decrease PV effects on the quantified parameters, border voxels between different tissue types were eroded. To estimate the impact of virtually reduced measurement time on the quantified in vivo parameters, the data was retrospectively undersampled to yield virtual measurement times of [32, 21, 11, 6.4] min. These experiments suggested that a 32 min measurement yields a good compromise between image quality and scan duration. Hence, volunteer 4 was measured a second time with reduced number of spokes per time frame (75 PTs) and therefore with a shortened scan duration of 32 min.

4 Results

This chapter presents the development and validation of both the 2D and the 3D MRF frameworks. First, the 2D MRF simulation experiments are illustrated, which were used for FA pattern design and for investigation of the MRF quantification capabilities in spatially resolved simulations. Phantom measurements were used for validation of the 2D MRF sequence by comparison of the quantified parameters with gold standard references. This was followed by an in vivo study with the objective to quantify the relaxation parameters in the human head. Next, the 3D MRF sequences were developed, where multiple simulation experiments were applied for improvement and evaluation of the 3D MRF framework. A subsequent phantom study was conducted to compare the encoding capabilities of the two 3D MRF sequences with the references. Last, a second in vivo study was performed with the final MRF sequence developed in this work.

4.1 2D MRF

In the following, the 2D MRF results are presented, parts of which are published in [40].

4.1.1 Simulation experiments

Simulations were applied to determine the minimal number of spokes and to test the 2D ^{23}Na MRF sequence with two different FA patterns. The first pattern (see section 2.6, figure 8) is identical to the ^{1}H FISP MRF pattern reported by Jiang et al. [31], but without the inversion pulse. The inversion was not applied to reduce the SAR demands and because of its limited effectiveness due to short relaxation times of ^{23}Na nuclei. The second FA pattern was heuristically designed to improve the T_1 encoding and its construction is described in the following.

4.1.1.1 2D MRF FA pattern design

To improve the T_1 encoding, various FA patterns were constructed from combinations of sine, sawtooth wave, step and sinc functions and their encoding capabilities were compared based on their auto-correlations. The correlations were determined by calculating the scalar product between one BT-simulating fingerprint ($T_1 = 37\,\text{ms}$, $T_{2l}^* = 40\,\text{ms}$, $T_{2s}^* = 4.6\,\text{ms}$) and the other signal evolutions in the T_1-T_{2l}^*- and the T_1-T_{2s}^*-plane of the dictionary (see section 3.4.1). Monoexponential relaxation was taken into account by calculating the correlations in the T_1-T_2^*-plane through a CSF-like entry ($T_1 = 64\,\text{ms}$,

$T_2^* = 56\,\text{ms}$). The entries above 99.95 % were counted in each correlation plane as a measure of specificity and the FA pattern with the lowest count was chosen. It is shown in section 3.3.1, figure 15 and consists of two half sinc functions, starting and ending with the highest entry. Stepwise modulations were imprinted onto the pattern, toggeling the amplitude between the initial value and the value scaled by 4/3 every five cycles. These rapid changes were found to improve the T_1 encoding, which later was confirmed in the FA pattern optimization for the 3D MRF II sequence (see section 4.2.1.1). The resulting correlation plots are displayed in figure 22, where the number of correlations above 99.95 % was reduced by 33 % compared to the ^{1}H FISP MRF pattern. This steeper correlation distribution corresponds to improved distinguishability between the entries and therefore hints increased specificity introduced by the new pattern.

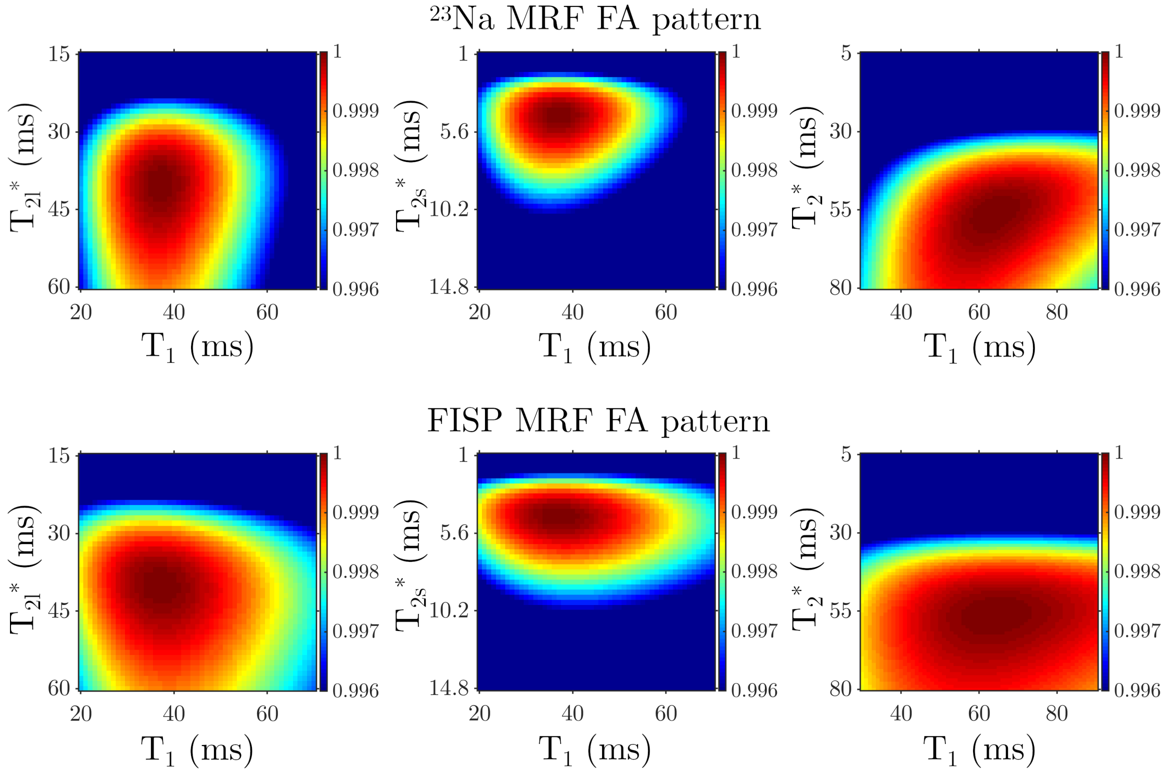

Figure 22: The auto-correlations in the T_1-T_{2l}^*- and the T_1-T_{2s}^*-plane were calculated for a BT-like parameter set ($T_1 = 37\,\text{ms}$, $T_{2l}^* = 40\,\text{ms}$, $T_{2s}^* = 4.6\,\text{ms}$) and in the T_1-T_2^*-plane for CSF ($T_1 = 64\,\text{ms}$, $T_2^* = 56\,\text{ms}$). The total number of correlations above 99.95 % in the proposed 2D FA pattern was reduced by 33 % with respect to the ^{1}H FISP MRF pattern. Image adapted from [40].

4.1.1.2 2D MRF imaging simulations

The imaging process was simulated to probe the impact of the two different FA patterns on the quantified parameters. Furthermore, the impact of different numbers of spokes on the resulting parameters was investigated and the minimal number of spokes was determined for the two nominal in-plane resolutions of $2{\times}2\,\mathrm{mm}^2$ and $4{\times}4\,\mathrm{mm}^2$.

The imaging process was simulated in a transverse slice through a numerical brain model [45], intersecting the ventricles. Here, a NUFFT operator [37] with N_s spokes was applied onto high resolution maps of GM, WM and CSF, which were scaled to the estimated sodium concentrations of 40 mmol/L, 30 mmol/L and 154 mmol/L. This was repeated 1000 times, where the readout directions were successively rotated by the golden angle, which resulted in 3×1000 k-spaces, one for each time frame and tissue type. Each k-space was then scaled with the corresponding theoretical signal evolution for the given MRF sequence, obtained with a Bloch simulation. Here, relaxation times of $T_1 = 37\,\mathrm{ms}$, $T^*_{2l} = 40\,\mathrm{ms}$ and $T^*_{2s} = 4.6\,\mathrm{ms}$ were assumed in BT (GM and WM), whereas CSF was simulated with $T_1 = 64\,\mathrm{ms}$ and $T^*_2 = 56\,\mathrm{ms}$. Next, the compartments were combined, yielding 1000 time frames in k-space, which were subsequently reconstructed similar to measured data, as explained in section 3.5.

To determine the minimal number of spokes, this procedure was performed for $N_s = [1, 2, ..., 15]$ for an in-plane resolution of $4{\times}4\,\mathrm{mm}^2$ and $N_s = [2, 4, ..., 30]$ for a resolution of $2{\times}2\,\mathrm{mm}^2$, where the heuristically constructed FA pattern was used. For each number of spokes, the mean and SD were calculated in the relaxometric maps for BT and CSF and the results are illustrated in figure 23 for the in-plane resolution of $2{\times}2\,\mathrm{mm}^2$. The results of the $4{\times}4\,\mathrm{mm}^2$ simulation are displayed in the appendix, figure 43.

The minimal number of spokes was defined such that the deviation of each quantified relaxation parameter was less than 5.0 % with respect to the results obtained with the maximal number of spokes. For the $2{\times}2\,\mathrm{mm}^2$ resolution, the minimal number of spokes per time frame was 14, whereas 7 spokes were found to be sufficient for a resolution of $4{\times}4\,\mathrm{mm}^2$. The resulting maps ($2{\times}2\,\mathrm{mm}^2$, $N_s = 14$) are shown in figure 24 in conjunction with the corresponding ground truth (GT) maps. Mean and SD of all relaxation times in BT and CSF were determined and are displayed in table 4. The mean absolute difference between MRF and the GT was 2.6 %, where the largest deviation was $-10.6\,\%$, found in T^*_{2s} in BT. Next, a simulation was conducted to compare the quantification capabilities of both FA patterns in presence of thermal noise. Here, k-space data were constructed for both patterns and complex Gaussian noise was added to the latter such that the reconstructed images visually matched some measured data. The resulting

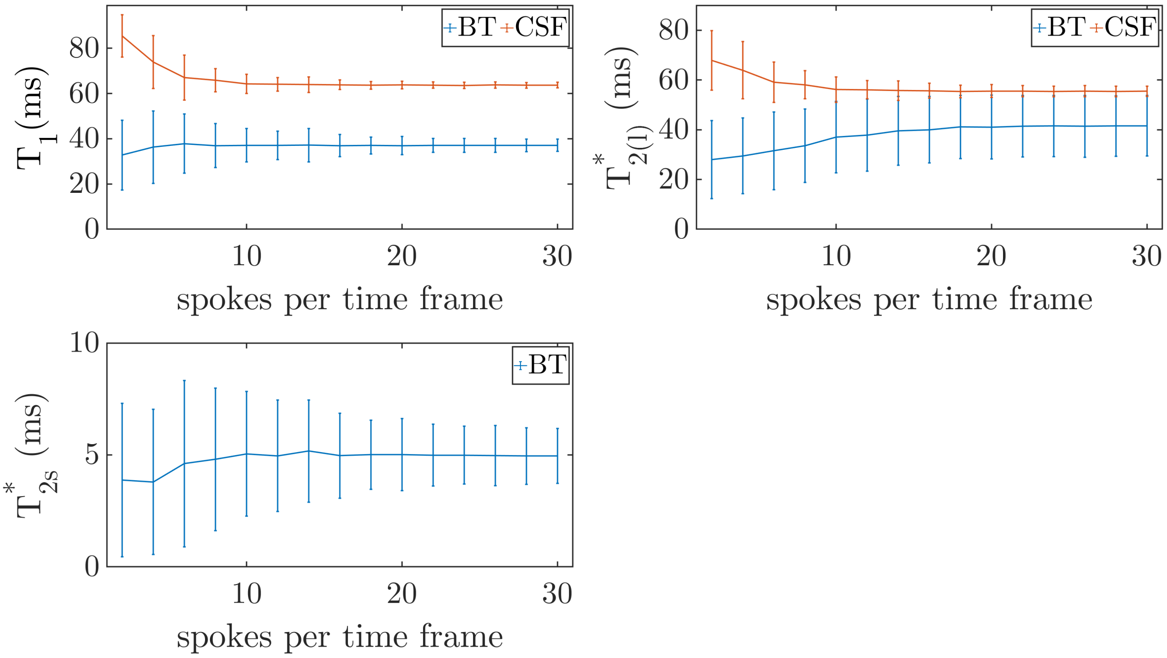

Figure 23: The mean and SD of the relaxation parameters in BT and CSF are illustrated for varying number of spokes per time frame and a nominal in-plane resolution of 2×2 mm^2. The minimal number of spokes per time frame was 14 as here the mean deviation of each quantified relaxation parameter was less than 5.0 % with respect to the results obtained with the maximal number of spokes. For the 4×4 mm^2 resolution a minimum of 7 spokes per time frame was found, as shown in the appendix, figure 43. Image adapted from [40].

maps, are shown in figure 24 and the quantified means and SDs are summarized in table 4. The largest bias was $-19.5\,\%$, found in the T^*_{2l} values of BT. The mean absolute difference between the ground truth and MRF with the ^{23}Na FA pattern was 4.7 %, whereas MRF with the ^{1}H FISP FA pattern deviated by 4.9 %. Consequently, the heuristically constructed pattern was used in the measurements.

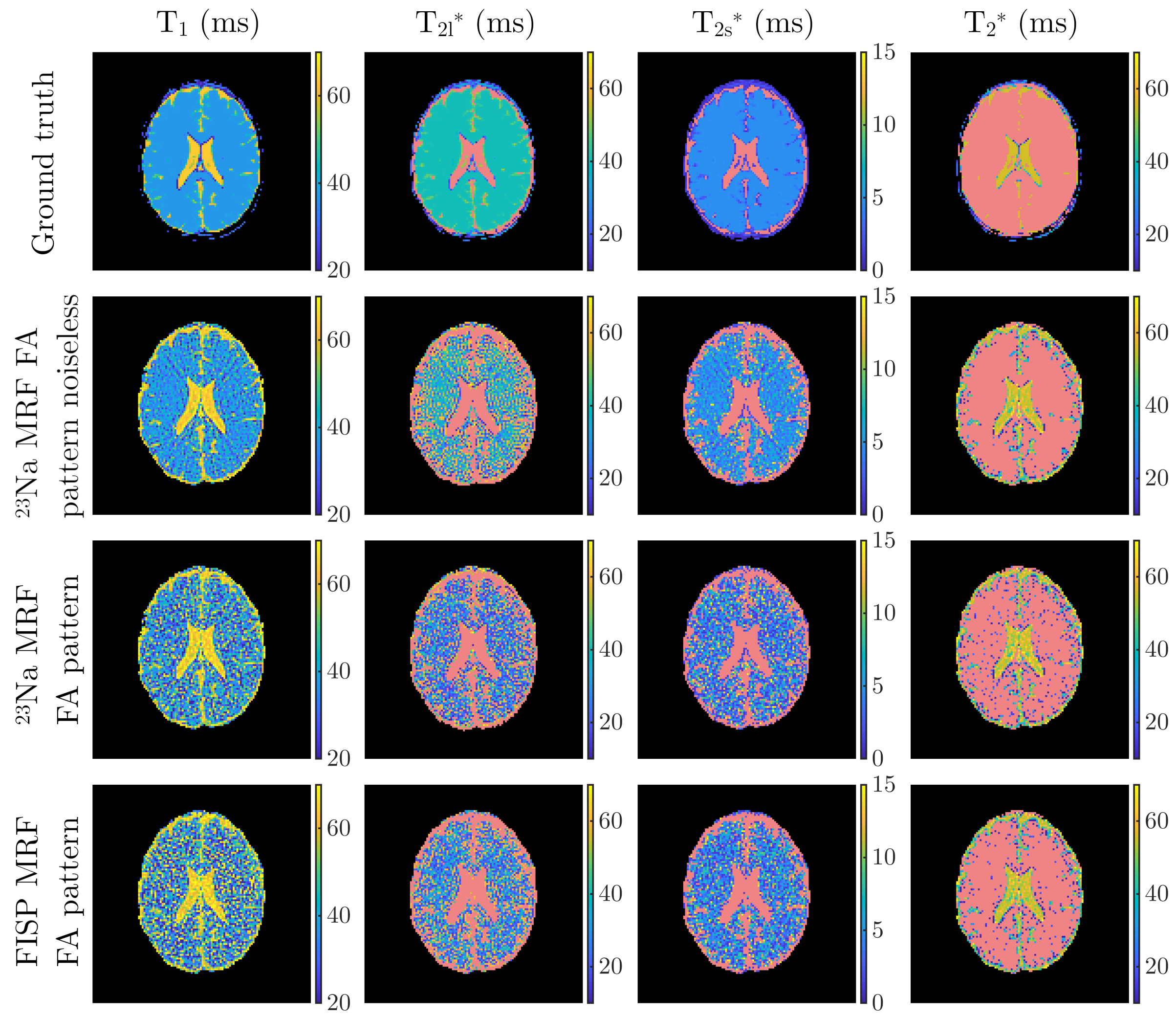

Figure 24: Simulation study of the 2D MRF framework in a numerical head phantom, intersecting the lateral ventricles. The ground truth maps are shown in the first row. Monoexponential voxels are masked in the T_{2l}^* and T_{2s}^* maps and vice versa in the T_2^* map. For simplicity, off-resonances were neglected in the simulations. Noiseless reconstructions of the 2D MRF framework are shown in the second row, whereas a comparison of the two FA patterns in presence of noise is illustrated in the third and fourth rows. Mean and SD in BT and CSF of each map are summarized in table 4. Image adapted from [40].

Table 4: Mean and SD were quantified in BT and CSF in all maps shown in figure 24.

	BT			CSF	
FA pattern	T_1 (ms)	T_{2l}^* (ms)	T_{2s}^* (ms)	T_1 (ms)	T_2^* (ms)
Ground truth	37.1	40.0	4.7	64.0	56.0
^{23}Na MRF, noiseless	37.2 ± 7.4	39.5 ± 13.8	5.2 ± 2.3	63.9 ± 3.4	55.7 ± 4.0
^{23}Na MRF	38.5 ± 13.3	32.2 ± 15.3	4.7 ± 3.5	63.9 ± 4.5	55.9 ± 5.1
FISP MRF	39.8 ± 16.3	33.7 ± 14.9	4.7 ± 3.2	63.7 ± 5.2	55.5 ± 3.9

4.1.2 Phantom measurements

Phantom measurements were conducted to validate the 2D MRF sequence by comparing the resulting parameter maps to the ones obtained with reference methods. The measurements and the corresponding sequence parameters (table 2) are described in section 3.7.1.

The measured T_1 maps acquired with both MRF and the reference method are shown in figure 25 in conjunction with the determined off-resonance distributions. Further, the first coefficient image in the compressed basis x_1 is shown, which is constructed by applying the low rank compression onto the reconstructed time frames in image space. The MRF T_1 maps appear noisier but the mean relaxation times in each compartment differed only 2 % on average with respect to the reference and a maximal deviation of 15 % was found. Good agreement in the ΔB_0 maps was found and the pixelwise mean absolute difference between MRF and the reference measurement was 2.7 Hz.

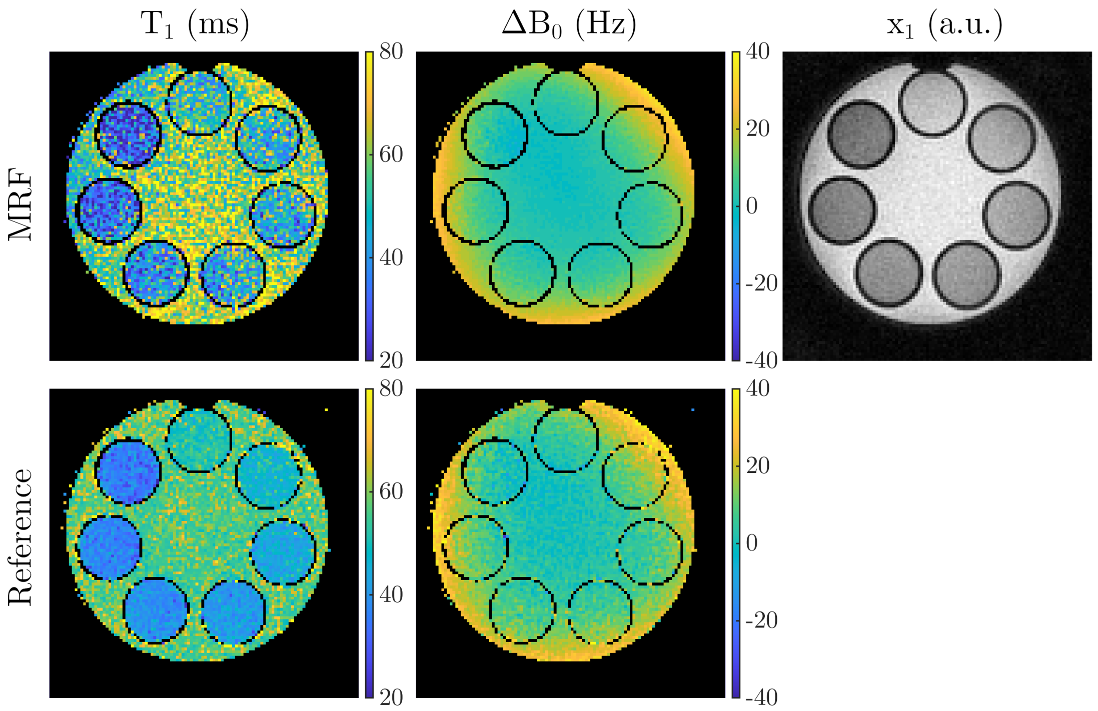

Figure 25: The relaxation times were acquired in a phantom, containing 0.9 % NaCl and various Agar concentrations ([0, 1, …, 7] %), with 2D MRF as well as reference methods. The resulting T_1 maps are shown, for which mean and SD in each compartment are summarized in the appendix, table 10. In the second column the ΔB_0 distributions are displayed. In the last column the first coefficient image in the compressed basis x_1 is shown. Image adapted from [40].

The measured T_{2l}^*, T_{2s}^* and T_2^* distributions are illustrated in figure 26. Here, the MRF framework determined biexponential relaxation in [18, 49, 73, 87, 89, 96, 98, 98] % of the voxels in the vials containing [0, 1, 2, 3, 4, 5, 6, 7] % Agar, whereas the reference method yielded [1, 39, 59, 85, 95, 98, 98, 97] %. In the vial containing 1 % Agar, the differentiation was unstable for both methods, suggesting that the bi- and the monoexponential relaxation model both describe the relaxation behavior similarly well. The T_{2l}^* values measured with MRF were overestimated by 15 % on average, whereas the short component was underestimated by 14 %. Mean and SD of all relaxation times in each compartment are illustrated in figure 27 and the corresponding numbers can be found in the appendix, table 10. Averaged over all quantified parameters, a mean deviation of 4.0 % between the results obtained with MRF and the reference results was found, whereas the mean absolute difference was 12.4 %.

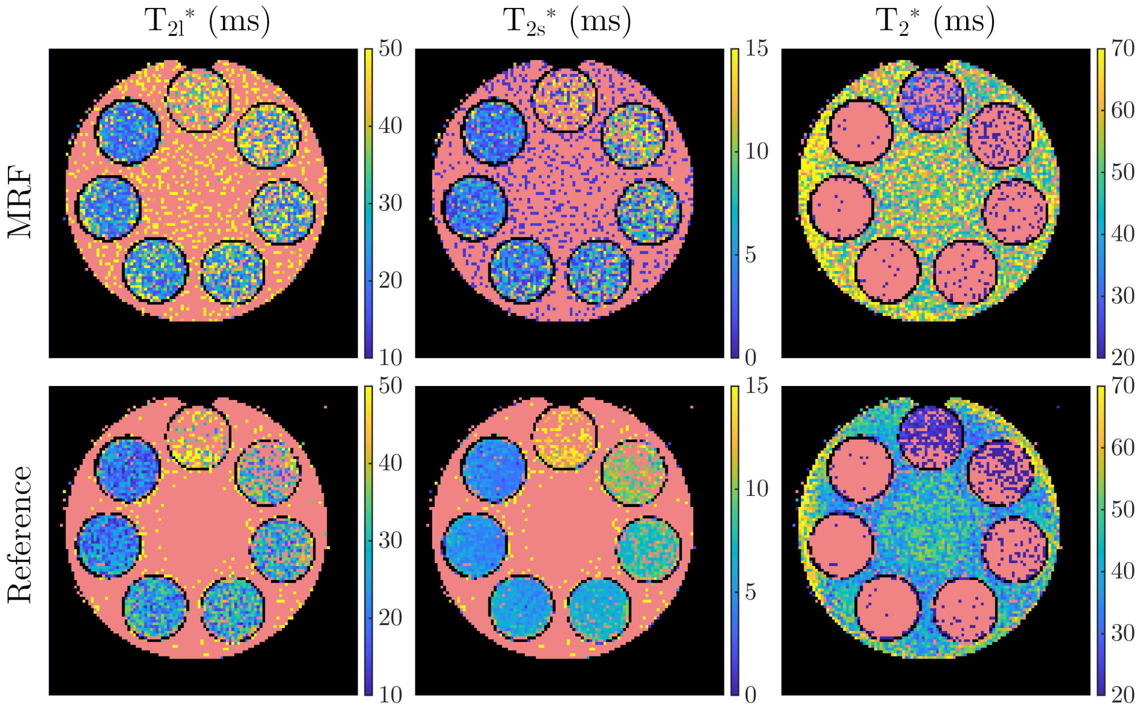

Figure 26: The transverse relaxation times are shown, acquired with 2D MRF and reference methods. Here, monoexponential voxels are masked in pink in the T_{2l}^* and T_{2s}^* maps, whereas biexponential voxels are masked in the T_2^* maps. Mean and SD of all compartments are summarized in the appendix, table 10. Image adapted from [40].

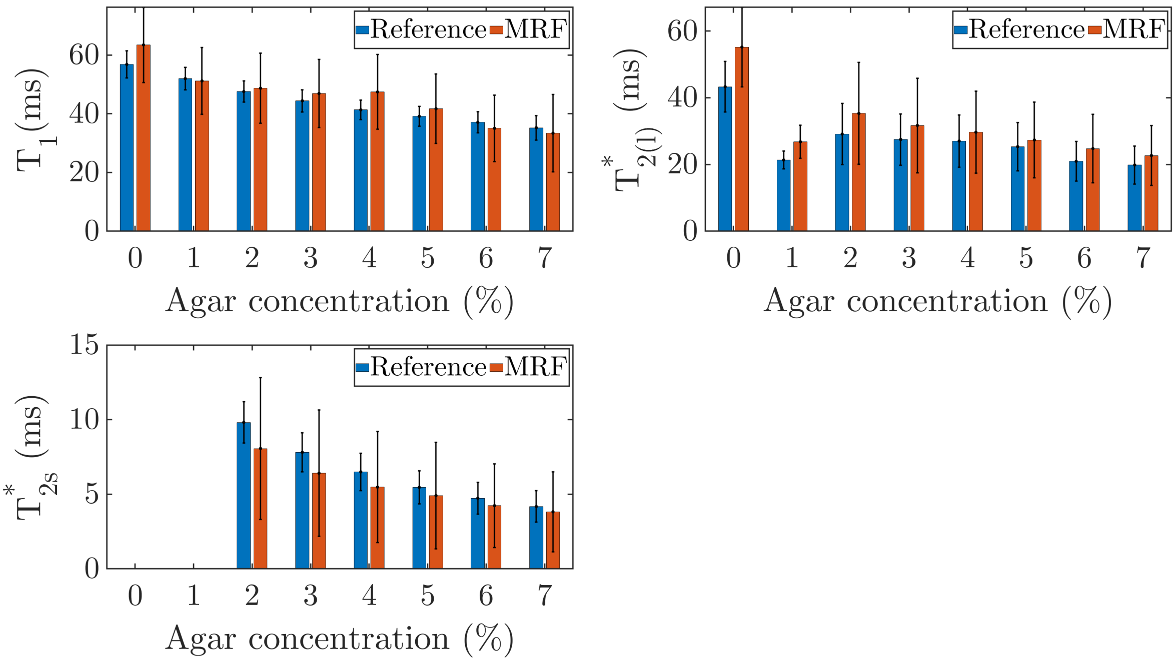

Figure 27: Mean and SD of all relaxation times in each phantom compartment are illustrated, measured with the reference methods and 2D MRF. All values are summarized in the appendix, table 10. Mind that the compartments with 0 % and 1 % Agar in the $T^*_{2(l)}$ subfigure decay with a monoexponential T^*_2, whereas the other compartments experience a biexponential relaxation and T^*_{2l} is shown. The average deviation between the MRF results and the references is 4.0 %.

4.1.3 In vivo studies

The relaxation parameters in BT and CSF were determined in an in vivo study, conducted in five healthy volunteers. Here, a nominal resolution of $4 \times 4\,\text{mm}^2$ was used and 7 spokes were acquired per time frame with 21-fold averaging, resulting in a measurement time of approximately 1 h. The resulting maps of an representative volunteer (volunteer 1) are illustrated in figure 28. In the first two images of the first row, the measured T_1 and ΔB_0 distributions are shown, whereas the second row displays T^*_{2l}, T^*_{2s} and T^*_2. Again, biexponential voxels are masked in pink in the monoexponential map and vice versa. The third image in the first row shows the first coefficient image in the compressed basis x_1 in conjunction with the ROIs, drawn in the co-registered ^{1}H images, which were used for quantitative analysis.

Mean and SD determined in BT and CSF of all relaxation parameters in each volunteer are summarized in table 5. In BT, the average T_1 values were in the range of (37.2 ± 9.4) ms–(43.3 ± 12.4) ms, where the mean was (38.9 ± 4.8) ms. The long and short transverse relaxation parameters were (29.2 ± 4.9) ms and (4.7 ± 1.2) ms on average, respectively. In CSF a mean T_1 of (67.1 ± 6.3) ms was found and the monoexponential transverse relaxation time was $T_2^* = (41.5 \pm 3.4)$ ms.

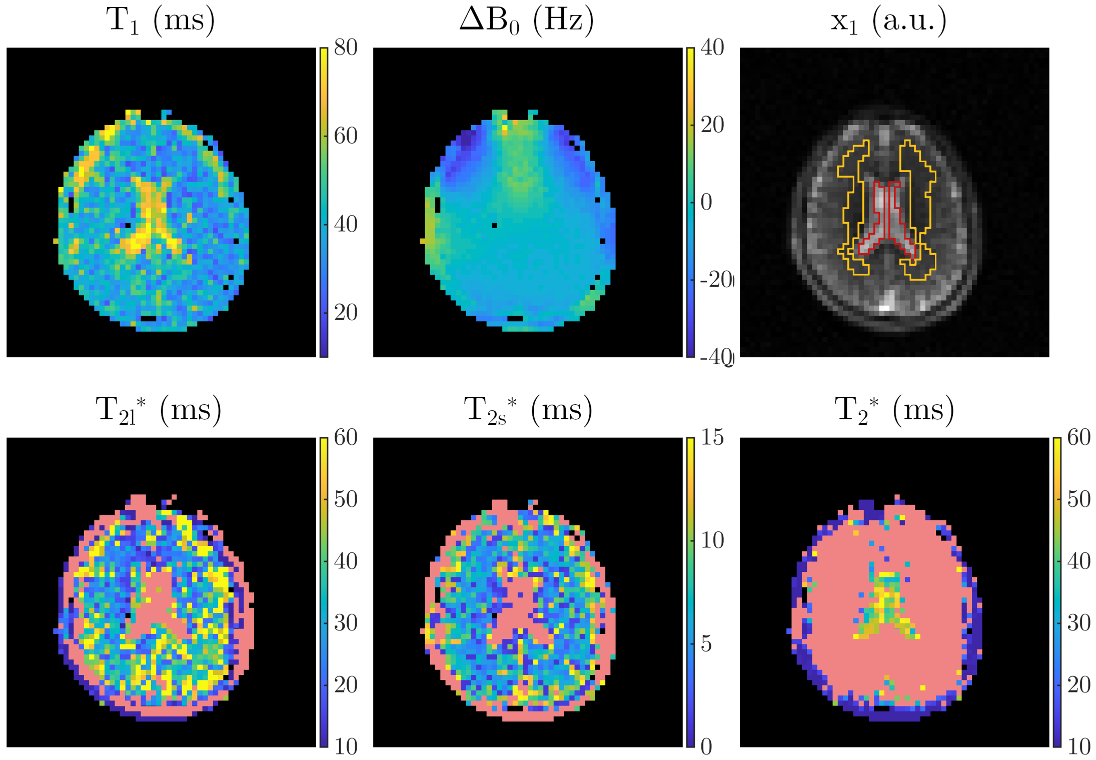

Figure 28: Relaxometric maps of an exemplary volunteer (volunteer 1) are illustrated, measured with the 2D MRF framework. Mean and SD of the relaxation times in the ROIs were calculated and are summarized in table 5 for all volunteers. Image adapted from [40].

Volunteer 1 was measured a second time with 147 spokes per time frame with a single average, resulting in the same scan duration as required for the measurement with 7 spokes and 21 averages. The resulting maps are shown in figure 29 and the quantified relaxation parameters are compared to the first measurement in table 6. The mean relaxation times were in good agreement and the maximal deviation was $-6.9\,\%$ in T_{2l}^*, which is well below the error of the individual measurements. However, decreased image quality was found in the 147 spokes measurement compared to the 7 spoke measurement and the SDs of all parameters were increased.

Table 5: Relaxometric mapping was performed in five healthy volunteers using 2D ^{23}Na MRF. Mean and SD of all relaxation times were evaluated in BT and CSF for each volunteer. Table adapted from [40].

	BT			CSF	
Volunteer	T_1 (ms)	T_{2l}^* (ms)	T_{2s}^* (ms)	T_1 (ms)	T_2^* (ms)
1	38.9 ± 10.2	28.8 ± 11.1	4.9 ± 2.5	69.1 ± 10.9	47.4 ± 6.6
2	37.2 ± 9.4	32.0 ± 11.3	4.6 ± 2.4	65.9 ± 15.5	43.7 ± 7.7
3	37.8 ± 10.6	25.1 ± 9.6	4.5 ± 2.8	63.1 ± 16.6	32.2 ± 7.6
4	43.3 ± 12.4	27.1 ± 11.2	4.4 ± 2.8	71.3 ± 15.2	40.6 ± 8.1
5	37.3 ± 10.4	30.9 ± 11.6	4.9 ± 3.2	65.9 ± 10.0	43.4 ± 7.9
mean	38.9 ± 4.8	29.2 ± 4.9	4.7 ± 1.2	67.1 ± 6.3	41.5 ± 3.4

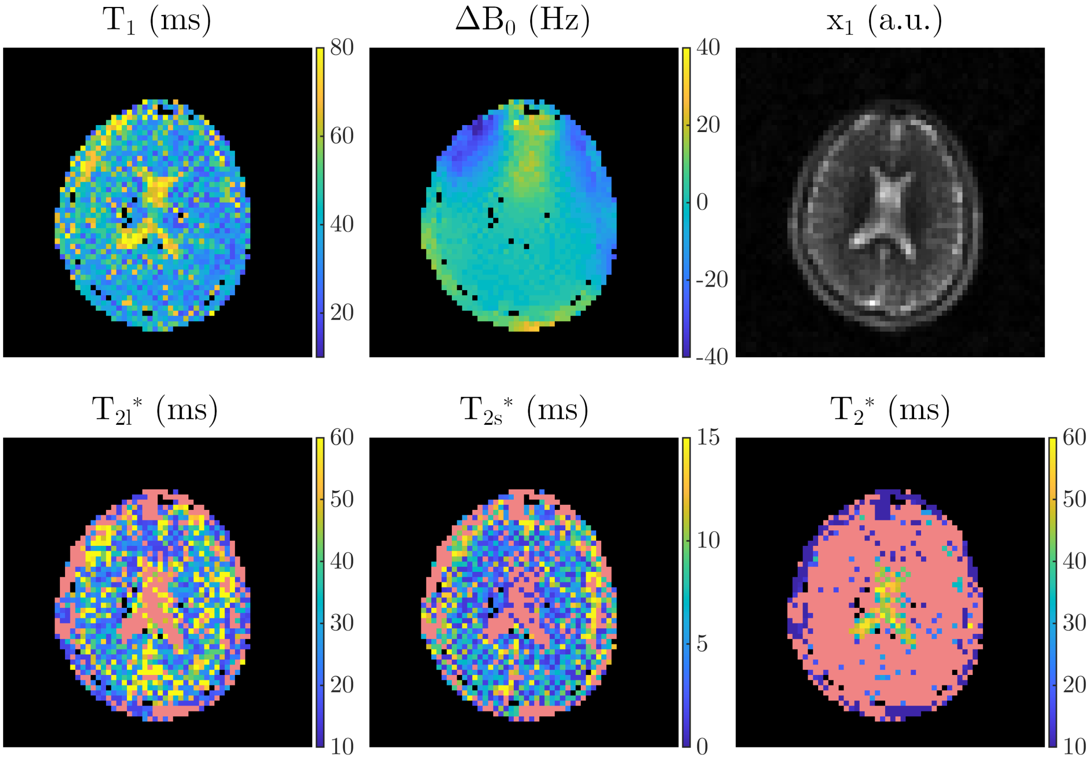

Figure 29: Volunteer 1 was measured a second time with 21-fold more spokes but a single average, leading to the same scan duration as in the first measurement. Similar relaxation times but increased noise and higher SDs in the quantified parameters are found, summarized in table 6. Image adapted from [40].

Table 6: Comparison of the quantified relaxation times acquired with 7 spokes per time frame using 21-fold averaging and 147 spokes per time frame with a single average [40].

	BT			CSF	
spokes/averages	T_1 (ms)	T^*_{2l} (ms)	T^*_{2s} (ms)	T_1 (ms)	T^*_2 ms
7/21	38.9 ± 10.2	28.8 ± 11.1	4.9 ± 2.5	69.1 ± 10.9	47.4 ± 6.6
147/1	38.8 ± 12.1	30.8 ± 14.2	4.7 ± 3.3	65.5 ± 11.9	48.1 ± 6.7

4.2 3D MRF

When the feasibility of ^{23}Na MRF was shown using the 2D MRF framework, two 3D MRF sequences were developed to improve the quantification efficiency. First, the 3D MRF I sequence was implemented as an extension of the 2D MRF sequence. Here, ISTO simulations were applied in the dictionary calculation, which allowed description of the full spin dynamics of spin 3/2 systems. Second, the MRF II sequence was developed, which uses a numerically optimized FA pattern and a hybrid of single- and double-echo readouts.
In the following, the 3D MRF results are presented, parts of which are published in [36].

4.2.1 Simulation experiments

Numerical simulations were used for FA pattern optimization to improve the T_1 encoding capability of the MRF II sequence. Further, the impact of PV effects on the quantified parameters was investigated and the smallest quantifiable image feature was estimated with respect to the nominal resolution. Finally, the influence of B_1 deviations on the quantified parameters was studied.

4.2.1.1 3D MRF FA pattern design

In the 3D ^{23}Na MRF sequences two different FA patterns were used. The MRF I sequence applies the same pattern as used in 2D MRF. For the MRF II sequence an FA pattern was optimized with the use of the CRLB [41, 42] as described in the following. Here, $\vec{s}(T_1, T_{2l}, T_{2s})$ denotes the normalized signal evolution of the described MRF II sequence for a given FA pattern and parameter set (T_1, T_{2l}, T_{2s}). Note that T_2-relaxation (not T_2^*) was assumed in the optimization to decrease the computational burden by simulating an on-resonant spin ensemble without the use of a Lorentzian off-resonance distribution. Further, finite differences were used to approximate the derivatives: $T_x^u = T_x(1 + \mathrm{d}T)$ and $T_x^l = T_x(1 - \mathrm{d}T)$, with $0 < \mathrm{d}T < 1$. Differentiation of the signal $\vec{s}$ along each parameter dimension yields:

$$y = \begin{pmatrix} \frac{\mathrm{d}}{\mathrm{d}T_1} \\ \frac{\mathrm{d}}{\mathrm{d}T_{2l}} \\ \frac{\mathrm{d}}{\mathrm{d}T_{2s}} \\ \frac{\mathrm{d}}{\mathrm{d}M_0} \end{pmatrix} \vec{s} = \begin{pmatrix} \frac{\vec{s}(T_1^u,\dots)-\vec{s}(T_1^l,\dots)}{T_1^u-T_1^l} \\ \frac{\vec{s}(T_{2l}^u,\dots)-\vec{s}(T_{2l}^l,\dots)}{T_{2l}^u-T_{2l}^l} \\ \frac{\vec{s}(T_{2s}^u,\dots)-\vec{s}(T_{2s}^l,\dots)}{T_{2s}^u-T_{2s}^l} \\ \vec{s} \end{pmatrix}, \tag{4.1}$$

from which the Fisher information matrix $F \in \mathbb{C}^{4\times 4}$ can be constructed:

$$F = yy^{\dagger}. \tag{4.2}$$

The FA pattern was then optimized by minimizing $\frac{\left(F^{-1}\right)_{11}}{T_1} \propto CRLB(T_1)$ using the GlobalSearch algorithm in MATLAB. Here, each FA was constrained to be between 20° and 91°.

To decrease the computational burden, the optimization was performed for one representative parameter set ($T_1 = 40\,\mathrm{ms}$, $T_{2l} = 30\,\mathrm{ms}$, $T_{2s} = 4.5\,\mathrm{ms}$, $\mathrm{d}T = 0.001$ and $\Delta B_0 = 0\,\mathrm{Hz}$) after conversion into spectral density parameters. Since the computational burden of the optimization increases exponentially with the number of FA entries, only 50 subsequent FAs were optimized, concatenated 20 times to obtain a pattern with 1000 entries. Note that a unique signal pattern over all cycles is achieved due to the changing TE and TR even though repeating the 50 pulses 20 times.

The resulting FA pattern is illustrated in section 3.3.3, figure 20. Here, rapid increases of the FA and subsequent exponential-like decreases were repeatedly found within the 50 FAs. These observations are similar to the findings in the construction of the 2D pattern, where toggling the FA was found to improve the parameter quantification.

A 2.08-fold reduction of the $CRLB(T_1)$ of the optimized pattern was found compared to the MRF I pattern for the optimization data set. Further, the $CRLB(T_1)$ of both patterns was calculated for 1000 random parameter combinations in $T_1 = [20, 21, \ldots, 70]\,\mathrm{ms}$, $T_{2l} = [15, 16, \ldots, 50]\,\mathrm{ms}$ and $T_{2s} = [1.0, 1.3, \ldots, 14.8]\,\mathrm{ms}$. Here, on average a 1.72-fold $CRLB(T_1)$ reduction was found, whereas the maximum and the minimal reduction factors were 3.13 and 1.26. These findings indicate, that the T_1 encoding was improved over the entire parameter space and not only for the optimization data set. This was confirmed in the phantom measurements where the quantification in all compartments was improved, as illustrated in section 4.2.2.

Correlation plots for the 3D sequence with both the optimized and the 2D pattern, were constructed (see figure 30) through the T_1-T_{2l}, the T_1-T_{2s} and the T_{2l}-T_{2s} plane, where the central parameters were $T_1 = 40\,\mathrm{ms}$, $T_{2l} = 30\,\mathrm{ms}$ and $T_{2s} = 4.6\,\mathrm{ms}$ ($J_0 = 193.8\,\mathrm{Hz}$, $J_1 = 23.6\,\mathrm{Hz}$, $J_2 = 9.7\,\mathrm{Hz}$). Parameter combinations violating $J_0 \geq J_1 \geq J_2 > 0$ were neglected in this process and are masked in pink. For all cases, the correlations were narrowed for the optimized pattern compared to the initial one, also implying improved parameter distinguishability.

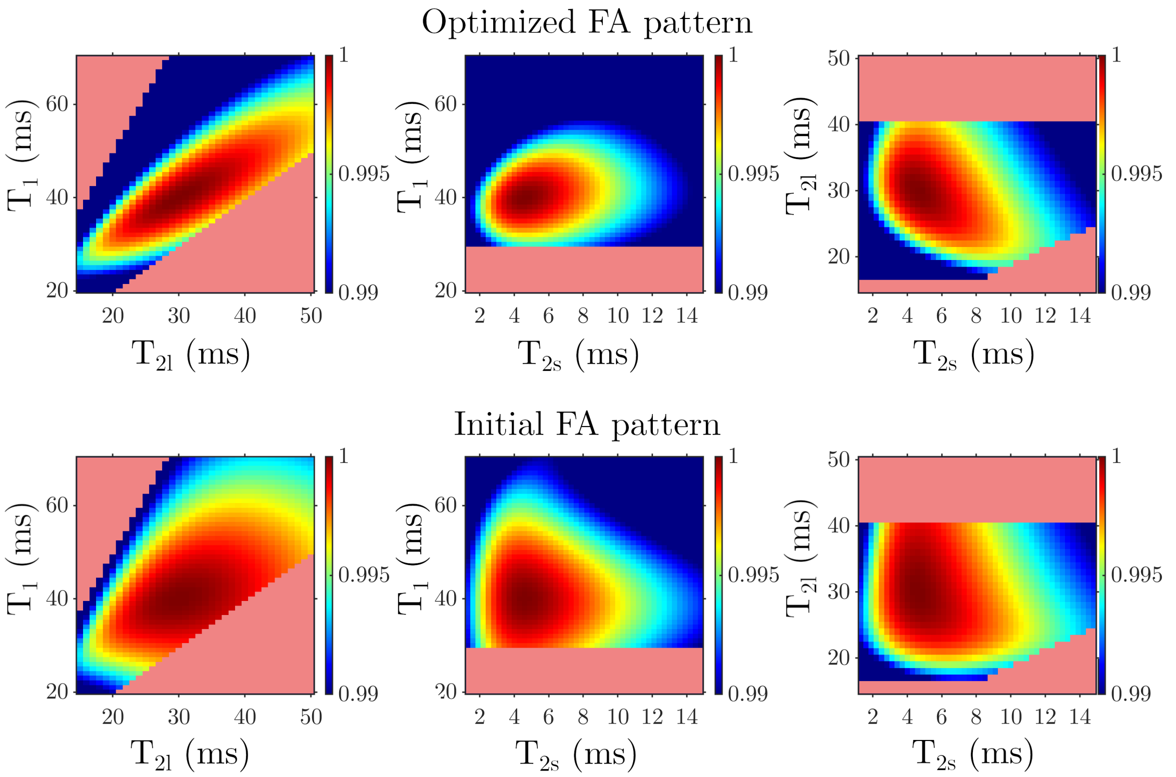

Figure 30: The auto-correlations in three orthogonal slices were calculated through the point $T_1 = 40\,\mathrm{ms}$, $T_{2l} = 30\,\mathrm{ms}$ and $T_{2s} = 4.6\,\mathrm{ms}$ ($J_0 = 193.8\,\mathrm{Hz}$, $J_1 = 23.6\,\mathrm{Hz}$, $J_2 = 9.7\,\mathrm{Hz}$). Here, values that violate $J_0 \geq J_1 \geq J_2 > 0$ are masked in pink. The optimized FA pattern shows a narrower distribution in all correlation planes, indicating improved parameter distinguishability.

4.2.1.2 PV effects on the quantified relaxation parameters

If a voxel is composed of a mixture of different tissue types, the signal evolution cannot be described well by the single-compartment model, which can yield a parameter bias. To estimate this bias at the example of a BT-CSF interface, a set of two-compartment signal evolutions was constructed by combining the simulated signal evolutions of BT ($T_1 = 40\,\mathrm{ms}$, $T_{2l} = 35\,\mathrm{ms}$, $T_{2s} = 4.9\,\mathrm{ms}$, $T_{2l}^* = 30\,\mathrm{ms}$, $T_{2s}^* = 4.8\,\mathrm{ms}$) and CSF ($T_1 = T_2 = 60\,\mathrm{ms}$, $T_2^* = 50\,\mathrm{ms}$) with weighting factors between 0 % and 100 %. Subsequently, each mixed fingerprint in the set was matched to the dictionary to extract the relaxation parameters. This allowed investigation of the parameter bias and which ratio results in bi- and which in monoexponential classification. The quantified parameters after dictionary matching are illustrated in figure 31 in conjunction with the fraction-weighted sum of the input parameters.

Even though this weighted sum is the best estimate, it does not pose a ground truth and consequently a numerical comparison between it and the matched parameters is waived.

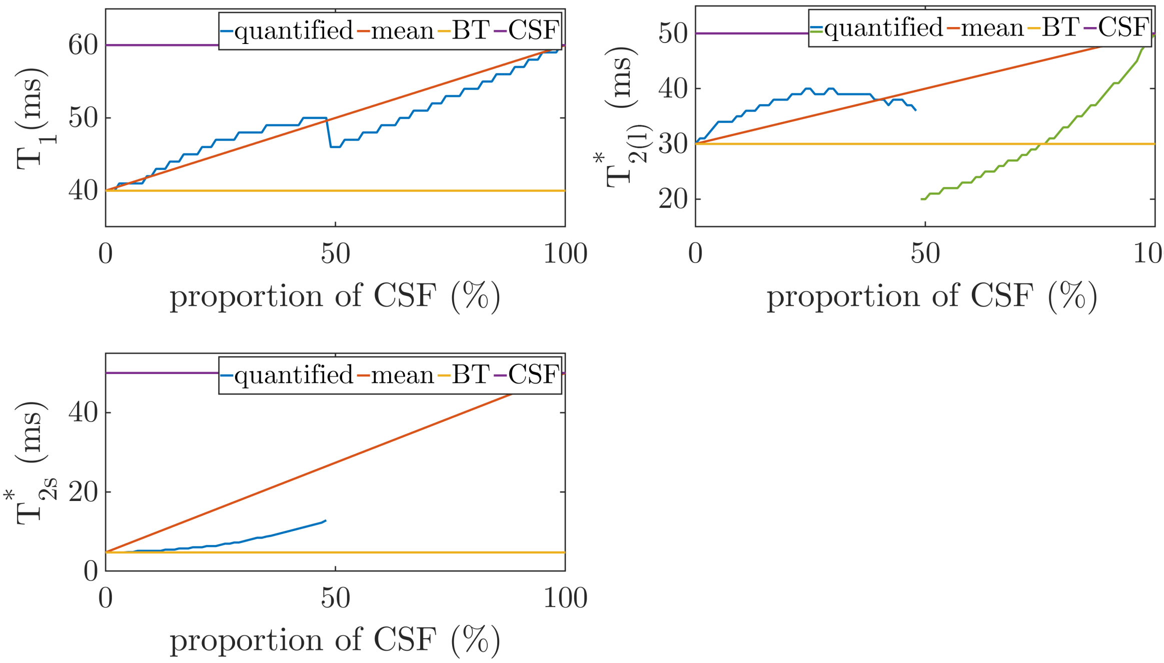

Figure 31: Partial volume effects were investigated by matching the combined signal of variable CSF and BT ratios to the dictionary. For a CSF content of 0 %–48 %, biexponential relaxation behavior was found, whereas 49 % and above resulted in monoexponential classification. Especially strong deviations were found in T_{2l}^* for a CSF to BT ratio of approximately 1:1, since here effectively triexponential relaxation is present, which is not represented in the dictionary.

The quantified T_1 curve behaves approximately linearly with respect to the tissue fraction, similar to the weighted sum. Only a small jump is observed at the point where the detected biexponential transverse relaxation switches to a monoexponential relaxation. A biexponential transverse relaxation was found for a CSF content of 0 %–48 %, whereas a monoexponential relaxation was found for a CSF proportion of 49 % and higher. In the monoexponential T_2^* curve, a relaxation time below both input parameters is found at the point where the transition from bi- to monoexponential relaxation is detected. These effects can be explained since the mixing of the compartments results in a triexponential relaxation, which is not represented in the dictionary. However, in conventional FID fitting similar problems are expected since here the model also does not describe the data well.

4.2.1.3 Simulations on the resolution

Two main effects can lead to the PV bias, described in the previous section: First, the voxel size can be larger than the anatomical structures, resulting in a tissue mixture in each voxel. Second, signal bleeding due to the PSF can cause a mixed signal in the voxels even if the nominal resolution is similar to the image features.

In MR imaging the nominal resolution is determined by the most peripheral point acquired in k-space (see section 2.5.3). The real resolution, however, is lower since the PSF, which describes the response of an imaging system to a point source, is no Dirac delta function. This results in smearing of the signal from neighboring voxels and therefore causes PV effects. The shape of the PSF mainly depends on the k-space sampling scheme but also on effects like relaxation during data acquisition, reconstruction and data filtering. Hence, knowledge on the PSF is of high interest to estimate the minimal object size that can be imaged with a given sequence. For sampling schemes that fulfill the Nyquist criterion, the PSF can be simulated straightforwardly and the real resolution can be estimated by the width of the PSF. However, the heavy undersampling of each time frame, the low rank compression and the non-linear reconstruction make this approach unpractical for MRF. Consequently, simulations of the imaging process were applied to estimate the real resolution, as this approach inherently covers most of these issues. However, note that the choice of the phantom also impacts the achievable resolution.

A numerical resolution phantom was constructed, consisting of a cylinder with 190 mm diameter. Here, a ^{23}Na concentration of 40 mmol/L and relaxation times of $T_1 = 40\,\text{ms}$, $T_{2l}^* = 30\,\text{ms}$ ($T_{2l} = 35\,\text{ms}$) and $T_{2s}^* = 4.8\,\text{ms}$ ($T_{2s} = 4.9\,\text{ms}$) were assumed to imitate BT. Eight cylinders with diameters of [3, 5, 8, 10, 20, 30, 40, 50] mm were incorporated, as illustrated in figure 32. Their ^{23}Na concentration was assumed to be 150 mmol/L and the relaxation times were $T_1 = 60\,\text{ms}$ and $T_2^* = 50\,\text{ms}$ ($T_2 = 60\,\text{ms}$) to mimic CSF.

An analytical k-space was determined for both compartments individually in each MRF time frame with the Fourier domain method proposed by Koay et al. [46]. Next, each time frame was weighted with the theoretical signal evolution, obtained using the ISTO simulation. Furthermore, transverse relaxation during data acquisition was incorporated by weighting each spoke in k-space with an exponential decay. Combination of the two compartments yielded a single set of time frames in k-space, which was subsequently reconstructed similar to the MRF measurements. These simulations were conducted for the nominal resolutions of $(3\,\text{mm})^3$ and $(5\,\text{mm})^3$ with both 150 and 50 spokes per time frame. To estimate the real resolution, line profiles were determined along three straights

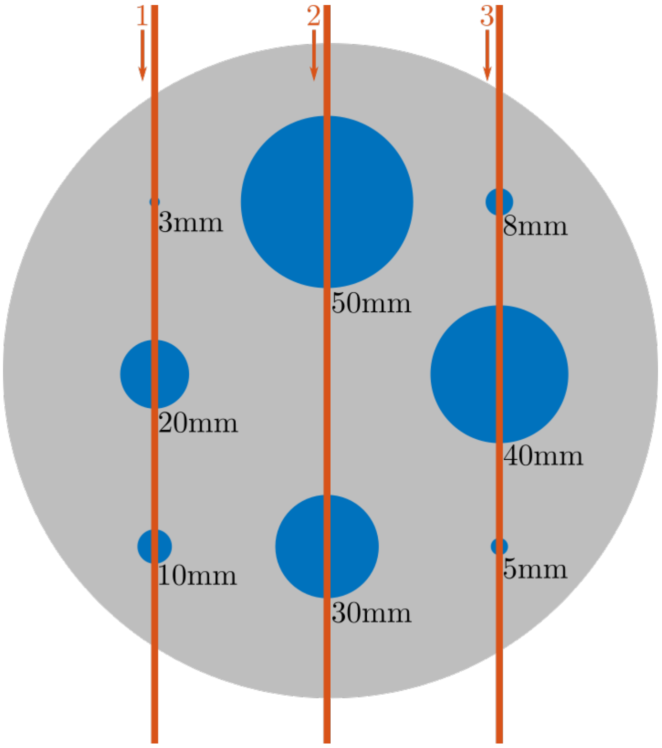

Figure 32: The phantom used for resolution simulations is illustrated. It is cylindrically shaped and the relaxation times mimic BT ($T_1 = 40\,\mathrm{ms}$, $T_{2l} = 35\,\mathrm{ms}$, $T_{2s} = 4.9\,\mathrm{ms}$, $T_{2l}^* = 30\,\mathrm{ms}$, $T_{2s}^* = 4.8\,\mathrm{ms}$). Eight CSF-like ($T_1 = T_2 = 60\,\mathrm{ms}$, $T_2^* = 50\,\mathrm{ms}$) vials are inserted, whose diameter range from 3 mm to 50 mm. In the resulting relaxometric maps, the parameter distributions along the red lines were evaluated in the direction of the arrows to estimate the real resolution of the MRF II sequence.

in the reconstructed parameter maps, as illustrated in figure 32.

The plots along the central line are illustrated in figure 33 for a nominal resolution of $(3\,\mathrm{mm})^3$, whereas the other lines are shown in the appendix, figures 44 and 45.

Good differentiation between bi- and monoexponential relaxation was found in all cases, which is in agreement to the findings in section 4.2.1.2. For the 150 spokes, the line plots indicate that the relaxation parameters in liquor structures with a size of approximately 10 mm can be quantified for the $(3\,\mathrm{mm})^3$ resolution, since this allows eroding one pixel at each side of the BT-CSF interface. The highest parameter bias at compartment borders was found in T_{2s}^* and at the center of the compartments in T_{2l}^*. The 50 spoke simulations showed stronger deviations, especially in T_{2l}^* and T_{2s}^*, where differences up to 56.7 % in the compartment center compared to the ground truth were found.

The simulations with a resolution of $(5\,\mathrm{mm})^3$ yielded similar results, which are shown in appendix 7.5.1.

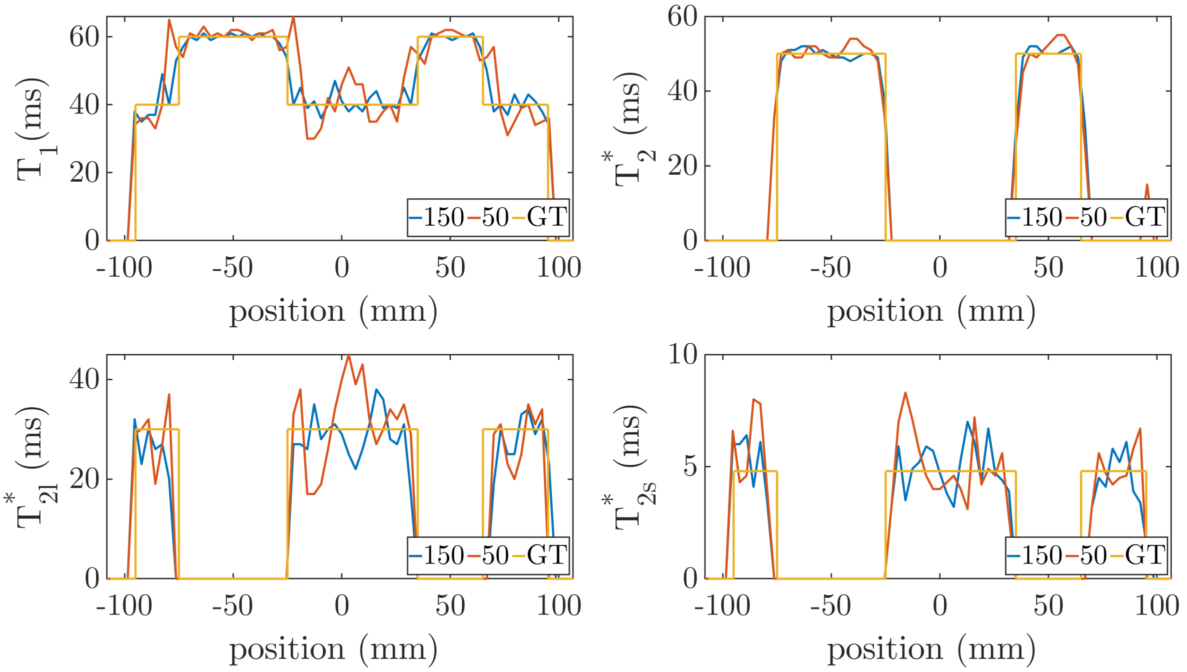

Figure 33: Line plots (150 spokes, 50 spokes and the ground truth) through the quantified parameters along the second line are shown, intersecting the liquid-filled vials with diameters of 50 mm and 30 mm.

4.2.1.4 Simulations on the influence of B_1 deviations

In this work, a uniform B_1 distribution was assumed in all measurements. However, any B_1 inhomogenieties linearly transfer into deviations in the actual FA, which can result in parameter bias.

To estimate the order of magnitude of this effect, the signal evolutions for BT ($T_1 = 40\,\text{ms}$, $T_{2l} = 35\,\text{ms}$, $T_{2s} = 4.9\,\text{ms}$, $T^*_{2l} = 30\,\text{ms}$, $T^*_{2s} = 4.8\,\text{ms}$) and CSF ($T_1 = T_2 = 60\,\text{ms}$, $T^*_2 = 50\,\text{ms}$) were simulated for a relative B_1 range of 0.8 to 1.2 and subsequently matched to the dictionary. The resulting relaxation parameters are illustrated in figure 34. In the realistic relative B_1 range of 0.87 to 1.095, the maximal relative deviation was 15.0 %, found in T_1 of BT. In T_1 an approximately linear slope $\frac{\mathrm{d}T_1}{\mathrm{d}B_1}$ was observed, which was about -0.18 in CSF and 1.22 in BT. This B_1 range was estimated from measurements in the human head, conducted in a healthy volunteer. Here, the maps were acquired with the phase sensitive method (FA = 90°, TE = 0.55 ms, TR = 190 ms, $(3\,\text{mm})^3$, TA

= 24 min) and subsequently masked by thresholding of the image data. Next, the B_1 data was plotted in a histogram, shown at the right of figure 34. The bins with 1/10th the count of the highest bin count were determined to yield a realistic B_1 range, which resulted in the borders of 0.870 and 1.095. In this area, 87.6 % of the B_1 values are represented and the remaining 12.4 % values are mostly found in peripheral head areas like the nose and ears (not shown), where a poor quantification is expected.

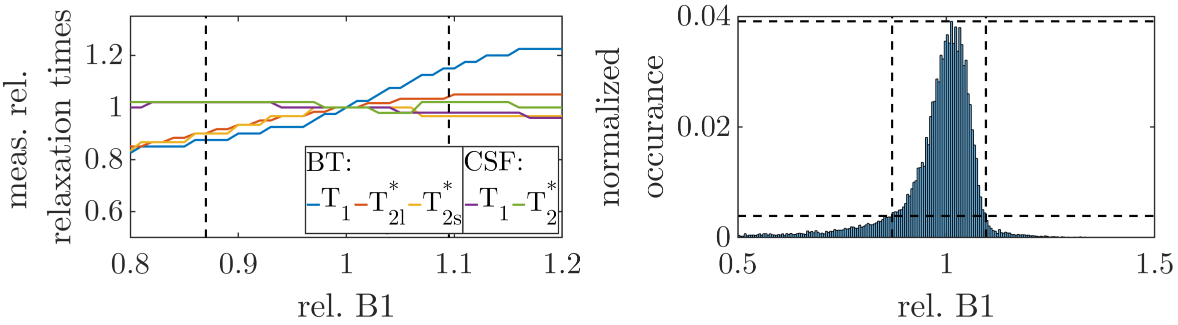

Figure 34: The impact of B_1 deviations on the quantified parameters in BT and CSF was simulated, shown in the left subfigure. Here the dashed lines correspond to a relative B_1 of 0.870 and 1.095. These limits were extracted by finding the values for which the B_1 distribution, illustrated in the right, was below 10 % of the maximum of the measured B_1 distribution in a human head. The specified interval contained 87.6 % of all measured B_1 vaules.

4.2.2 Phantom measurements

Phantom studies were used to compare the relaxation parameters quantified using the reference methods with the ones determined with both 3D MRF sequences. The phantom has a ^{23}Na concentration of 0.9 % (154 mmol/L) and six vials with additional Agar concentration in the range of 2 %–7 %. All measurements had a nominal resolution of $(3\,\text{mm})^3$ and the sequence parameters are summarized in the methods section 3.7.2, table 3.

The central slice of all T_1 maps is shown in figure 35 in conjunction with the off-resonance distributions ΔB_0. The T_1 map acquired with MRF I shows increased values in the liquid compartment compared to the reference map, whereas the results of the MRF II measurement are in good agreement with the reference. Further, good accordance between all ΔB_0 maps is visible.

In figure 36 the transverse relaxation maps are shown. Note that monoexponential

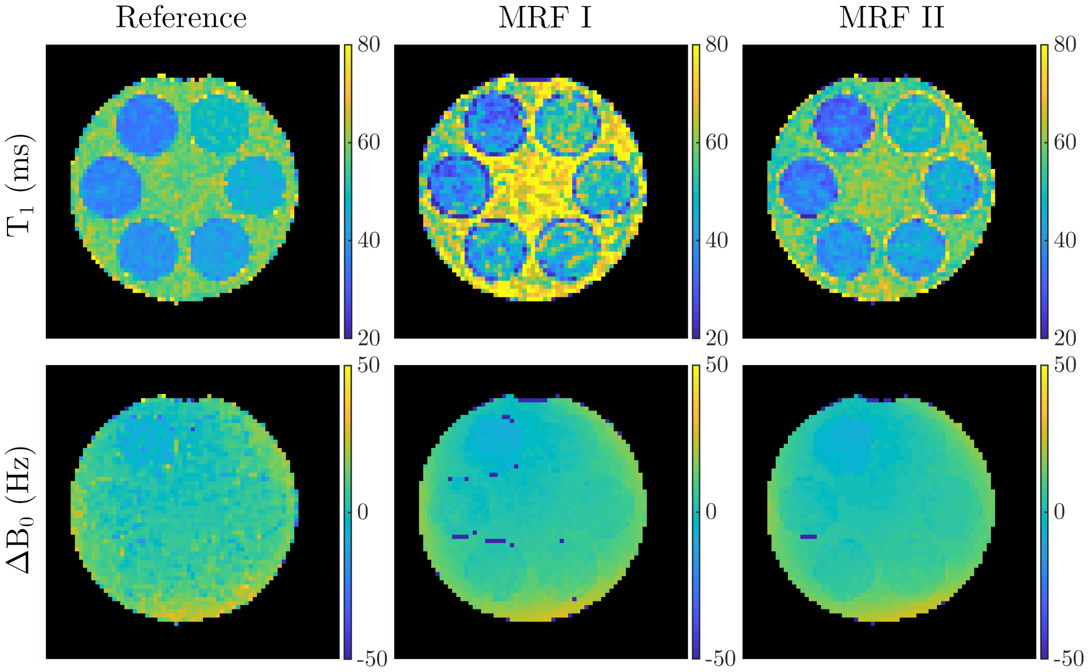

Figure 35: The central slice of the T_1 and the ΔB_0 maps are compared, acquired with the reference methods, MRF I and MRF II. The T_1 encoding is strongly improved in MRF II compared to MRF I due to the optimized FA pattern. Mean and SD of T_1 for all phantom compartments are illustrated in figure 37 and summarized in the appendix, table 11. Good agreement between all ΔB_0 maps is found. Image adapted from [36].

areas are masked in pink in the T_{2l}^* and T_{2s}^* maps, whereas biexponential relaxation is masked in the T_2^* maps. Differentiation of the relaxation type was based on the goodness of the fit R^2 for the reference method and was automatically determined in the dictionary matching step for the MRF sequences. Good differentiation between bi- and monoexponential relaxation was found in all cases. Difference images between the maps acquired with MRF and the reference are shown in the appendix, figures 49 and 50.
Mean and SD of all relaxation times in each compartment, evaluated over the ten central slices, are illustrated in figure 37 and summarized in the appendix, table 11. Both the mean deviation and the mean absolute deviation of MRF I with respect to the references were 10.8 %. MRF II, on the other hand, deviated by 1.0 % on average and the mean absolute deviation was 4.6 %.

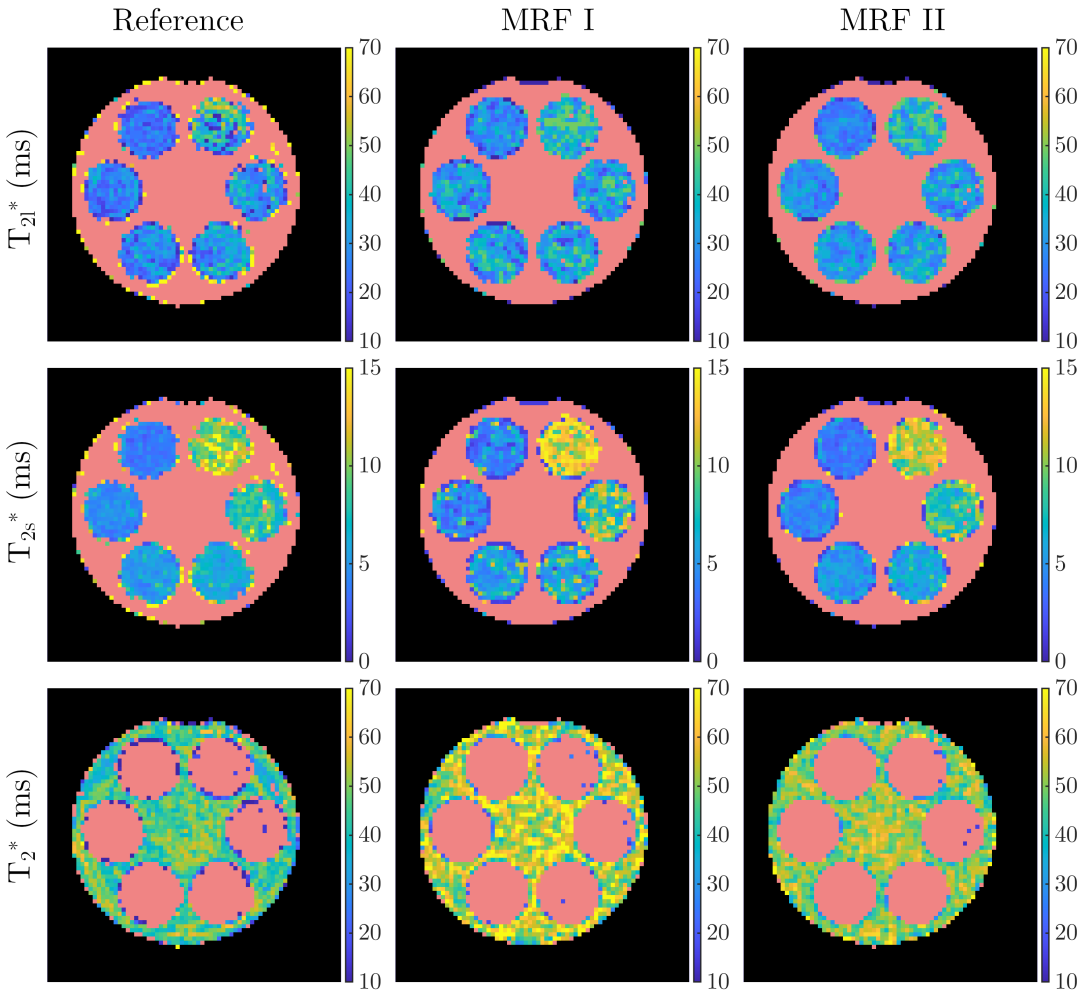

Figure 36: Comparison of the quantified transverse relaxation times in the central phantom slice. In the T_{2l}^* and T_{2s}^* maps, monoexponentially relaxing voxels are masked in pink, whereas in the T_2^* maps biexponential areas are masked, respectively. Mean and SD of all compartments are summarized in figure 37 and in the appendix, table 11. Image adapted from [36].

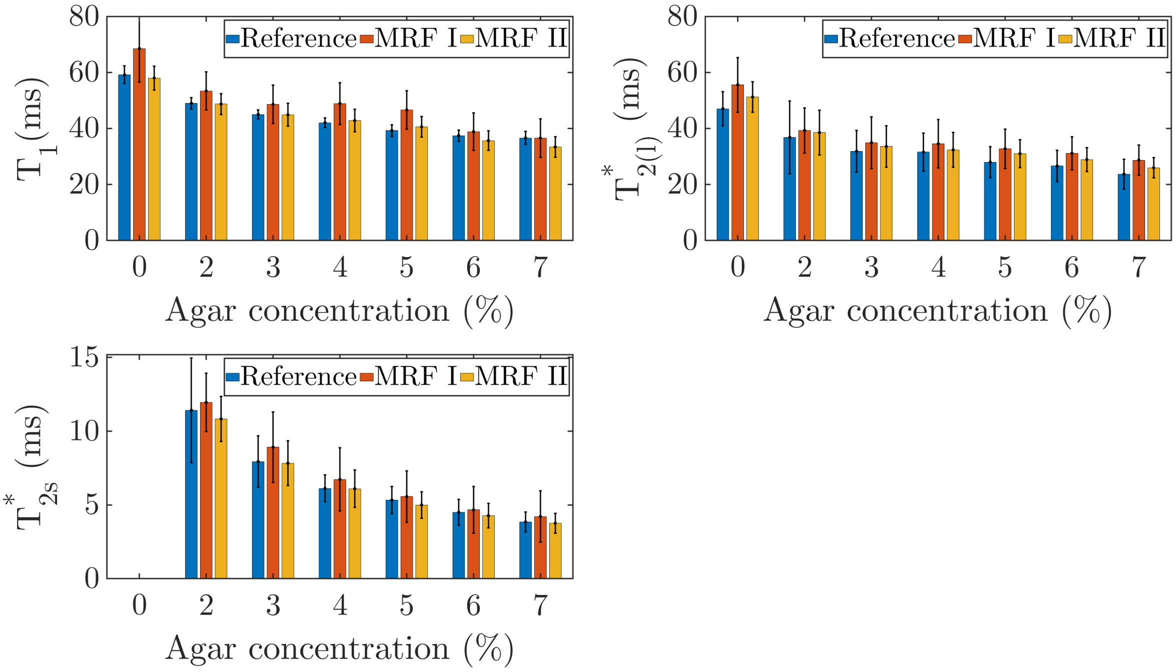

Figure 37: Mean and SD are illustrated for all relaxation parameters in each phantom compartment, evaluated over the ten central slices. Mind that in the $T^*_{2(l)}$ subplot T^*_2 is shown for the compartment with 0 % Agar, whereas the compartments with Agar concentrations of 2 %–7 % show T^*_{2l}. The mean deviation between the results acquired with reference methods and with MRF I is 10.8 %, whereas MRF II only differed by 1.0 % on average. Image adapted from [36].

Further, the impact of reduced measurement time was investigated by reconstructing only subsets of the measured data. The corresponding reconstructed data is shown in figure 38 for virtual measurement times of [2.6, 7.3, 11, 16, 21, 32, 64] min, where 64 min corresponds to the full data set. For the 2.6 min measurement, a significant loss of the spatial information is found and the differentiation between bi- and monoexponential relaxation is perturbed. However, the relaxation times only differ by 3.2 % on average compared to the full data set. The maximal deviation was found in the liquid compartment, where T^*_2 was reduced by 14.4 % from (51.2 ± 5.4) ms to (43.8 ± 10.8) ms. A virtual measurement time of 21 min appeared to be a good compromise between scan duration and image quality as here only minor alterations of the spatial information were found and the average deviation in the relaxation parameters was -1.1 %. The maximal deviation was a -3.1 % change of T^*_{2l} in the compartment containing 7 % Agar.

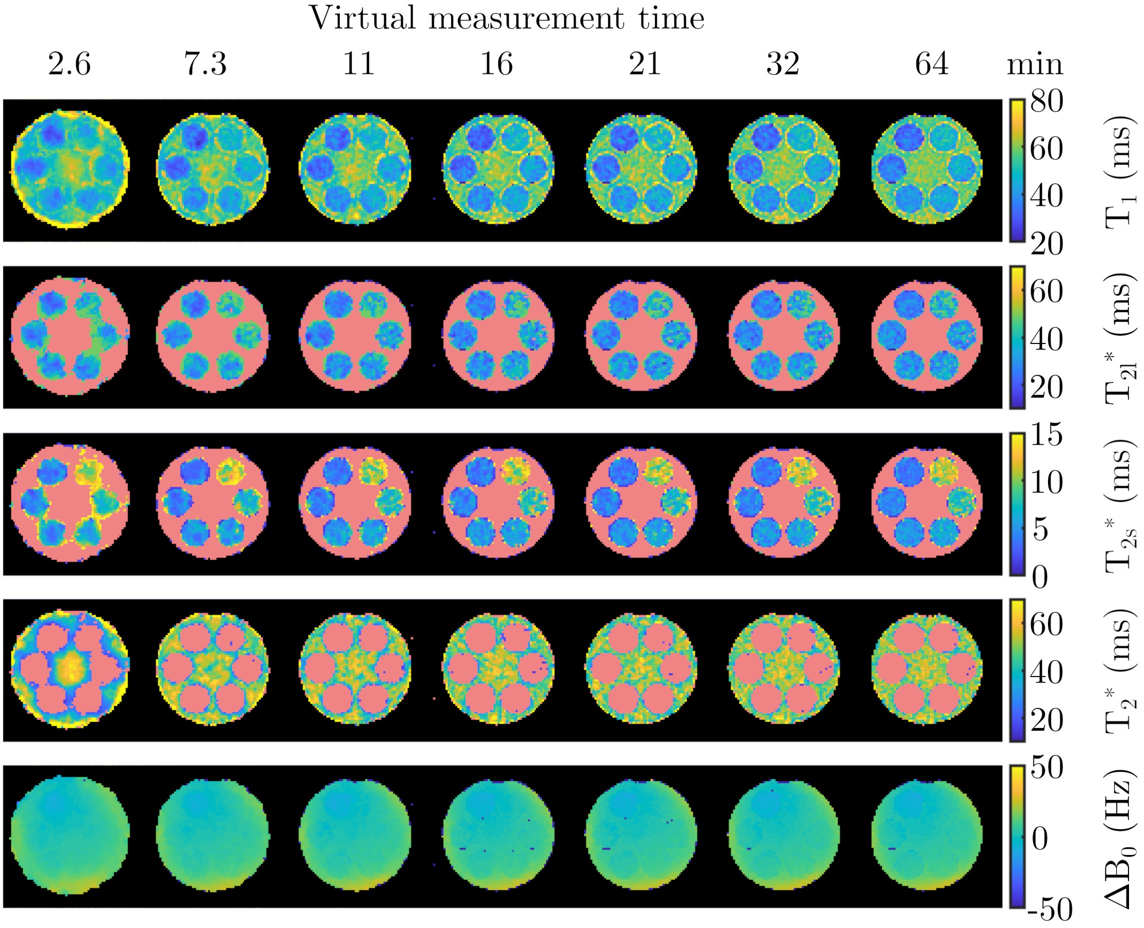

Figure 38: Subsets of the measured phantom data were reconstructed to investigate the impact of reduced measurement time on the quantitative maps. The spatial structure is highly affected for the short scan durations and a maximal parameter deviation of 14.4 % with respect to the full data set was found in the liquid-filled compartment. However, the virtual measurement of 21 min yielded a good compromise between image quality and scan duration. Image adapted from [36].

4.2.3 In vivo studies

An in vivo study was conducted in four healthy volunteers using the MRF II framework. The nominal resolution was $(3\,\mathrm{mm})^3$ and the measurement duration was 64 min. Mean and SD of all relaxation times were determined in ROIs in BT and CSF, evaluated over the seven central slices, and are summarized in table 7. In BT, an average T_1 of (35.0 ± 3.2) ms was found, whereas the mean transverse relaxation times were $T^*_{2l} = (29.3 \pm 3.8)$ ms and $T^*_{2s} = (5.5 \pm 1.3)$ ms. In CSF $T_1 = (61.9 \pm 2.8)$ ms and $T^*_2 = (46.3 \pm 4.5)$ ms were found.

The relaxometric maps in six equidistant slices of a representative volunteer (volunteer 1) are shown in figure 39. The upper row shows the first coefficient in the compressed basis. The second row corresponds to the T_1 maps, where good distinction between CSF and BT is achieved. In the T^*_{2l} and T^*_{2s} maps monoexponential voxels are masked in pink, which is found in areas dominated by CSF. Erroneous T^*_{2l} quantification is found in areas with high off-resonances, i.e. in the frontal lobe and near the ear canals.

Table 7: Relaxometric mapping was performed in four healthy volunteers using MRF II. Mean and SD of all relaxation times were evaluated in 7 slices in each volunteer [36].

	BT			CSF	
Volunteer	T_1 (ms)	T^*_{2l} (ms)	T^*_{2s} (ms)	T_1 (ms)	T^*_2 ms
1	35.3 ± 6.2	29.9 ± 7.9	5.6 ± 2.6	64.2 ± 5.1	50.9 ± 8.4
2	34.6 ± 5.6	29.0 ± 6.9	5.4 ± 2.4	60.6 ± 6.0	44.4 ± 9.6
3	35.0 ± 6.6	29.1 ± 7.8	5.2 ± 2.4	60.3 ± 6.2	39.0 ± 7.4
4	35.0 ± 6.8	29.0 ± 8.0	5.7 ± 2.8	62.8 ± 5.0	50.9 ± 10.3
mean	35.0 ± 3.2	29.3 ± 3.8	5.5 ± 1.3	61.9 ± 2.8	46.3 ± 4.5

Retrospective undersampling was performed to investigate the impact of reduced measurement time on the quantified parameters. Resulting maps (of volunteer 2) for virtual scan durations of [6.4, 11, 21, 32, 64] min are shown in figure 40, where 64 min corresponds to the full data set. The quantified relaxation parameters in CSF and BT are displayed in each image. In the 6.4 min measurement, the loss of spatial information resulted in poor distinguishability between CSF and BT in the T_1 map. A good compromise between image quality and scan duration appears to be the 32 min measurement. Here, all parameters deviated by less than 4 % compared to the full data set.

This was confirmed by measuring volunteer 4 a second time with reduced number of

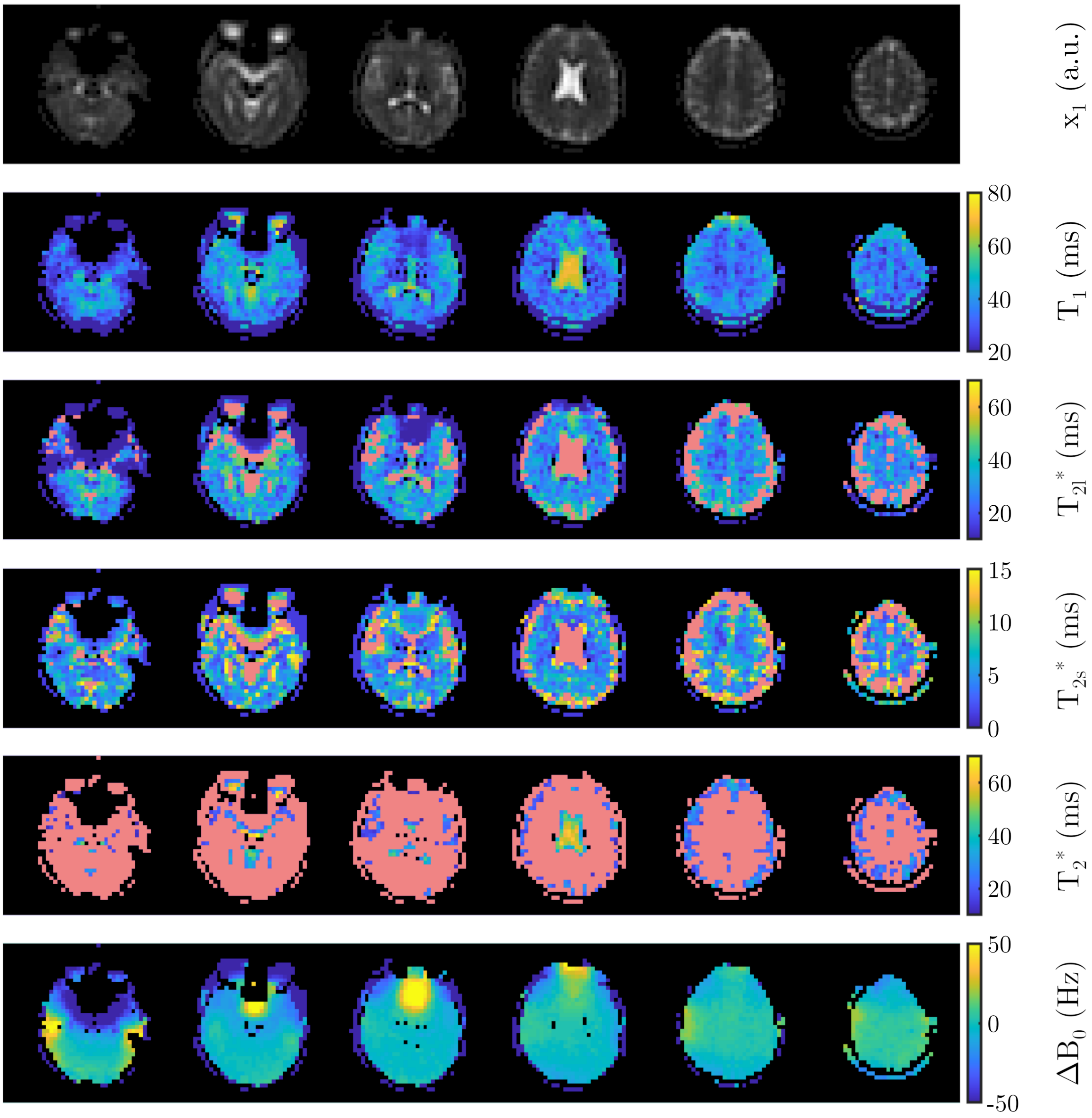

Figure 39: Six equidistant slices of the in vivo data of an exemplary volunteer are shown, acquired with MRF II within 64 min with a nominal resolution of (5 mm)^3. At the top, the first coefficient image in the compressed basis is shown, followed by the relaxation maps and the off-resonance distribution. In the T_{2l}^* and T_{2s}^* maps, pink areas correspond to areas where monoexponential relaxation was found. In the T_2^* maps, biexponential relaxation is masked, respectively. Image adapted from [36].

spokes to yield a measurement time of 32 min. The quantified parameters of the 32 min measurement, the retrospective reduced measurement (1/2×64 min) and the full data set (64 min) are summarized in table 8. Good agreement between them is found as the maximal deviation was less than 5.0 %, which is well below each SD, with respect to the 64 min measurement. Images of the reduced measurement times are shown in the appendix in figure 51.

Table 8: The relaxation parameters, determined (A) in a 32 min measurement and (B) by retrospective undersampling of a 64 min data set are compared to the results of the full data set.

	BT			CSF	
Measurement	T_1 (ms)	T_{2l}^* (ms)	T_{2s}^* (ms)	T_1 (ms)	T_2^* ms
A: 32 min	35.1 ± 7.7	28.3 ± 8.4	5.8 ± 3.2	60.7 ± 5.3	49.9 ± 9.3
B: 1/2× 64 min	34.9 ± 7.7	28.0 ± 8.4	5.9 ± 3.1	60.9 ± 6.1	48.4 ± 10.5
C: 64 min	35.0 ± 6.8	29.0 ± 8.0	5.7 ± 2.8	62.8 ± 5.0	50.9 ± 10.3

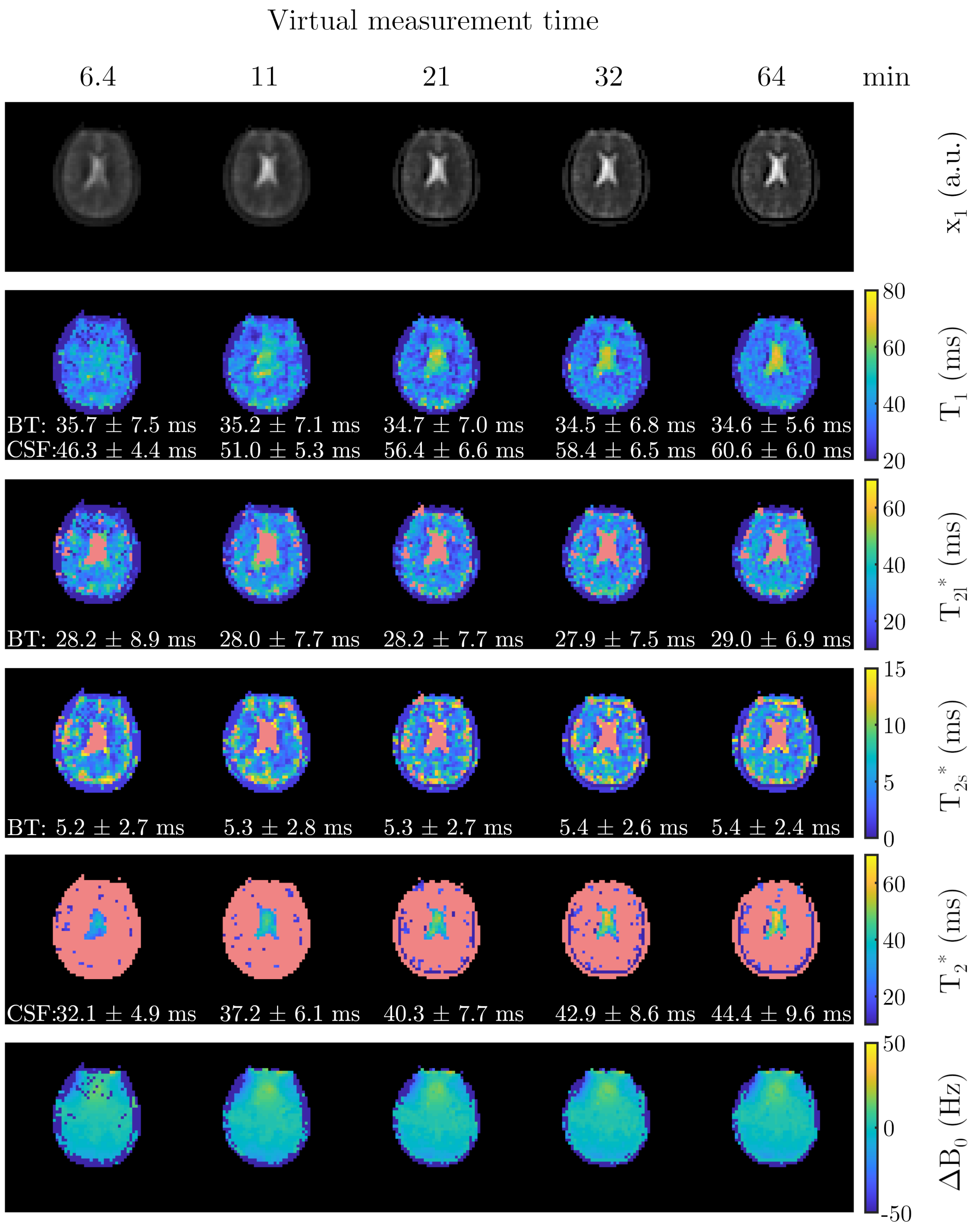

Figure 40: Parts of the data acquired in volunteer 2 were retrospectively discarded to investigate the effect of reduced measurement time on the quantified parameters. The virtual scan duration of 32 min showed a good compromise between image quality and scan duration. This was confirmed in a shortened measurement with reduced number of spokes, shown in the appendix in figure 51. Image adapted from [36].

4.2.4 Comparison between the Bloch and the ISTO model

The impact of the model used for dictionary simulation was investigated by matching entries from the Bloch dictionary to the ISTO dictionary. To reduce the computational burden, this approach was conducted for two off-resonance values: 0 Hz and 30 Hz, which resulted in matching of 2 × 645088 entries.

The deviations between the inputs and the matched parameters are summarized in table 9. The matched off-resonances were identical to the inputs in all cases, whereas T_1 deviated by $-2.0\,\%$ on average for the 0 Hz-input and $-4.1\,\%$ for the 30 Hz-input.

The maximal mean absolute deviation of 18.6 % was found in T_{2l}^* for the 0 Hz-inputs.

Table 9: The impact of the signal model used was investigated by matching the 0 Hz- and the 30 Hz-entries of a Bloch dictionary to the corresponding ISTO dictionary.

ΔB_0 input	metric	T_1	T_{2l}^*	T_{2s}^*	T_2^*	ΔB_0
0 Hz	relative mean (%)	-2.0	1.6	11.3	-0.8	0.0
	relative absolute mean (%)	11.1	18.6	14.1	7.2	0.0
30 Hz	relative mean (%)	-4.1	-1.8	12.2	-12.8	0.0
	relative absolute mean (%)	10.5	12.3	14.6	12.8	0.0

Moreover, the MRF II measurements were reconstructed with both an ISTO and a Bloch dictionary. The resulting parameters in the phantom for both signal models are illustrated in figure 41 and summarized in the appendix, table 12. Good agreement between the models was found for the longitudinal relaxation times. Here, the mean deviation of the Bloch model with respect to the ISTO model was 0.0 % and the maximal deviation was 3.3 %. For the transverse relaxation times, however, stronger differences up to $-25.0\,\%$ were found. The quantified long component T_{2l}^* was found to differ the most. Here, the value only ranges from (23.7 ± 3.1) ms to (28.9 ± 6.0) ms for the Bloch model, whereas the ISTO model yields a range of (26.0 ± 3.6) ms to (38.5 ± 8.0) ms. The T_{2s}^* was in good agreement, except for the 2 % Agar vial, where the deviation was $-15.2\,\%$. The off-resonance distributions were in excellent agreement and the mean voxelwise difference was -0.9 Hz.

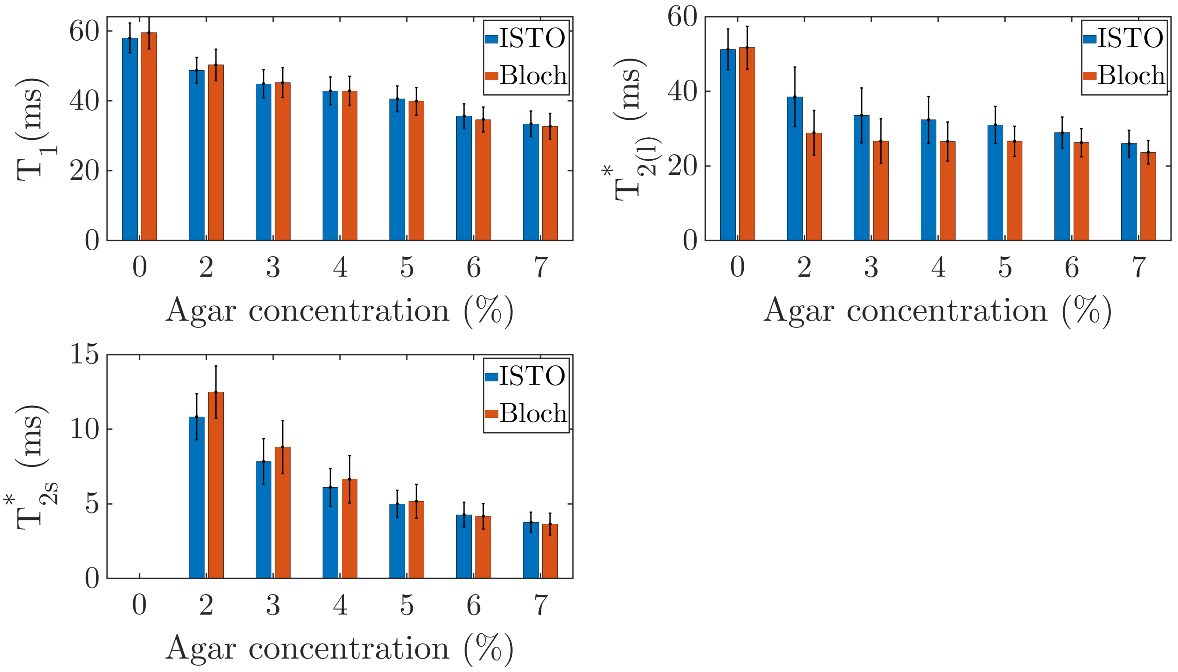

Figure 41: Visual representation of mean and SD of the relaxation times determined in a phantom measurement with both an ISTO and a Bloch model. The values are summarized in the appendix, table 12.

A comparison between Bloch and ISTO results in the in vivo measurements is illustrated in figure 42. In T_1 in BT, the results obtained with the Bloch model differed by 1.8 % on average with respect to the ISTO model, whereas the maximal deviation was 2.2 %. The long and the short transverse relaxation times deviated by 13.2 % and −1.9 % on average with maximal deviations of 16.5 % and −4.1 %. In CSF, the mean T_1 deviation was −2.6 % with a maximal value of −3.5 %, whereas T_2^* differed by −2.5 % on average and the maximum was −2.9 %.

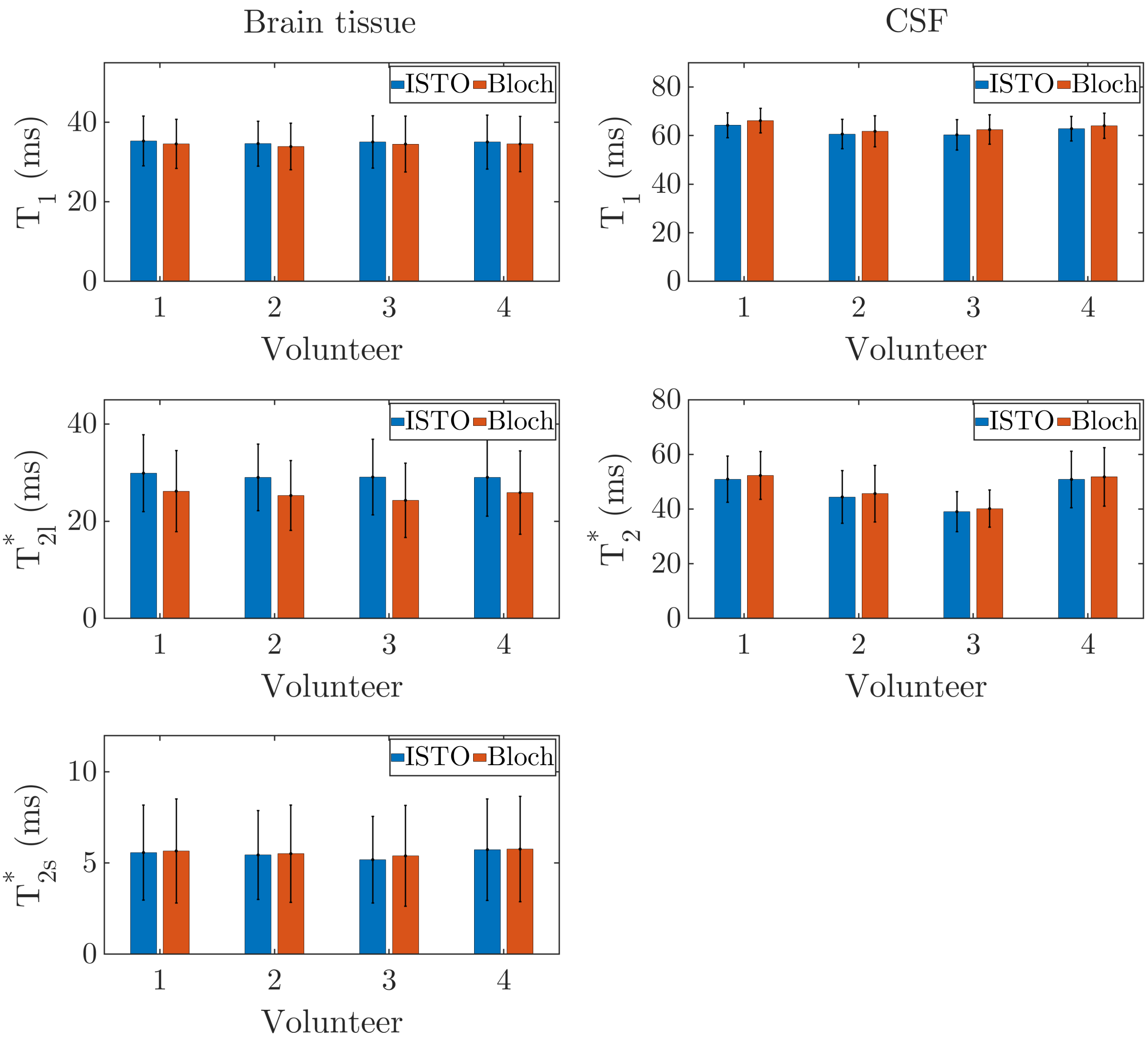

Figure 42: To investigate the impact of the signal model in in vivo experiments, the measured data were reconstructed with both an ISTO and a Bloch dictionary. The highest difference was found in T_{2l}^* in BT, where an average deviation of 13.2 % was found. In T_1 and T_{2s}^* in BT the deviations were 1.8 % and −1.9 %.

5 Discussion

Mapping of sodium relaxation times is of high interest, as they were found to be altered in several diseases [2, 3, 4, 5]. However, low in vivo concentrations and short relaxation times intrinsically result in a low SNR. Hence, sodium imaging suffers from long scan durations, especially in relaxometric mapping, where scan times of approximately 1 h were reported for mapping of one relaxation parameter [4, 8, 9]. The high costs of MR scan time and the difficulty for the patient to lie still throughout the measurement make these long scan times unfeasible in clinical routine. Hence, relaxometric sodium mapping is rarely applied in clinical research and therefore remains to be limited to small scale studies. To tackle this issue, techniques like 3D-MERINA [7] and the variable flip angle method for ^{23}Na [6] have been developed in recent years. In this work, a new MRF approach for simultaneous ^{23}Na quantification of T_1, T_{2l}^*, T_{2s}^*, T_2^* and ΔB_0 with automated differentiation between bi- and monoexponential transverse relaxation was presented.

MRF was proposed in 2013 by Ma et al. [10] to enable simultaneous mapping of T_1 and T_2 in ^{1}H MRI. Since then, MRF based approaches have been used to tackle various multi-parametric mapping problems such as chemical exchange [12] and flow velocity [11]. In X-nuclei imaging, however, MRF was only applied for ^{31}P spectroscopic quantification of the creatine kinase reaction rate [15] and for compartment differentiation based on known ^{23}Na relaxation times [14].

In this work, the potential of ^{23}Na MRF for relaxometric mapping was investigated, which was approached in two stages.

First, a 2D MRF framework was developed which was validated in both simulations and phantom experiments. Subsequently, an in vivo study was conducted in five healthy volunteers. After this was successful, a 3D MRF framework with two pulse sequences was implemented to improve the accuracy and the scan efficiency of the 2D sequence. Here, an improved signal model was used to allow full description of the spin dynamics of spin 3/2 particles. Further, a more efficient pulse sequence was proposed which applies a hybrid of single- and double-echo readouts and an improved FA pattern was used, optimized based on the CRLB.

Note that the 3D sequences were developed as an improvement of the 2D sequence to increase the quantification efficiency. Hence, other potential improvements of the 2D sequence were directly implemented in the more efficient 3D framework and refining of the 2D framework was not pursued.

5.1 Sequence structure and measurements

Each MRF sequence used in this work, can be divided into multiple pulse trains, in which the FA, TE and TR are varied to drive the magnetization in non-steady state conditions and therefore enable the simultaneous quantification of T_1, T_{2l}^* and T_{2s}^* (T_2^* respectively). While the T_1 encoding is mainly achieved by FA variation, the apparent transverse relaxation times are encoded by variation of TE, which makes the sequence inherently sensitive to ΔB_0. A radial center-out readout was used for spatial encoding for both the 2D and the 3D sequences. The readout direction of each pulse train is incremented linearly and within each pulse train by the golden angle for 2D MRF and by the 13th tiny golden angle for 3D MRF. This approach results in 1000 homogeneously sampled time frames in k-space with successively rotated readout directions.
The MRF pulse sequences use a FISP-based sequence design [31] and start with a VERSE pulse with variable amplitude in the 2D case, whereas a rect pulse is applied in the 3D sequences. Next, a variable TE was inserted, followed by a DA readout gradient, a rewinder gradient in read direction and a spoiler gradient in z-direction. Since the next excitation pulse is played out directly after the spoiler gradient, the variable TE directly results in varying TR.

5.1.1 FA pattern

The FA pattern of the 2D MRF sequence was heuristically designed by combining sine, sawtooth wave, step and sinc functions and calculating their auto-correlations in a $T_1 - T_{2l}^*$, a $T_1 - T_{2s}^*$ and a $T_1 - T_2^*$ plane as a measure of their encoding capability. The resulting FA pattern consists of two half sinc functions, overlaid with step-like modulations. The number of correlations above 99.95 % was reduced by 33 % for the optimized pattern compared to the initial ^{1}H FISP pattern [31]. However, even though the reduction of high correlation entries hints an improved distinguishability between the signal evolutions, this has no implications on the signal amplitude and thus on the SNR. Consequently, the new pattern does not necessarily correspond to better encoding in real measurements. In ^{23}Na MRF this effect is important, as here the SNR is dominated by thermal noise, whereas the SNR in ^{1}H MRF is dominated by the undersampling. To give an intuitive example, let's assume a normalized fingerprint with 999 vanishing signal entries and a single 1 at any arbitrary position in the fingerprint. A second fingerprint is constructed similarly but with the non-vanishing entry at a neighboring position. Consequently, the correlation between the latter, defined as the scalar product, is 0 and they are perfectly distinguishable. Nevertheless, in a real measurement this is unpractical because of two reasons. First of all, spatial information is only acquired at the non-zero entry and therefore is not sufficient for image reconstruction. Second, the noise present challenges separation of the fingerprints based on only these two samples. To further validate the encoding capabilities of the new pattern, spatially resolved simulations in a numerical head model in presence of complex Gaussian noise and undersampling were conducted and compared to simulations that used the initial ^{1}H FISP pattern. In this experiment, the mean absolute difference of the average relaxation times in BT and CSF between MRF with the proposed FA pattern and the ground truth was 4.7 %, whereas the ^{1}H pattern resulted in deviations of 4.9 %. Consequently, the new pattern was used in all 2D measurements. However, the difference of 0.2 % and therefore the improvement due to the new pattern appears to be minor.

Combining different functions or an automated numerical optimization based on the CRLB, which was used in the 3D FA pattern design, could yield an improved FA pattern as discussed in the following.

While the 3D MRF I sequence uses the same FA pattern as the 2D sequence, the FA pattern of the 3D MRF II sequence was numerically optimized using the CRLB. To reduce the computational burden, only 50 subsequent FAs were optimized and this batch was concatenated 20 times to yield 1000 pattern entries. Due to the constantly changing TE and TR, the signal state in each cycle is still unique. However, optimization of all 1000 entries could further improve the encoding capability of the sequence. Moreover, the pattern length and the TE pattern could be optimized as well. Yet, this would be computationally unfeasibly expensive as the 50 FA optimization already required about 50 h on a standalone PC and the computational burden grows exponentially with the number of parameters for a finite differences optimization. Furthermore, it is likely that a local optimum was found and the global optimum is still unknown. Moreover, the optimization was performed for a single representative parameter set. Even though the CRLB was reduced by 58 % on average in 1000 parameter combinations in a large parameter space, a more general solution might be found if the optimization was performed on a multitude of optimization parameter sets, which again, would lead to high computational demands.

5.1.2 TE pattern

After the excitation pulse, a variable TE was inserted, which was varied pseudo-randomly between the minimal echo time TE_{min} (2D: 1.55 ms; 3D: 0.55 ms) and TE_{min}+ 20 ms to tackle the challenge of encoding a large range of apparent transverse relaxation times. Here, the T_{2s}^* is mainly encoded with the short TE entries, whereas the long entries are required for quantification of T_{2l}^* and T_2^*. Consequently, the TE pattern comprises a trade-off between time efficiency and sensitivity towards the short and the long transverse relaxation times. However, a more sophisticated TE pattern could be constructed using the CRLB.

In the 3D MRF II sequence, the readout efficiency was increased by implementing an additional readout between the excitation pulse and signal acquisition when the current TE was longer than the time required for acquisition of a spoke. In theory, the readout efficiency could be further increased by using more data acquisitions with shorter duration, which would result in an even higher sampling density within each cycle. Nonetheless, this might need exact mapping of the gradients as any hardware error is summed up in each cycle, which is a common problem in echo planar imaging (EPI) [48].

5.1.3 Minimal number of spokes

The number of spokes required per time frame was investigated for the 2D and the 3D MRF II sequence.

For the 2D sequence, spatial simulations were conducted and the mean relaxation times in BT and CSF were determined in dependence of the number of spokes. Here, 14 spokes were found to be sufficient for a nominal in-plane resolution of $2{\times}2\,\mathrm{mm}^2$, whereas only 7 spokes were required for a resolution of $4{\times}4\,\mathrm{mm}^2$. This factor of two meets the expectations as the Nyquist criterion for 2D radial imaging depends linearly on the inverse of the voxel width. It became apparent that the quantified parameters asymptotically approached a slightly different limit than the ground truth. This can be explained by the spatial encoding, which leads to ringing artifacts and partial volume effects. The minimal spoke number was used in the measurements as this requires only one averaging step in the beginning of the reconstruction, whereas a higher number of spokes severely increases the computational burden in the whole reconstruction. Furthermore, Behl et al. [49] found an improved image quality for averaged data compared to more densely sampled data in a compressed sensing (CS) reconstruction. This can be explained since CS yields good results for removing undersampling artifacts but cannot distinguish between thermal noise and actual image features. Comparison of an in vivo measurement with 7 spokes and 21 averages and a measurement with 147 spokes and a single average supported the findings by Behl et al. [49] as similar mean relaxation parameters were found, but the maps appeared more noisy for the 147 spoke measurement and all SDs

were increased.
The minimal measurement duration of 3D MRF II was investigated by retrospective undersampling of the measured phantom data. Note that the measurement duration and the number of spokes are equivalent since no averaging was performed in the 3D measurements. Here, the mean relaxation times in each compartment only changed mildly with reduced spokes, whereas a loss of spatial information in form of smearing was found for short virtual measurement times. A good compromise between image quality and measurement time was found to be the 21 min measurement (50 spokes per time frame) in the piecewise constant phantom. On the other hand in the in vivo experiments, stronger image alterations became apparent, which can be explained by the lower sodium concentration, the lower resolution and the small lateral ventricles. Here, a scan time of 32 min (75 spokes per time frame) appeared to be promising, so a second measurement in a representative volunteer was conducted with reduced measurement time. This experiment yielded similar results as the retrospectively undersampled data. However, more quantitative characterization of the effects of reduced spatial information, such as the peak-SNR (PSNR) or the structural similarity (SSIM), could be subject to future research.

5.1.4 Validation measurements

Phantom measurements were used to test the encoding capabilities of the MRF sequences by comparing the results to the references.
In the 2D MRF experiments, a mean deviation of 4.0 % was found, whereas the mean absolute difference was 12.4 % because 2D MRF overestimated T_{2l}^* in all cases. Here, the mean deviation was 15 %. These deviations could arise from signal contributions of refocusing T_2-pathways, which were neglected by the approximation of $T_2^* = T_2$ (T_{2l}^* respectively). T_{2s}^*, on the other hand, was always underestimated with an average difference of 14 %. The longitudinal relaxation parameters only deviated by 2 % and good agreement was found for the ΔB_0 map, where the mean voxelwise difference was 2.7 Hz. Further, the differentiation between voxels experiencing a biexponential decay and the ones relaxing monoexponentially appeared to be stable, as the MRF reconstruction provided the same classification like the reference for more than 80 % of the voxels in six out of eight compartments. In the compartments with 1 % and 2 % Agar, MRF found the same classification for 51 % and 73 % of the voxels, which is in agreement with the reference where 61 % and 59 % were determined. These uncertainties in classification might be caused by a similarly well description of the relaxation behavior by both re-

laxation types, so that noise determined the detected relaxation type. Further, a single compartment model was assumed in each vial, which might be violated for the low Agar concentrations. In general, the MRF maps visually appear noisier, which is supported by the increased SDs, found in all quantified parameters. Then again, the MRF experiments were acquired in a 5-fold reduced scan time compared to the references and investigation of the SNR efficiency could be subject of future research.

In the 3D experiments both an increased specificity and sensitivity were found for the 3D MRF sequences compared to 2D MRF and 3D MRF II was superior to 3D MRF I. Both the mean and the mean absolute deviation between MRF I and the reference methods were 10.8 % since MRF I constantly overestimated the parameters. MRF II, on the contrary, only deviated by 1.0 % on average and the mean absolute difference was 4.6 %. Moreover, the SD was reduced for the MRF II sequence in all cases compared to the MRF I sequence and the mean SD reduction was 39 %.

All three sequences were measured in approximately 1 h each, but the 2D sequence was tested in a different phantom than the 3D versions. Further, the voxel volume of the 2D sequence was $48\,\mathrm{mm}^3$, whereas the 3D sequences were acquired with a voxel volume of $27\,\mathrm{mm}^3$. Consequently, a fairer comparison between the sequences could be performed by measuring the sequences within the same measurement session in the same phantom and both similar voxel volumes as well as similar number of voxels.

5.1.5 In vivo measurements

The relaxation times in the human head were measured in two in vivo studies, one conducted with the 2D MRF sequence and one with 3D MRF II.

In the 2D study, five healthy volunteers were measured, where 7 spokes per time frame and 21-fold averaging yielded a measurement time of 1 h for a nominal resolution of $4 \times 4{\times}12\,\mathrm{mm}^3$. The 3D MRF study, conducted in four healthy volunteers, was also measured in approximately 1 h measurement time with a nominal resolution of $(5\,\mathrm{mm})^3$. Average T_1 of (38.9 ± 4.8) ms and (67.1 ± 6.3) ms were found in BT and CSF with the 2D framework, which are in agreement with the 3D MRF II experiments, for which (35.0 ± 3.2) ms and (61.9 ± 2.8) ms were determined. This is consistent with literature, where values around 37 ms and 64 ms are reported [4]. The 2D MRF framework quantified $T_{2l}^* = (29.2 \pm 4.9)$ ms and $T_{2s}^* = (4.7 \pm 1.2)$ ms in BT, whereas 3D MRF II yielded $T_{2l}^* = (29.3 \pm 3.8)$ ms and $T_{2s}^* = (5.5 \pm 1.3)$ ms. Here, literature reports broad ranges of 20 ms–40 ms and 2 ms–6.5 ms [7, 8, 9], underlining the difficulty of accurate relaxometric mapping. In CSF, a monoexponential transverse relaxation time of $T_2^* = (41.5 \pm 3.4)$ ms

was found with 2D MRF and $T_2^* = (46.3 \pm 4.5)$ ms with 3D MRF. These values are lower than the literature values, for which values about 55 ms [4, 50] are reported.
This deviation might be explained by residual partial volume effects, as the maximal diameter of the lateral ventricles within the five volunteers was 15 mm at the widest part. Hence, the nominal resolutions of $4 \times 4 \times 12\,\mathrm{mm}^3$ for the 2D case and $(5\,\mathrm{mm})^3$ for the 3D experiments are low compared to the ventricle size, so that the CSF ROIs are often only two voxels wide and only small areas at the BT-CSF interface were eroded.
Moreover, simulation experiments hinted that the nominal resolution used in the 3D in vivo experiments allows reliable quantification of structures with a diameter of 15 mm–25 mm or larger, making PV effects likely to occur in CSF quantification.
All SDs in the 3D MRF II results were reduced compared to the 2D MRF results, except for T_2^*. Moreover, the phantom experiments, discussed above, showed more accurate quantification for MRF II. Hence, the 3D MRF II framework was heavily improved compared to 2D MRF, as it provided both higher sensitivity and specificity while covering a larger scan volume with smaller voxel volume in a similar measurement time.

5.2 Potential parameter biases

The potential biases of the quantified parameters are discussed in the following. Note that the 3D MRF II framework was the final version developed in this work. Therefore, some experiments, such as testing of the parameter bias by B_1 deviations, were representatively conducted using only the MRF II framework.

5.2.1 Signal model

In the 2D MRF framework, the dictionary was calculated using non-interacting two-pool Bloch equations. For this, 60 % of the signal were assumed to originate from a pool with $T_2^* = T_{2s}^*$ and 40 % from a second pool with $T_2^* = T_{2l}^*$ to allow biexponential transverse relaxation. This ratio is given by the theoretical quantum mechanical description of spin 3/2 particles for a single compartment [19]. In biological tissues, however, various environments are commonly present within one voxel, potentially leading to a changed effective ratio [1]. This could be taken into account as a free parameter in the dictionary simulation, which on the other hand would dramatically increase the computational burden in both the simulation and the image reconstruction. Separation of the parameters would be challenging, making this approach currently unfeasible. Another limitation of the signal model is the assumption of negligible signal contributions by refocusing

T_2-pathways, which allowed the reduction of the computational burden by simulating $T_2^* = T_2$. Yet, if such signal contributions arise, this can lead to a bias in T_2^* (T_{2l}^* respectively). Nevertheless, this effect is assumed to be small since the sequence is not optimized for refocusing and the average TR of 23.34 ms is in the order of T_{2l}^*, which further reduces the chance of refocusing T_2 signal contributions. Moreover, higher order quantum coherences are not represented in the model, which could lead to a bias in the quantified relaxometric parameters, as discussed below. A refined dictionary could be constructed for 2D MRF by implementing the full sequence in the ISTO frameworks developed for 3D MRF, which would lead to high computational cost. However, this approach was not pursued due to the higher efficiency of 3D MRF sequences compared to 2D MRF.

In the 3D MRF framework, the dictionary simulation was refined by implementing an ISTO simulation framework to cover the full spin dynamics of spin 3/2 particles. However, this signal model again is based on some assumptions. The ISTO framework inherently yields a biexponential longitudinal relaxation, whereas a monoexponential model is commonly assumed in fitting of measured data since differentiation of the components is unstable in presence of noise. Hence, a monoexponential T_1 estimate was developed in this work. Further, a Lorentz distribution of off-resonances was assumed in each voxel to introduce T_2^* over T_2, which is a commonly used concept [51]. Nevertheless, some literature suggests that a Gaussian distribution might describe the situation in biological tissues better [51]. Another assumption was that the residual quadrupolar interaction vanishes ($\omega_q = 0$). Literature found signal contributions for which $\omega_q \neq 0$ in the human head [52], but their amplitude appears to be small. Moreover, the assumption of vanishing residual quadrupolar interaction is implicitly also made when a bi- or monoexponential signal model is fitted to FID data, which is a common approach in ^{23}Na relaxometry. Last, the signal in each voxel was assumed to originate from a single compartment which could cause a bias in the quantified parameters, as investigated in the PV simulations. This could be tackled by the use of multi-compartment MRF [53].

The impact of the signal model used was investigated in two ways: Entries in a 3D MRF II Bloch dictionary were matched to the corresponding ISTO dictionary for the off-resonance values of 0 Hz and 30 Hz. For this, the highest mean absolute relative deviation was 18.6 %, found in T_{2l}^* for $\Delta B_0 = 0$ Hz. To investigate the impact of the model onto the parameters in measurements, the phantom data was reconstructed with both an ISTO and a Bloch dictionary. A maximal deviation of 3.3 % was found in T_1, whereas T_{2l}^* and T_{2s}^* differed with up to −25 % and 15.2 %. The same approach was used

for the in vivo measurements, where T_{2l}^* in BT deviated the most with an average of 13.2 %. These findings hint that the ISTO model mainly improved the T_{2l}^* quantification, whereas the other parameters were less effected.
In future, MRF could be used to determine spectral density parameter maps (J_0, J_1, J_2) instead of relaxation times, as the spectral density parameters are the basis of the ISTO model. On the downside, this would require validation measurements of J_0, J_1, J_2, ΔB_0 and the intravoxel ΔB_0-distribution and examination of the CRLB to investigate their separability.

5.2.2 Partial volume effects

The impact of PV effects was estimated by simulating the signal evolution for a mix of BT and CSF with varying ratio. The classification of the relaxation type appeared to be stable, as the matching determined a biexponential relaxation for a BT content of 52 % and higher. However, strong effects of PV contributions on the quantified parameters were found, especially in T_{2l}^* in BT, where a severe bias in the quantified parameters was found. This bias can be explained since mixing of BT and CSF results in a triexponential transverse relaxation and a biexponential longitudinal relaxation, which is not modeled in the dictionary. Similar problems arise in conventional fitting when and a biexponential signal model is fitted to the FID of the mixed compartments.
Such PV effects can arise from structures smaller than the resolution and by signal bleeding due to the PSF. For fully sampled measurements, the latter can be simulated and consequently be corrected for, which is a common approach in ^{23}Na TSC quantification [54]. In MRF, however, the PSF is unknown due to the undersampling and is likely to differ between the coefficient images in the compressed basis. Consequently, the imaging process was simulated to estimate the smallest quantifiable image features for nominal resolutions of $(3\,\mathrm{mm})^3$ and $(5\,\mathrm{mm})^3$. Here, structures larger than 3-5 times the voxel width showed reasonable parameter quantifiability since this allowed eroding of one to two pixels at each side. Consequently, a nominal isotropic resolution of 3 mm appears to allow relaxometric quantification of structures with a diameter of 9 mm–15 mm or larger. Structures with a size of 15 mm–25 mm or larger can be quantified with a nominal isotopic resolution of 5 mm. This suggests that the relaxation times quantified in CSF are PV biased as the diameter of the lateral ventricles is in the order of 15 mm. However, similar issues are expected in gold standard techniques such as IR experiments. Here, the PSF also results in signal mixing of adjacent voxels, resulting in a quantification bias at tissue interfaces.

5.2.3 $\mathbf{B_1}$ deviations

In all measurements a uniform B_1 distribution was assumed, based on previous work [55]. To estimate the potential parameter bias due to B_1 imperfections, the signal evolution of BT and CSF for the MRF II sequence for a relative B_1 range of 87.0 %–109.5 % was simulated, which was found to be a realistic range in an in vivo experiment. Subsequent matching to the dictionary resulted in a maximal deviation of 15.0 % and a slope $\frac{\mathrm{d}T_1}{\mathrm{d}B_1}$ of approximately 1.22. Yet, simulation experiments were restricted to a BT and a CSF compartment, which could be extended to a larger parameter range in future research. Moreover, B_1 could be implemented as a dictionary parameter to correct for those errors, which might be especially useful when using RF coils with reduced B_1 homogeneity. However, this would lead to a highly increased computational burden for both the dictionary simulation and the reconstruction.

6 Summary and conclusion

As sodium relaxation times were found to be altered in several diseases, their quantification may enable new opportunities in clinical research. Hence, a new MRF approach for simultaneous ^{23}Na quantification of T_1, T_{2l}^*, T_{2s}^*, T_2^* and ΔB_0 was presented in this work, which is the first application of MRF-based relaxometry in X-nuclei imaging.
First, a 2D MRF framework was developed, where a FISP-based radial sequence with density adapted readout gradients and VERSE pulses [56] is used. Here, the magnetization is driven in non-steady state conditions by varying the FA, which enables T_1 encoding, and variation of TE and TR, sensitizing the sequence towards the transverse relaxation times. In the dictionary simulations, a two-pool Bloch model was applied to describe biexponential transverse relaxation.
Simulation experiments were conducted for FA pattern design and for investigation of the feasibility of spatially resolved ^{23}Na MRF. Further, the minimal number of spokes per time frame was determined in dependence of the in-plane resolution.
Phantom experiments were used for sequence validation by comparing the MRF results to gold standard references, where a mean deviation of 4.0 % was found in the quantified relaxation times. The automatic differentiation between bi- and monoexponential transverse relaxation was in agreement with the reference in all phantom compartments and ΔB_0 differed by 2.7 Hz on average.
In a subsequent in vivo study, conducted in five healthy volunteers, the relaxation times in the human head were determined. Here, a nominal resolution of $4 \times 4 \times 12\,\mathrm{mm}^3$ was achieved in a scan duration of approximately 1 h. In brain tissue, average relaxation times of $T_1 = (38.9 \pm 4.8)\,\mathrm{ms}$, $T_{2l}^* = (29.2 \pm 4.9)\,\mathrm{ms}$ and $T_{2s}^* = (4.7 \pm 1.2)\,\mathrm{ms}$ were found. In CSF a monoexponential transverse relaxation was determined, yielding $T_1 = (67.1 \pm 6.3)\,\mathrm{ms}$ and $T_2^* = (41.5 \pm 3.4)\,\mathrm{ms}$.
Secondly, the 3D MRF framework with two 3D MRF sequences was developed to improve both the scan efficiency and the accuracy of the 2D sequence. Here, a refined signal model, based on ISTOs [19, 20], was implemented to allow full description of the spin dynamics of spin 3/2 particles. However, the ISTO model intrinsically yields a biexponential longitudinal relaxation, whereas a monoexponential relaxation model is commonly assumed in literature, as separation of T_{1l} and T_{1s} is challenging with the given noise level. Hence, a monoexponential T_1 estimate was constructed in this work to allow comparison to literature and reference methods. Further, T_2^* relaxation was simulated over T_2 (T_{2l} and T_{2s} respectively) by assuming a Lorentzian shaped intravoxel

ΔB_0 distribution.

In the 3D MRF sequences, non-selective excitation pulses and density adapted readout gradients are applied [26]. The 3D MRF I sequence uses the same FA pattern as 2D MRF and the TE pattern is similar except for a global off-set of $-1.0\,\mathrm{ms}$, as no rewinder gradient is required due to the non-selective excitation pulses. The 3D MRF II sequence was improved in two ways: In a first step, the scan efficiency was increased by inserting an additional readout in each TE delay that is long enough, yielding a hybrid sequence of single- and double-echo readouts. Subsequently, an improved FA pattern was applied, which was optimized using the Cramér Rao lower bound.

Simulation experiments were conducted for investigation of the impact of PV contributions on the quantified parameters. Further, the smallest quantifiable image features were investigated with respect to the nominal resolution and the impact of B_1 imperfections was evaluated. The latter hinted a maximal bias of 15.0 % of the relaxation times for a realistic B_1 distribution in the human head. A comparison between the Bloch and the ISTO model showed that the latter mainly improved quantification of T^*_{2l}, whereas the other parameters were less affected.

Phantom experiments yielded a mean deviation between MRF I and the references of 10.8 %, whereas MRF II only deviated by 1.0 %. A second in vivo study was conducted with MRF II, where a nominal resolution of $(5\,\mathrm{mm})^3$ was acquired in a scan duration of about 1 h. Here, good agreement with literature and the 2D study was observed, as $T_1 = (35.0 \pm 3.2)\,\mathrm{ms}$, $T^*_{2l} = (29.3 \pm 3.8)\,\mathrm{ms}$ and $T^*_{2s} = (5.5 \pm 1.3)\,\mathrm{ms}$ were quantified in BT. In CSF, $T_1 = (61.9 \pm 2.8)\,\mathrm{ms}$ and $T^*_2 = (46.3 \pm 4.5)\,\mathrm{ms}$ were found. Further experiments showed that 3D relaxometric mapping of the human head is possible using MRF within a shortened scan time of approximately $\frac{1}{2}\,\mathrm{h}$ with a nominal resolution of $(5\,\mathrm{mm})^3$.

These findings suggest that ^{23}Na MRF is a promising candidate to push sodium relaxometry towards clinically feasible scan times.

7 Appendix

7.1 Abbreviations

ADP	adenosine diphosphate
ATP	adenosine triphosphate
BT	brain tissue
BW	bandwidth
BWT	band width time product
CG	conjugate gradient
CS	compressed sensing
CSF	cerebrospinal fluid
CRLB	Cramér Rao lower bound
DA	density adapted
EFG	electrical field gradient
EPI	echo-planar imaging
FA	flip angle
FID	free induction decay
GM	gray matter
GT	ground truth
HWHM	half width at half maximum
ISTO	irreducible spherical tensor operator
IR	inversion recovery
MR	magnetic resonance
MRF	magnetic resonance fingerprinting
MRI	magnetic resonance imaging
MRS	magnetic resonance spectroscopy
NMR	nuclear magnetic resonance
PSF	point spread function
PSNR	peak-signal-to-noise ratio
PT	pulse train
RF	radio frequency
ROI	region of interest
SNR	signal-to-noise ratio
SSIM	structural similarity
TE	echo time
TI	inversion time
TPI	twisted projection imaging
TR	repetition time
TSC	tissue sodium concentration
TSE	turbo spin echo
UHF	ultra-high fields
USF	undersampling factor

UTE	ultra-short echo time
VERSE	variable-rate selective excitation
WM	white matter

7.2 Matrix representations of ISTOs for spin 3/2 systems

$$T_{00} = \begin{pmatrix} 1 & 0 & 0 & 0 \\ 0 & 1 & 0 & 0 \\ 0 & 0 & 1 & 0 \\ 0 & 0 & 0 & 1 \end{pmatrix} \qquad T_{10} = \tfrac{1}{2} \begin{pmatrix} 3 & 0 & 0 & 0 \\ 0 & 1 & 0 & 0 \\ 0 & 0 & -1 & 0 \\ 0 & 0 & 0 & -3 \end{pmatrix}$$

$$T_{11} = \tfrac{1}{\sqrt{2}} \begin{pmatrix} 0 & -\sqrt{3} & 0 & 0 \\ 0 & 0 & -2 & 0 \\ 0 & 0 & 0 & -\sqrt{3} \\ 0 & 0 & 0 & 0 \end{pmatrix} \qquad T_{1-1} = \tfrac{1}{\sqrt{2}} \begin{pmatrix} 0 & 0 & 0 & 0 \\ \sqrt{3} & 0 & 0 & 0 \\ 0 & 2 & 0 & 0 \\ 0 & 0 & \sqrt{3} & 0 \end{pmatrix}$$

$$T_{20} = \sqrt{\tfrac{3}{2}} \begin{pmatrix} 1 & 0 & 0 & 0 \\ 0 & -1 & 0 & 0 \\ 0 & 0 & -1 & 0 \\ 0 & 0 & 0 & 1 \end{pmatrix} \qquad T_{21} = \sqrt{3} \begin{pmatrix} 0 & -1 & 0 & 0 \\ 0 & 0 & 0 & 0 \\ 0 & 0 & 0 & 1 \\ 0 & 0 & 0 & 0 \end{pmatrix}$$

$$T_{2-1} = \sqrt{3} \begin{pmatrix} 0 & 0 & 0 & 0 \\ 1 & 0 & 0 & 0 \\ 0 & 0 & 0 & 0 \\ 0 & 0 & -1 & 0 \end{pmatrix} \qquad T_{22} = \sqrt{3} \begin{pmatrix} 0 & 0 & 1 & 0 \\ 0 & 0 & 0 & 1 \\ 0 & 0 & 0 & 0 \\ 0 & 0 & 0 & 0 \end{pmatrix}$$

$$T_{2-2} = \sqrt{3} \begin{pmatrix} 0 & 0 & 0 & 0 \\ 0 & 0 & 0 & 0 \\ 1 & 0 & 0 & 0 \\ 0 & 1 & 0 & 0 \end{pmatrix} \qquad T_{30} = \tfrac{3}{2\sqrt{10}} \begin{pmatrix} 1 & 0 & 0 & 0 \\ 0 & -3 & 0 & 0 \\ 0 & 0 & 3 & 0 \\ 0 & 0 & 0 & -1 \end{pmatrix}$$

$$T_{31} = \frac{3}{\sqrt{10}} \begin{pmatrix} 0 & -1 & 0 & 0 \\ 0 & 0 & \sqrt{3} & 0 \\ 0 & 0 & 0 & -1 \\ 0 & 0 & 0 & 0 \end{pmatrix} \quad T_{3-1} = \frac{3}{\sqrt{10}} \begin{pmatrix} 0 & 0 & 0 & 0 \\ 1 & 0 & 0 & 0 \\ 0 & -\sqrt{3} & 0 & 0 \\ 0 & 0 & 1 & 0 \end{pmatrix}$$

$$T_{32} = \frac{3}{2} \begin{pmatrix} 0 & 0 & 1 & 0 \\ 0 & 0 & 0 & -1 \\ 0 & 0 & 0 & 0 \\ 0 & 0 & 0 & 0 \end{pmatrix} \qquad T_{3-2} = \frac{3}{2} \begin{pmatrix} 0 & 0 & 0 & 0 \\ 0 & 0 & 0 & 0 \\ 1 & 0 & 0 & 0 \\ 0 & -1 & 0 & 0 \end{pmatrix}$$

$$T_{33} = \frac{3}{\sqrt{2}} \begin{pmatrix} 0 & 0 & 0 & -1 \\ 0 & 0 & 0 & 0 \\ 0 & 0 & 0 & 0 \\ 0 & 0 & 0 & 0 \end{pmatrix} \qquad T_{3-3} = \frac{3}{\sqrt{2}} \begin{pmatrix} 0 & 0 & 0 & 0 \\ 0 & 0 & 0 & 0 \\ 0 & 0 & 0 & 0 \\ 1 & 0 & 0 & 0 \end{pmatrix}$$

7.3 Differential equation of motion for spin 3/2 systems

$$\frac{\mathrm{d}}{\mathrm{d}T}\begin{pmatrix} \hat{T}_{00} \\ \hat{T}_{10} \\ \hat{T}_{11}(s) \\ \hat{T}_{11}(a) \\ \hat{T}_{20} \\ \hat{T}_{21}(s) \\ \hat{T}_{21}(a) \\ \hat{T}_{22}(s) \\ \hat{T}_{22}(a) \\ \hat{T}_{30} \\ \hat{T}_{31}(s) \\ \hat{T}_{31}(a) \\ \hat{T}_{32}(s) \\ \hat{T}_{32}(a) \\ \hat{T}_{33}(s) \\ \hat{T}_{33}(a) \end{pmatrix} = M \begin{pmatrix} \hat{T}_{00} \\ \hat{T}_{10} \\ \hat{T}_{11}(s) \\ \hat{T}_{11}(a) \\ \hat{T}_{20} \\ \hat{T}_{21}(s) \\ \hat{T}_{21}(a) \\ \hat{T}_{22}(s) \\ \hat{T}_{22}(a) \\ \hat{T}_{30} \\ \hat{T}_{31}(s) \\ \hat{T}_{31}(a) \\ \hat{T}_{32}(s) \\ \hat{T}_{32}(a) \\ \hat{T}_{33}(s) \\ \hat{T}_{33}(a) \end{pmatrix} \tag{7.1}$$

$$
M = \left(\begin{matrix}
0 & 0 & 0 & 0 & 0 & 0 & 0 & 0 \\
\frac{2}{5}J_1 + \frac{8}{5}J_2 & -\frac{2}{5}J_1 - \frac{8}{5}J_2 & -i\omega_1 & 0 & 0 & 0 & 0 & 0 \\
0 & -i\omega_1 & -\frac{3}{5}J_0 - J_1 - \frac{2}{5}J_2 & i\omega_{off} & 0 & 0 & i\sqrt{\frac{3}{5}}\omega_Q & 0 \\
0 & 0 & i\omega_{off} & -\frac{3}{5}J_0 - J_1 - \frac{2}{5}J_2 & 0 & i\sqrt{\frac{3}{5}}\omega_Q & 0 & 0 \\
0 & 0 & 0 & 0 & -2J_1 - 2J_2 & -i\sqrt{3}\omega_1 & 0 & 0 \\
0 & 0 & 0 & i\sqrt{\frac{3}{5}}\omega_Q & -i\sqrt{3}\omega_1 & -J_0 - J_1 - 2J_2 & 0 & -i\omega_1 \\
0 & 0 & i\sqrt{\frac{3}{5}}\omega_Q & 0 & 0 & i\omega_{off} & -J_0 - J_1 - 2J_2 & 0 \\
0 & 0 & 0 & 0 & 0 & -i\omega_1 & 0 & -J_0 - 2J_1 - J_2 & \ldots \\
0 & 0 & 0 & 0 & 0 & 0 & -i\omega_1 & i2\omega_{off} \\
\frac{4}{5}J_1 - \frac{4}{5}J_2 & -\frac{4}{5}J_1 + \frac{4}{5}J_2 & 0 & 0 & 0 & 0 & 0 & 0 \\
0 & 0 & -\frac{\sqrt{6}}{5}J_0 + \frac{\sqrt{6}}{5}J_2 & 0 & 0 & 0 & i\sqrt{\frac{2}{5}}\omega_Q & 0 \\
0 & 0 & 0 & -\frac{\sqrt{6}}{5}J_0 + \frac{\sqrt{6}}{5}J_2 & 0 & i\sqrt{\frac{2}{5}}\omega_Q & 0 & 0 \\
0 & 0 & 0 & 0 & 0 & 0 & 0 & 0 \\
0 & 0 & 0 & 0 & 0 & 0 & 0 & i\omega_Q \\
0 & 0 & 0 & 0 & 0 & 0 & 0 & 0 \\
0 & 0 & 0 & 0 & 0 & 0 & 0 & 0
\end{matrix}\right.
$$

$$
\left.\begin{matrix}
 & 0 & 0 & 0 & 0 & 0 & 0 & 0 & 0 \\
 & 0 & -\frac{4}{5}J_1 + \frac{4}{5}J_2 & 0 & 0 & 0 & 0 & 0 & 0 \\
 & 0 & 0 & -\frac{\sqrt{6}}{5}J_0 + \frac{\sqrt{6}}{5}J_2 & 0 & 0 & 0 & 0 & 0 \\
 & 0 & 0 & 0 & -\frac{\sqrt{6}}{5}J_0 + \frac{\sqrt{6}}{5}J_2 & 0 & 0 & 0 & 0 \\
 & 0 & 0 & 0 & 0 & 0 & 0 & 0 & 0 \\
 & 0 & 0 & 0 & i\sqrt{\frac{2}{5}}\omega_Q & 0 & 0 & 0 & 0 \\
 & -i\omega_1 & 0 & i\sqrt{\frac{2}{5}}\omega_Q & 0 & 0 & 0 & 0 & 0 \\
 & i2\omega_{off} & 0 & 0 & 0 & 0 & i\omega_Q & 0 & 0 \\
\ldots & J_0 - 2J_1 - J_2 & 0 & 0 & 0 & i\omega_Q & 0 & 0 & 0 \\
 & 0 & -\frac{8}{5}J_1 - \frac{2}{5}J_2 & -i\sqrt{6}\omega_1 & 0 & 0 & 0 & 0 & 0 \\
 & 0 & -i\sqrt{6}\omega_1 & -\frac{2}{5}J_0 - J_1 - \frac{3}{5}J_2 & i\omega_{off} & -i\sqrt{\frac{5}{2}}\omega_1 & 0 & 0 & 0 \\
 & 0 & 0 & i\omega_{off} & -\frac{2}{5}J_0 - J_1 - \frac{3}{5}J_2 & 0 & -i\sqrt{\frac{5}{2}}\omega_1 & 0 & 0 \\
 & i\omega_Q & 0 & -i\sqrt{\frac{5}{2}}\omega_1 & 0 & -J_0 - J_2 & i2\omega_{off} & -i\sqrt{\frac{3}{2}}\omega_1 & 0 \\
 & 0 & 0 & 0 & -i\sqrt{\frac{5}{2}}\omega_1 & i2\omega_{off} & -J_0 - J_2 & 0 & -i\sqrt{\frac{3}{2}}\omega_1 \\
 & 0 & 0 & 0 & 0 & -i\sqrt{\frac{3}{2}}\omega_1 & 0 & -J_1 - J_2 & i3\omega_{off} \\
 & 0 & 0 & 0 & 0 & 0 & -i\sqrt{\frac{3}{2}}\omega_1 & i3\omega_{off} & -J_1 - J_2
\end{matrix}\right) \tag{7.2}
$$

7.4 2D Results

7.4.1 Simulations

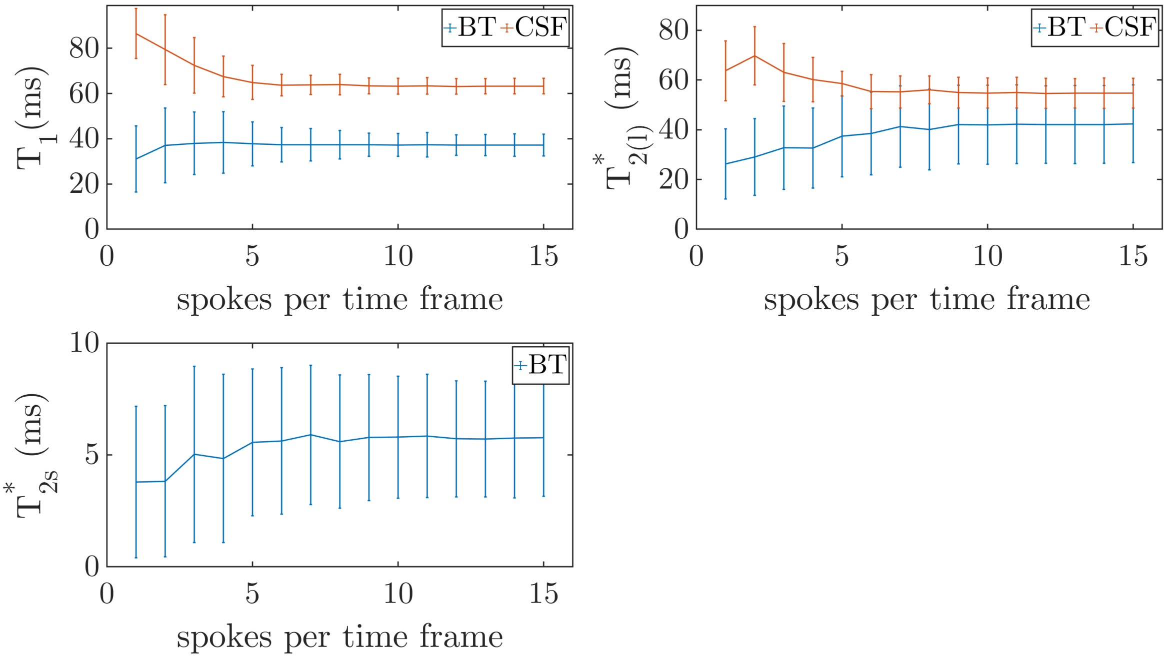

Figure 43: A simulation was conducted to determine the minimal number of spokes required for sufficient reconstruction, described in section 4.1.1.2. Mean and SD of the relaxation parameters in BT and CSF are illustrated for varying number of spokes per time frame for a nominal in-plane resolution of 4×4 mm^2. The minimal number of spokes per time frame was 7, as here the mean deviation of each quantified relaxation parameter was less than 5.0 % with respect to the results obtained with the maximal number of spokes. Image adapted from [40].

7.4.2 Measurements

Table 10: Phantom measurements were conducted to investigate the encoding capabilities of the 2D MRF sequence, explained in section 3.7.1. Mean and SD of all relaxation parameters in each compartment, acquired with 2D MRF and reference methods, are summarized. Mind that the compartments with 0 % and 1 % Agar in the $T_{2(l)}^*$ column decay with a monoexponential T_2^*, whereas the other compartments experience a biexponential relaxation and T_{2l}^* is shown. Table adapted from [40].

Agar	T_1 (ms)		$T_{2(l)}^*$		T_{2s}^*	
conc. (%)	Reference	MRF	Reference	MRF	Reference	MRF
0	56.8 ± 4.6	63.4 ± 12.8	43.3 ± 7.5	55.2 ± 11.9		
1	52.0 ± 3.8	51.2 ± 11.3	21.3 ± 2.7	26.8 ± 5.0		
2	47.5 ± 3.6	48.7 ± 12.0	29.1 ± 9.2	35.3 ± 15.3	9.8 ± 1.4	8.1 ± 4.8
3	44.4 ± 3.8	46.9 ± 11.6	27.5 ± 7.7	31.7 ± 14.2	7.8 ± 1.3	6.4 ± 4.2
4	41.3 ± 3.4	47.4 ± 12.7	27.0 ± 7.8	29.7 ± 12.3	6.5 ± 1.3	5.5 ± 3.7
5	39.1 ± 3.3	41.7 ± 11.8	25.3 ± 7.2	27.3 ± 11.4	5.5 ± 1.1	4.9 ± 3.6
6	37.1 ± 3.6	35.0 ± 11.3	21.0 ± 6.0	24.8 ± 10.3	4.7 ± 1.1	4.2 ± 2.8
7	35.2 ± 4.1	33.4 ± 13.2	19.8 ± 5.7	22.7 ± 8.9	4.2 ± 1.1	3.8 ± 2.7

7.5 3D Results

7.5.1 Simulations

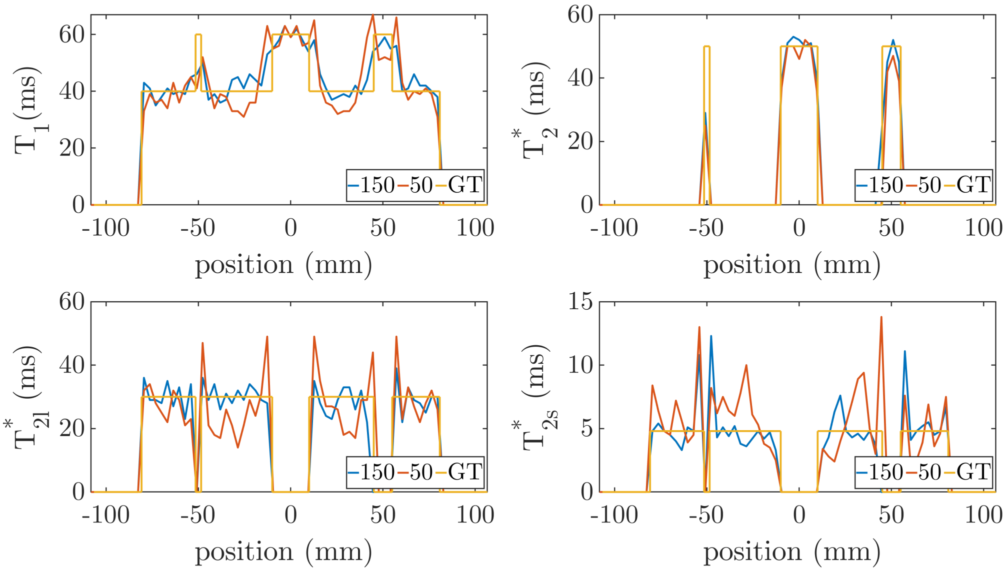

Figure 44: The real resolution of the MRF II sequence for a given nominal resolution was investigated in simulations, described in section 4.2.1.3. Here, line plots (150 spokes, 50 spokes and the ground truth) through the quantified parameters along the first line, intersecting the liquid-filled vials with diameters of 3 mm, 20 mm and 10 mm, are shown for a nominal resolution of $(3\,\mathrm{mm})^3$.

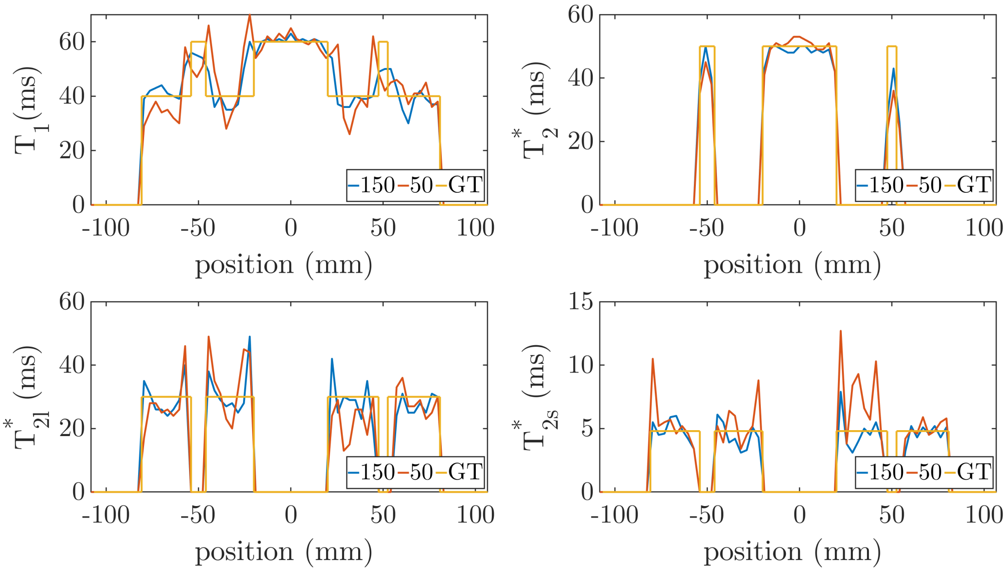

Figure 45: Line plots (150 spokes, 50 spokes and the ground truth) through the quantified parameters along the third line, intersecting the liquid-filled vials with diameters of 8 mm, 40 mm and 5 mm, are shown for a nominal resolution of $(3\,\mathrm{mm})^3$.

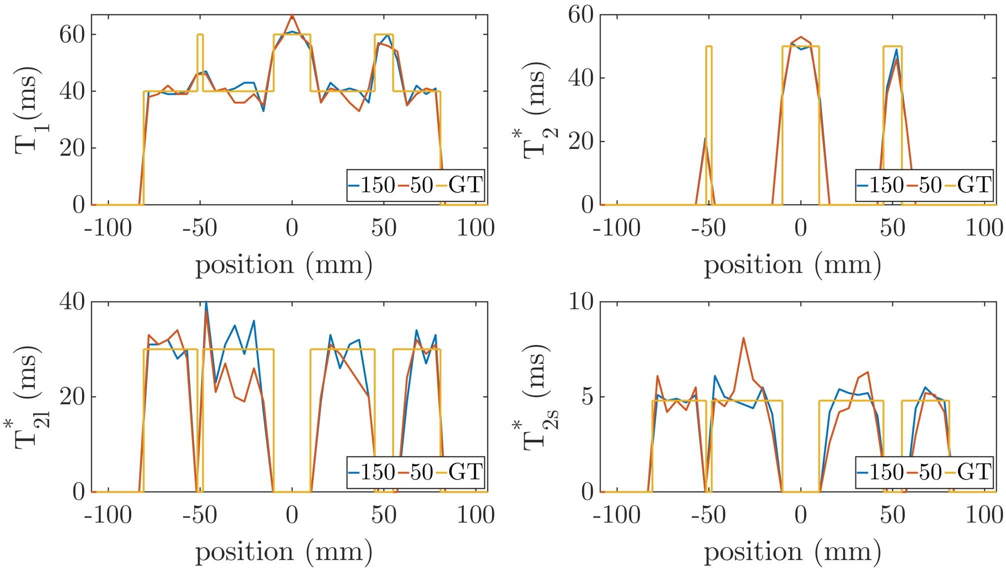

Figure 46: Line plots (150 spokes, 50 spokes and the ground truth) through the quantified parameters along the first line, intersecting the liquid-filled vials with diameters of 3 mm, 20 mm and 10 mm, are shown for a nominal resolution of $(5\,\mathrm{mm})^3$.

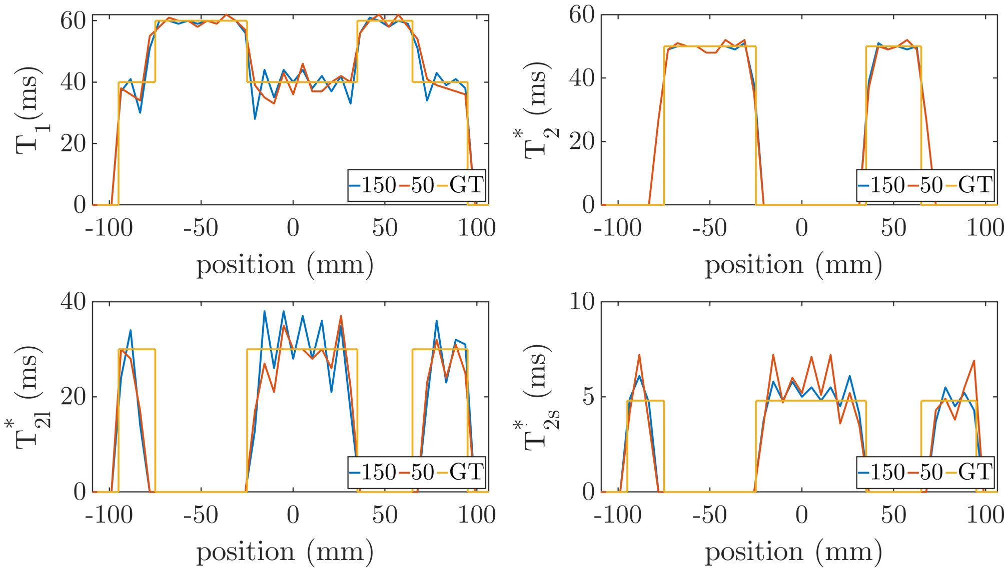

Figure 47: Line plots (150 spokes, 50 spokes and the ground truth) through the quantified parameters along the second line, intersecting the liquid-filled vials with diameters of 50 mm and 30 mm, are shown for a nominal resolution of $(5\,\text{mm})^3$.

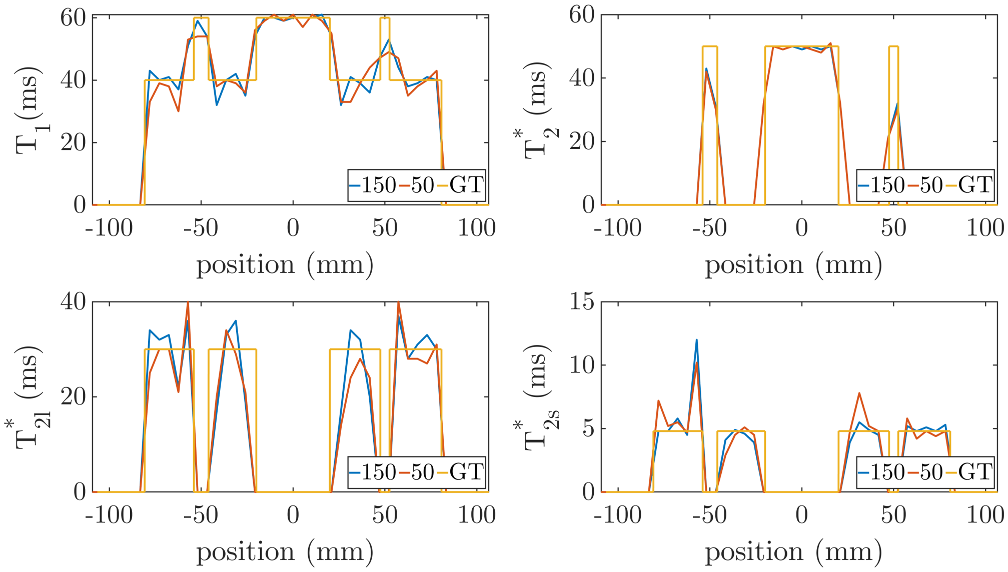

Figure 48: Line plots (150 spokes, 50 spokes and the ground truth) through the quantified parameters along the third line, intersecting the liquid-filled vials with diameters of 8 mm, 40 mm and 5 mm, are shown for a nominal resolution of $(5\,\text{mm})^3$.

7.5.2 Measurements

Table 11: Phantom measurements were conducted to investigate the encoding capabilities of the 3D MRF sequences, as explained in section 3.7.2. Mean and SD of all relaxation times in each phantom compartment were determined in the 10 central slices. The mean absolute difference between MRF I was 10.8 % with respect to the references, whereas MRF II only differed by 4.6 %. Mind that in the $T^*_{2(l)}$ column T^*_2 is shown for the compartment with 0 % Agar, whereas the compartments with Agar concentrations of 2 %–7 % show T^*_{2l}.

Agar	T_1 (ms)			$T^*_{2(l)}$			T^*_{2s}		
conc. (%)	Reference	MRF I	MRF II	Reference	MRF I	MRF II	Reference	MRF I	MRF II
0	59.1 ± 3.1	68.5 ± 12.0	58.0 ± 4.3	47.0 ± 6.1	55.6 ± 9.7	51.2 ± 5.4			
2	49.0 ± 2.0	53.4 ± 6.8	48.7 ± 3.7	36.8 ± 13.0	39.3 ± 8.0	38.5 ± 8.0	11.4 ± 3.6	12.0 ± 2.0	10.8 ± 1.5
3	45.0 ± 1.6	48.6 ± 6.9	44.9 ± 4.0	31.8 ± 7.4	34.9 ± 9.2	33.6 ± 7.3	7.9 ± 1.7	8.9 ± 2.4	7.8 ± 1.5
4	42.1 ± 1.7	48.9 ± 7.4	42.8 ± 4.0	31.6 ± 6.8	34.5 ± 8.6	32.4 ± 6.2	6.1 ± 0.9	6.7 ± 2.1	6.1 ± 1.3
5	39.2 ± 2.0	46.6 ± 6.8	40.6 ± 3.7	28.0 ± 5.6	32.7 ± 7.0	31.0 ± 5.0	5.3 ± 0.9	5.6 ± 1.7	5.0 ± 0.9
6	37.4 ± 2.0	38.9 ± 6.6	35.7 ± 3.5	26.6 ± 6.6	31.1 ± 5.9	28.9 ± 4.2	4.5 ± 0.9	4.7 ± 1.6	4.3 ± 0.8
7	36.6 ± 2.3	36.6 ± 6.9	33.4 ± 3.7	23.7 ± 5.3	28.7 ± 5.4	26.0 ± 3.6	3.8 ± 0.7	4.2 ± 1.7	3.8 ± 0.7

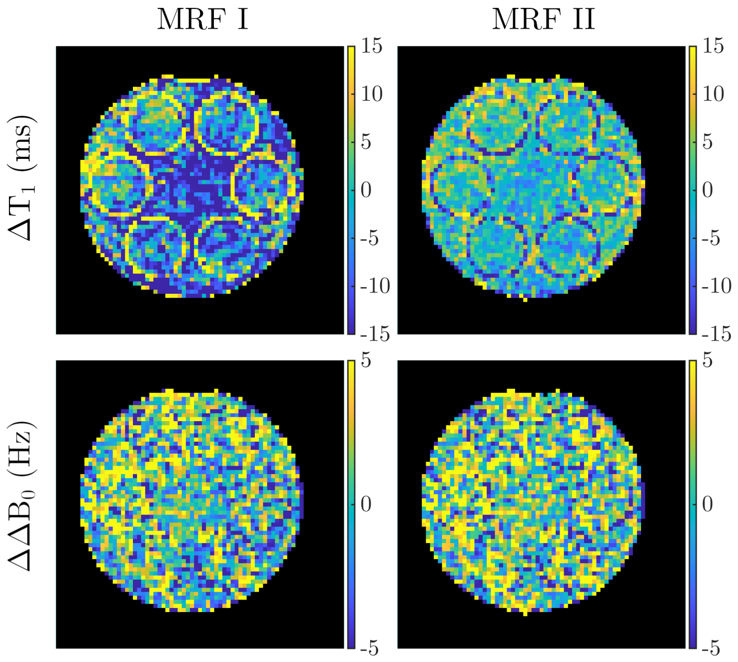

Figure 49: Difference maps of T_1 and ΔB_0 between the MRF measurements and the references are shown. Image adapted from [36].

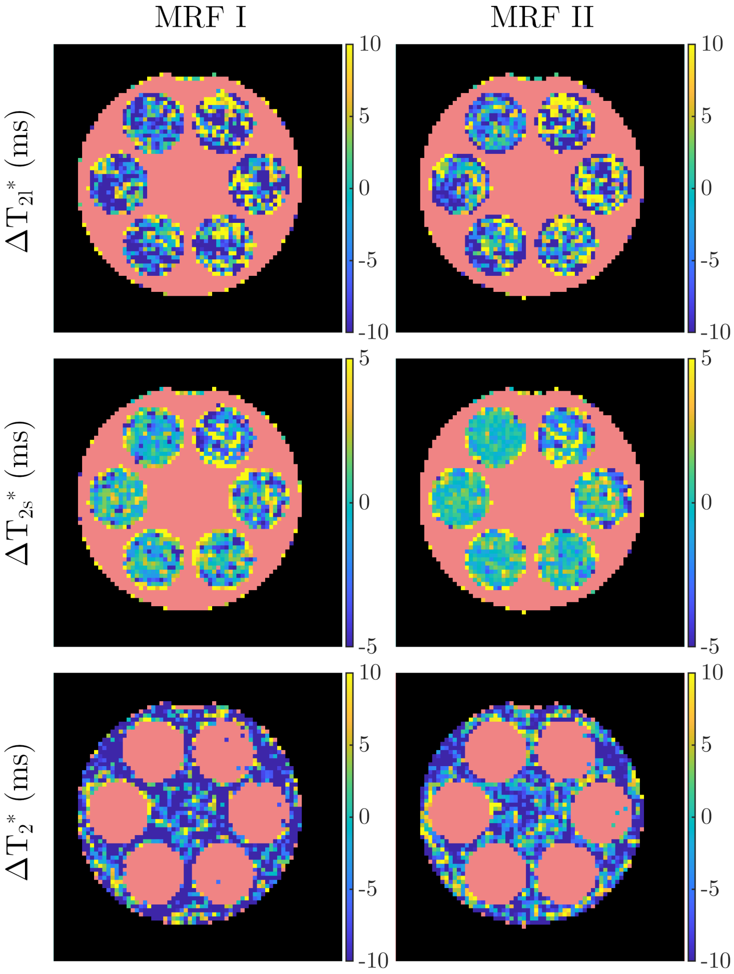

Figure 50: Difference maps of T_{2l}^*, T_{2s}^* and T_2^* between the MRF measurements and the references are shown. Image adapted from [36].

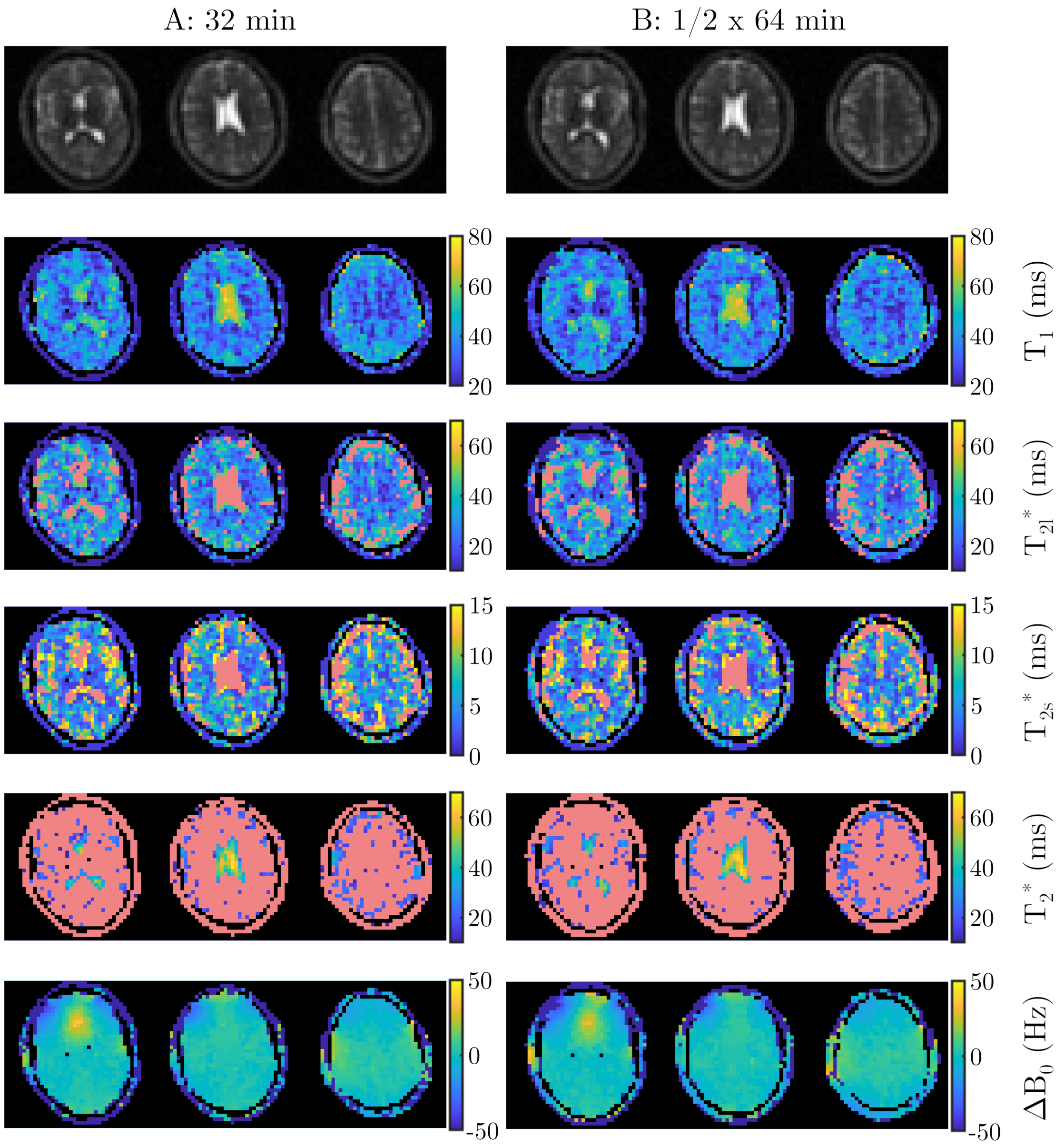

Figure 51: First coefficient images (top), relaxometric maps and off-resonance distributions for A) a measurement time of 32 min and B) every second spoke from a 64 min measurement are shown. The quantified parameters are summarized in table 8. Image adapted from [36].

7.5.3 Comparison between the ISTO and the Bloch model

Table 12: To investigate the effect of the signal model used in phantom measurements, the measured phantom data was reconstructed with both an ISTO and a Bloch dictionary. The largest bias is found in the long component of the transverse relaxation time.

Agar conc. (%)	T_1 (ms) ISTO	 Bloch	$T^*_{2(l)}$ (ms) ISTO	 Bloch	T^*_{2s} (ms) ISTO	 Bloch
0	58.0 ± 4.3	59.5 ± 4.6	51.2 ± 5.4	51.7 ± 5.7		
2	48.7 ± 3.7	50.3 ± 4.5	38.5 ± 8.0	28.9 ± 6.0	10.8 ± 1.5	12.5 ± 1.8
3	44.9 ± 4.0	45.2 ± 4.2	33.6 ± 7.3	26.7 ± 6.0	7.8 ± 1.5	8.8 ± 1.8
4	42.8 ± 4.0	42.8 ± 4.2	32.4 ± 6.2	26.6 ± 5.2	6.1 ± 1.3	6.6 ± 1.6
5	40.6 ± 3.7	39.9 ± 3.9	31.0 ± 5.0	26.6 ± 4.0	5.0 ± 0.9	5.2 ± 1.3
6	35.7 ± 3.5	34.7 ± 3.5	28.9 ± 4.2	26.2 ± 3.8	4.3 ± 0.8	4.2 ± 0.8
7	33.4 ± 3.7	32.7 ± 3.7	26.0 ± 3.6	23.7 ± 3.1	3.8 ± 0.7	3.6 ± 0.7
deviation (%):						
mean	0.0		-13.6		-3.0	
max	3.3		-25.0		15.2	

7.6 Publications

Parts of this work appear in the following publications:

Journal Publications

F.J. Kratzer, S. Flassbeck, S. Schmitter, T. Wilferth, A.W. Magill, B.R. Knowles, T. Platt, P. Bachert, M.E. Ladd, and A.M. Nagel. 3D Sodium (23Na) Magnetic Resonance Fingerprinting for time-efficient relaxometric mapping. *Magnetic Resonance in Medicine*, 2021, doi. 10.1002/mrm.28873.

F.J. Kratzer, S. Flassbeck, A.M. Nagel, N.G.R. Behl, B.R. Knowles, P. Bachert, M.E. Ladd, and S. Schmitter. Sodium relaxometry using 23Na MR fingerprinting: A proof of concept. *Magnetic Resonance in Medicine*, 84(5):2577-2591, 2020.

Conference Talks

F.J. Kratzer, S. Flassbeck, S. Schmitter, T. Wilferth, A.W. Magill, B.R. Knowles, T. Platt, P. Bachert, M.E. Ladd, and A.M. Nagel. 3D Sodium (23Na) Magnetic Resonance Fingerprinting for time-efficient relaxometric mapping. *In Proc. 23th Annual Meeting of DS-ISMRM*, 2021.

F.J. Kratzer, S. Schmitter, A.M. Nagel, N.G.R. Behl, B.R. Knowles, P. Bachert, M.E. Ladd, and S. Flassbeck. Sodium Relaxometry using Magnetic Resonance Fingerprinting. *In Proc. 29th Annual Meeting of ISMRM*, 2020. [1] [2]

F.J. Kratzer, S. Flassbeck, A.M. Nagel, T. Platt, B.R. Knowles, P. Bachert, M.E. Ladd, and S. Schmitter. 23Na-Magnetic-Resonance-Fingerprinting: Ein Vergleich zwischen gemittelten, unterabgetasteten Daten und voller Datenabtastung. *In Proc. DGMP*, 2020.

F.J. Kratzer, S. Flassbeck, A.M. Nagel, S. Schmitter, P. Bachert, M.E. Ladd, and N.G.R. Behl. 23Na Imaging using VERSE Pulses in a Density Adapted Stack-of-Stars Sequence at 7T. *In Proc. ISMRM Workshop on UHF MR*, 2019.

---

[1] This contribution was awarded the *1st Place for the best Trainee Abstract* in the X-nuclei imaging study group.

[2] This contribution was awarded the *ISMRM Summa Cum Laude Merit Award.*

Conference Posters

F.J. Kratzer, S. Flassbeck, S. Schmitter, T. Wilferth, A.W. Magill, B.R. Knowles, T. Platt, P. Bachert, M.E. Ladd, and A.M. Nagel. Three Dimensional Sodium Magnetic Resonance Fingerprinting using Irreducible Spherical Tensor Operator Simulations. *In Proc. 30th Annual Meeting of ISMRM*, 2021. [1]

F.J. Kratzer, S. Flassbeck, A.M. Nagel, P. Bachert, M.E. Ladd, and N.G.R. Behl. Density Adapted Stack of Stars Sequence for 23Na using Dictionary Learning Compressed Sensing Reconstruction. *In Proc. 28th Annual Meeting of ISMRM*, 2019.

---

[1] This contribution was awarded the *1st Place for the best Trainee Abstract* in the X-nuclei imaging study group.

References

[1] Deborah Burstein and Charles S. Springer. Sodium MRI revisited. *Magnetic Resonance in Medicine*, 82(2):521–524, 2019.

[2] Richard P. Kline, Ed X. Wu, Daniel P. Petrylak, Matthias Szabolcs, Philip O. Alderson, Myron L. Weisfeldt, Paul Cannon, and Jose Katz. Rapid in vivo monitoring of chemotherapeutic response using weighted sodium magnetic resonance imaging. *Clinical Cancer Research*, 6(6):2146–2156, 2000.

[3] Robert W. Stobbe and Christian Beaulieu. In vivo sodium magnetic resonance imaging of the human brain using soft inversion recovery fluid attenuation. *Magnetic Resonance in Medicine*, 54(5):1305–1310, 2005.

[4] Armin M. Nagel, Michael Bock, Christian Hartmann, Lars Gerigk, Jan O. Neumann, Marc A. Weber, Martin Bendszus, Alexander Radbruch, Wolfgang Wick, Heinz P. Schlemmer, Wolfhard Semmler, and Armin Biller. The potential of relaxation-weighted sodium magnetic resonance imaging as demonstrated on brain tumors. *Investigative Radiology*, 46(9):539–547, 2011.

[5] Armin M. Nagel, Erick Amarteifio, Frank Lehmann-Horn, Karin Jurkat-Rott, Wolfhard Semmler, Lothar R. Schad, and Marc A. Weber. 3 Tesla sodium inversion recovery magnetic resonance imaging allows for improved visualization of intracellular sodium content changes in muscular channelopathies. *Investigative Radiology*, 46(12):759–766, 2011.

[6] Arthur Coste, Fawzi Boumezbeur, Alexandre Vignaud, Guillaume Madelin, Kathrin Reetz, Denis Le Bihan, Cécile Rabrait-Lerman, and Sandro Romanzetti. Tissue sodium concentration and sodium T1 mapping of the human brain at 3T using a Variable Flip Angle method. *Magnetic Resonance Imaging*, 58:116–124, 2019.

[7] Yasmin Blunck, Sonal Josan, Syeda W. Taqdees, Bradford A. Moffat, Roger J. Ordidge, Jon O. Cleary, and Leigh A. Johnston. 3D-multi-echo radial imaging of 23Na (3D-MERINA) for time-efficient multi-parameter tissue compartment mapping. *Magnetic Resonance in Medicine*, 79(4):1950–1961, 2018.

[8] Jonathan M. Lommen, Sebastian Flassbeck, Nicolas G. R. Behl, Sebastian C. Niesporek, Peter Bachert, Mark E. Ladd, and Armin M. Nagel. Probing the microscopic environment of 23 Na ions in brain tissue by MRI: On the accuracy of different

sampling schemes for the determination of rapid, biexponential T2* decay at low signal-to-noise ratio. *Magnetic Resonance in Medicine*, 80(2):571–584, 2018.

[9] Ben Ridley, Armin M. Nagel, Mark Bydder, Adil Maarouf, Jan Patrick Stellmann, Soraya Gherib, Jeremy Verneuil, Patrick Viout, Maxime Guye, Jean Philippe Ranjeva, and Wafaa Zaaraoui. Distribution of brain sodium long and short relaxation times and concentrations: a multi-echo ultra-high field 23 Na MRI study. *Scientific Reports*, 8(1):1–12, 2018.

[10] Dan Ma, Vikas Gulani, Nicole Seiberlich, Kecheng Liu, Jeffrey L. Sunshine, Jeffrey L. Duerk, and Mark A. Griswold. Magnetic resonance fingerprinting. *Nature*, 495:187–192, 2013.

[11] Sebastian Flassbeck, Simon Schmidt, Peter Bachert, Mark E. Ladd, and Sebastian Schmitter. Flow mr fingerprinting. *Magnetic Resonance in Medicine*, 81(4):2536–2550, 2019.

[12] Ouri Cohen, Shuning Huang, Michael T. McMahon, Matthew S. Rosen, and Christian T. Farrar. Rapid and quantitative chemical exchange saturation transfer (CEST) imaging with magnetic resonance fingerprinting (MRF). *Magnetic Resonance in Medicine*, 80(6):2449–2463, 2018.

[13] Zidan Yu, Guillaume Madelin, Daniel K. Sodickson, and Martijn A. Cloos. Simultaneous proton magnetic resonance fingerprinting and sodium mri. *Magnetic Resonance in Medicine*, 83(6):2232–2242, 2020.

[14] Alina Gilles, Armin M. Nagel, and Guillaume Madelin. Multipulse sodium magnetic resonance imaging for multicompartment quantification: Proof-of-concept. *Scientific Reports*, 7(1):1–19, 2017.

[15] Charlie Y. Wang, Yuchi Liu, Shuying Huang, Mark A. Griswold, Nicole Seiberlich, and Xin Yu. 31p magnetic resonance fingerprinting for rapid quantification of creatine kinase reaction rate in vivo. *NMR in Biomedicine*, 30(12):e3786, 2017. e3786 NBM-17-0036.R2.

[16] A. Abragam. *The Principles of Nuclear Magnetism*. International series of monographs on physics. Clarendon Press, 1961.

[17] E.M. Haacke, R.W. Brown, M.R. Thompson, and R. Venkatesan. *Magnetic Resonance Imaging: Physical Principles and Sequence Design*. Wiley, 1999.

[18] C.P. Slichter. *Principles of Magnetic Resonance*. Springer Series in Solid-State Sciences. Springer Berlin Heidelberg, 1996.

[19] Johan R.C. Van Der Maarel. Thermal relaxation and coherence dynamics of spin 3/2. I. Static and fluctuating quadrupolar interactions in the multipole basis. *Concepts in Magnetic Resonance Part A: Bridging Education and Research*, 19(2):97–116, 2003.

[20] Ileana Hancu, Johan R.C. Van Der Maarel, and Fernando E. Boada. A Model for the Dynamics of Spins 3/2 in Biological Media: Signal Loss during Radiofrequency Excitation in Triple-Quantum-Filtered Sodium MRI. *Journal of Magnetic Resonance*, 147(2):179–191, 2000.

[21] Guillaume Madelin, Jae Seung Lee, Ravinder R. Regatte, and Alexej Jerschow. Sodium MRI: Methods and applications. *Progress in Nuclear Magnetic Resonance Spectroscopy*, 79:14–47, 2014.

[22] International Electrotechnical Comission (IEC). IEC 60601-2-33 Medical Electrical Equipment - Part 2-33: Particular Requirements for the Basic Safety and Essential Performance. 3.2, 2015.

[23] M.A. Bernstein, K.F. King, X.J. Zhou, and X.J. Zhou. *Handbook of MRI Pulse Sequences*. Academic Press, 2004.

[24] Steven Conolly, Dwight G. Nishimura, Albert Macovski, and Gary Glover. Variable-rate selective excitation. *Journal of Magnetic Resonance*, 78(3):440–458, 1988.

[25] Simon Konstandin, Armin M. Nagel, Patrick M. Heiler, and Lothar R. Schad. Two-dimensional radial acquisition technique with density adaption in sodium mri. *Magnetic Resonance in Medicine*, 65(4):1090–1096, 2011.

[26] Armin M. Nagel, Frederik B. Laun, Marc-André Weber, Christian Matthies, Wolfhard Semmler, and Lothar R. Schad. Sodium MRI using a density-adapted 3D radial acquisition technique. *Magnetic Resonance in Medicine*, 62(6):1565–1573, 2009.

[27] Yun Jiang, Jesse I Hamilton, Wei-Ching Lo, , Katherine L Wright, Dan Ma, Andrew J Corostine, Nicole Seiberlich, Vikas Gulani, and Mark A Griswold. Simultaneous T1, T2 and Diffusion Quantification using Multiple Contrast Prepared Magnetic Resonance Fingerprinting. *Proc. Intl. Soc. Mag. Reson. Med*, 25:1171, 2017.

[28] Megan E. Poorman, Michele N. Martin, Dan Ma, Debra F. McGivney, Vikas Gulani, Mark A. Griswold, and Kathryn E. Keenan. Magnetic resonance fingerprinting part 1: Potential uses, current challenges, and recommendations. *Journal of Magnetic Resonance Imaging*, 51(3):675–692, 2020.

[29] Debra F. McGivney, Rasim Boyacıoğlu, Yun Jiang, Megan E. Poorman, Nicole Seiberlich, Vikas Gulani, Kathryn E. Keenan, Mark A. Griswold, and Dan Ma. Magnetic resonance fingerprinting review part 2: Technique and directions. *Journal of Magnetic Resonance Imaging*, 51(4):993–1007, 2020.

[30] Bhairav B. Mehta, Simone Coppo, Debra Frances McGivney, Jesse Ian Hamilton, Yong Chen, Yun Jiang, Dan Ma, Nicole Seiberlich, Vikas Gulani, and Mark Alan Griswold. Magnetic resonance fingerprinting: a technical review. *Magnetic Resonance in Medicine*, 81(1):25–46, 2019.

[31] Yun Jiang, Dan Ma, Nicole Seiberlich, Vikas Gulani, and Mark A. Griswold. MR Fingerprinting Using Fast Imaging with Steady State Precession (FISP) with Spiral Readout. *Magnetic Resonance in Medicine*, 74(6):1621–1631, 2015.

[32] Jakob Assländer, Martijn A. Cloos, Florian Knoll, Daniel K. Sodickson, Jürgen Hennig, and Riccardo Lattanzi. Low rank alternating direction method of multipliers reconstruction for MR fingerprinting. *Magnetic Resonance in Medicine*, 79(1):83–96, 2018.

[33] Debra F. McGivney, Eric Pierre, Dan Ma, Yun Jiang, Haris Saybasili, Vikas Gulani, and Mark A. Griswold. SVD Compression for Magnetic Resonance Fingerprinting in the Time Domain. *IEEE Transactions on Medical Imaging*, 33(12):2311–2322, 2014.

[34] Guillaume Madelin and Ravinder R. Regatte. Biomedical applications of sodium MRI in vivo. *Journal of Magnetic Resonance Imaging*, 38(3):511–529, 2013.

[35] P Deetjen, E.-J Speckmann, and J Hescheler. *Physiologie*. Urban & Fischer Verlag/Elsevier GmbH, 2004.

[36] Fabian J. Kratzer, Sebastian Flassbeck, Sebastian Schmitter, Tobias Wilferth, Arthur W. Magill, Benjamin R. Knowles, Tanja Platt, Peter Bachert, Mark E. Ladd, and Armin M. Nagel. 3D sodium (23Na) magnetic resonance fingerprinting for time-efficient relaxometric mapping. *Magnetic Resonance in Medicine*, (doi.org/10.1002/mrm.28873), 2021.

[37] Jeffrey A. Fessler and Bradley P. Sutton. Nonuniform Fast Fourier Transforms Using Min-Max Interpolation. *IEEE Transactions on Signal Processing*, 51(2):560–574, 2003.

[38] Steven P. Allen, Glen R. Morrell, Brock Peterson, Danny Park, Garry E. Gold, Joshua D. Kaggie, and Neal K. Bangerter. Phase-sensitive sodium B1 mapping. *Magnetic Resonance in Medicine*, 65(4):1126–1131, 2011.

[39] Glen R. Morrell. A phase-sensitive method of flip angle mapping. *Magnetic Resonance in Medicine*, 60(4):889–894, 2008.

[40] Fabian J. Kratzer, Sebastian Flassbeck, Armin M. Nagel, Nicolas G.R. Behl, Benjamin R. Knowles, Peter Bachert, Mark E. Ladd, and Sebastian Schmitter. Sodium relaxometry using 23Na MR fingerprinting: A proof of concept. *Magnetic Resonance in Medicine*, 84(5):2577–2591, 2020.

[41] Jakob Assländer, Riccardo Lattanzi, Daniel K. Sodickson, and Martijn A. Cloos. Optimized quantification of spin relaxation times in the hybrid state. *Magnetic Resonance in Medicine*, 82(4):1385–1397, 2019.

[42] Jakob Assländer, Dmitry S. Novikov, Riccardo Lattanzi, Daniel K. Sodickson, and Martijn A. Cloos. Hybrid-state free precession in nuclear magnetic resonance. *Communications Physics*, 2(1), 2019.

[43] Alexander Frydahl, Karen Holst, Kenneth Caidahl, Martin Ugander, and Andreas Sigfridsson. Generalization of three-dimensional golden-angle radial acquisition to reduce eddy current artifacts in bSSFP CMR imaging. *Magnetic Resonance Materials in Physics, Biology and Medicine*, 34(1):109–118, 2021.

[44] Martin Uecker, Peng Lai, Mark J. Murphy, Patrick Virtue, Michael Elad, John M. Pauly, Shreyas S. Vasanawala, and Michael Lustig. Espirit—an eigenvalue approach to autocalibrating parallel mri: Where sense meets grappa. *Magnetic Resonance in Medicine*, 71(3):990–1001, 2014.

[45] Chris A. Cocosco, Vasken Kollokian, Remi K.-S. Kwan, and Alan C. Evans. BrainWeb: Online Interface to a 3D MRI Simulated Brain Database. *NeuroImage*, 5(4):425, 1997.

[46] Cheng G. Koay, Joelle E. Sarlls, and Evren Özarslan. Three-dimensional analytical magnetic resonance imaging phantom in the Fourier domain. *Magnetic Resonance in Medicine*, 58(2):430–436, 2007.

[47] Sebastian Schmitter, Michael Bock, Sören Johst, Edward J. Auerbach, Kâmil Uğurbil, and Pierre-François Van de Moortele. Contrast enhancement in TOF cerebral angiography at 7 T using saturation and MT pulses under SAR constraints: Impact of verse and sparse pulses. *Magnetic Resonance in Medicine*, 68(1):188–197, 2012.

[48] Nan Kuei Chen and Alice M. Wyrwicz. Optimized distortion correction technique for echo planar imaging. *Magnetic Resonance in Medicine*, 45(3):525–528, 2001.

[49] Nicolas G. R. Behl, Christine Gnahm, Peter Bachert, Mark E. Ladd, and Armin M. Nagel. Three-dimensional dictionary-learning reconstruction of 23Na MRI data. *Magnetic Resonance in Medicine*, 75(4):1605–1616, 2016.

[50] Lazar Fleysher, Niels Oesingmann, Bernd Stoeckel, and Robert I. Grossman. Sodium Long-Component T2* Mapping in Human Brain at 7 Tesla. *Brain*, 62(5):1338–1341, 2009.

[51] Robert V. Mulkern, Mukund Balasubramanian, and Dimitrios Mitsouras. On the Lorentzian versus Gaussian Character of Time-Domain Spin-Echo Signals from the Brain as Sampled via Gradient-Echoes: Implications for Quantitative Transverse Relaxation Studies. *Magnetic Resonance in Medicine*, 74(1):51–62, 2015.

[52] Robert W. Stobbe and Christian Beaulieu. Residual quadrupole interaction in brain and its effect on quantitative sodium imaging. *NMR in Biomedicine*, 29(2):119–128, 2016.

[53] Sunlin Tang, Carlos Fernandez-Granda, Sylvain Lannuzel, Brett Bernstein, Riccardo Lattanzi, Martijn A. Cloos, Florian Knoll, and Jakob Assländer. Multicompartment Magnetic Resonance Fingerprinting. *Inverse Problems*, 34(9), 2018.

[54] Sebastian C. Niesporek, Reiner Umathum, Thomas M. Fiedler, Peter Bachert, Mark E. Ladd, and Armin M. Nagel. Improved T2* determination in 23Na, 35Cl, and 17O MRI using iterative partial volume correction based on 1H MRI segmentation. *Magnetic Resonance Materials in Physics, Biology and Medicine*, 30(6):519–536, 2017.

[55] Jonathan M. Lommen, Frank Resmer, Nicolas G. R. Behl, Michael Sauer, Nadia Benkhedah, Andreas K. Bitz, Reiner Umathum, Mark E. Ladd, Titus Lanz, and Armin M. Nagel. Comparison of a 30-channel head array with a birdcage for 23Na MRI at 7 Tesla. *Proc. Intl. Soc. Mag. Reson. Med.*, 24:3974, 2016.

[56] Simon Konstandin and Lothar R. Schad. 2D Radial Sodium MRI using VERSE. *Proc. Intl. Soc. Mag. Reson. Med*, 20:1697, 2012.

Acknowledgments

An dieser Stelle möchte ich mich bei allen Personen bedanken, die mich während der Promotion begleitet und unterstützt haben.

Zuerst möchte ich mich bei Herrn Prof. Dr. Bachert für die Vertretung dieser Arbeit gegenüber der Fakultät bedanken. Der unkomplizierte und gute Umgang mit Ihnen hat mir in den letzten Jahren vieles erleichtert.

Herrn Prof. Dr. Schad möchte ich für die Übernahme des Zweitgutachtens danken.

Vielen Dank auch an Herrn Prof. Dr. Ladd, dass ich die letzten Jahre in seiner Abteilung arbeiten und vieles lernen konnte.

Ein besonderer Dank geht an Armin und Sebastian S., die mich so kurzfristig unter ihre Fittiche genommen haben. Trotz der Entfernung habt ihr es geschafft immer ein offenes Ohr zu haben. Eure Ideen, Hilfe und Ratschläge waren unglaublich wertvoll und vieles hätte ohne euch so nicht geklappt.

Ein zweites riesiges Dankeschön geht an Sebastian F. Die Zusammenarbeit mit dir, deine Unterstützung und die gemeinsamen Diskussionen haben diese Arbeit geprägt. Besonders zu Beginn der Promotion habe ich unglaublich von deinem Wissen und deinen Ideen profitiert. Nochmal danke fürs Korrekurlesen dieser Arbeit und all die spaßigen privaten Aktionen!

Auch Tobias, Tanja, Stephan, Ben und Arthur möchte ich für die anregenden Diskussionen danken.

Euch, Simon, Melanie, Johanna, Lucy, Anna, Jan, Kilian und Marco möchte ich nochmal gesondert danken. Die vielen Stunden des gemeinsamen Blödsinns, die Fußballtennis-Duelle und vieles mehr haben wahnsinnigen Spaß gemacht.

Der gesamten 7T-Gruppe und all den anderen Leuten, denen ich hier nicht gerecht werde, möchte ich von Herzen für die großartige Zeit danken. Die gute Atmosphäre, die Feiern und die Kaffeepausen haben die letzten Jahre zu einer unvergesslichen Zeit gemacht.

Zuletzt möchte ich meinen Freunden und meiner Familie danken. Eure Unterstützung, Geduld und Nerven haben diese Arbeit letztendlich erst möglich gemacht.